THESIS FOR THE DEGREE OF LICENTIATE OF ENGINEERING

High-Temperature Corrosion in Waste-Fired Boilers:

Insights into material selection for fluidized bed heat exchangers and the corrosivity of $PbCl_2$

HAMPUS LINDMARK

Department of Chemistry and Chemical Engineering
Division of Energy and Materials
CHALMERS UNIVERSITY OF TECHNOLOGY
Gothenburg, Sweden 2023

High-Temperature Corrosion in Waste-Fired Boilers: Insights into material selection for fluidized bed heat exchangers and the corrosivity of $PbCl_2$
HAMPUS LINDMARK

Thesis for the degree of Licentiate of Engineering 2023:11
Department of Chemistry and Chemical Engineering
Division of Energy and Materials
Chalmers University of Technology
SE-412 96 Gothenburg
Sweden
Telephone + 46 (0)31-772 1000

Cover: *Left;* Schematic image of the furnace set-up used in this project. SEM-BSE cross-section images of a low-alloyed steel exposed to the furnace set-up for 168 hours, both with and without $PbCl_2$. *Right;* Schematic image of the CFB waste-fired boiler used for field exposures in this project. SEM-BSE cross-section images of a FeCrAl alloy exposed to the boiler for 6 and 12 months.

Chalmers Reproservice
Gothenburg, Sweden 2023

ABSTRACT

The replacement of fossil fuels with waste-derived fuels for heat and electricity production has gained significant momentum in the European Union (EU), especially in the wake of the implementation of stricter waste management directives and the pursuit of ambitious climate goals. Combustion of waste, however, leads to the formation of a complex and highly corrosive flue gas that cause severe corrosion on important boiler equipment. Consequently, corrosion has significant impact on the operational cost and electrical efficiency of the power plant. As an approach to improve boiler efficiency, modern designed circulating fluidized bed (CFB) waste-fired boilers conduct the final heating of the superheated steam within the loop seal region. However, there is limited published research on the performance of different alloy types in this region of the boiler, and the influence of corrosive and erosive events on the material degradation mechanisms remains relatively elusive. Furthermore, in the water wall region of waste-fired boilers, elevated concentrations of Pb-containing compounds such as $PbCl_2$ have been identified and linked to the accelerated corrosion rate of the tube material. Nevertheless, there is a limited comprehension of the underlying corrosion mechanism in $PbCl_2$-induced corrosion of low-alloyed steel, which is often used as tube material in this area of the boiler.

The aim of this thesis is to address these aforementioned concerns through a combination of field exposures and laboratory studies. A field exposure study was conducted on a commercial CFB boiler to assess the performance of relevant alloy types for superheater application in the loop seal region of the boiler and to improve the understanding of the synergetic effect of corrosion and erosion attacks on the material degradation mechanism. The results from the study revealed that novel FeCrAl alloys exhibited comparable material loss to a conventional nickel-based alloy, positioning them as viable candidates for this application with the potential to reduce material costs. However, significant internal Al-nitridation was observed for this material, and further studies are required in order to understand its impact on the materials' corrosive protective properties. Lastly, the results observed in this study underscore that corrosion rather than erosion is the principal driving force for the observed material losses, highlighting the importance of considering corrosion mitigation strategies when choosing suitable materials for this application.

Additionally, a time-resolved laboratory study was carried out to investigate the corrosive nature of $PbCl_2$(s) on low-alloyed steel at 400°C in a humid environment. Based on the findings presented in this work, it was shown that the presence of $PbCl_2$(s) significantly accelerated the corrosion rate of the steel substrate. The corrosion attack is argued to be driven by the extreme reactivity of $PbCl_2$(s) in the studied environment which leads to a local release of HCl(g) and the introduction of metal chlorides to the metal/oxide interface that promotes severe delamination, void formation, and development of cracks within the oxide scale. The results suggests that Cl plays a pivotal role in both the initiating and propagating corrosion mechanisms of $PbCl_2$-induced corrosion on low-alloyed steels, whereas the Pb compound in $PbCl_2$ do not demonstrate any corrosion-accelerating properties.

Keywords: *High-Temperature Corrosion, Superheaters, $PbCl_2$, Water Walls*

LIST OF PUBLICATIONS

This thesis is based on the work contained in the following appended papers:

Paper I

H. Lindmark, J. Phother, M. Dolores Paz, J. Nockert, F. Lind, A. Jonasson, V. Barišić, K. Vänskä, L. Rioja-Monllor and J. Liske., *"A material degradation study of novel FeCrAl alloys, stainless steels and nickel base alloy in fluidized bed heat exchangers of a waste-fired CFB boiler"*. Fuel, vol. 338, p.127299, Apr. 2022. Doi: 10.1016/j.fuel.2022.127299

Paper II

H. Lindmark, T. Jonsson and J. Liske., *"A time-resolved study of $PbCl_2$-induced corrosion in the presence of water vapour at 400°C on low-alloyed steel."*. Manuscript

Statement of the author's contribution

Paper I: I was the main author of the paper and performed all the analytical work. I wrote the first draft and was responsible for the manuscript.

Paper II: I was the main author of the paper and performed all the experimental and analytical work. I wrote the first draft and was responsible for the manuscript.

Related technical report not included in this thesis:

H. Lindmark, F. Lind, M. Dolores Paz, L. Rioja-Monllor, B. Wahlund, A. Jonasson, J. Nockert, M. Hautakangas, H. Larsson, V. Barišić, K. Vänskä and J. Liske., *"New materials and oxygen carrier aided combustion for improved competitiveness of FB plants using renewable fuels"*. Konsortium Materialteknik för Termiska Energiprocesser (KME) report 2022. ISBN: 978-91-7673.

LIST OF ACRONYMS

AlN: Aluminum Nitride

BCC: Body-Centered Cubic

BECCS: Bioenergy with Carbon Capture and Storage

BIB: Broad Ion Beam

BSE: Backscattered Electrons

CCS: Carbon Capture and Storage

CFB: Circulating Fluidized Bed

CHP: Combined Heat and Power

EC: European Commission

EDX: Energy-Dispersive X-ray Spectroscopy

EGD: European Green Deal

EU: European Union

FBHE: Fluidized Bed Heat Exchanger

FCC: Face-Centered Cubic

GHG: Greenhouse Gases

HTC: High Temperature Corrosion

MSW: Municipal Solid Waste

OpEx: Operating Expenditure

RE: Reactive Element

RWW: Recycled Wood Waste

SE: Secondary Electrons

SEM: Scanning Electron Microscope

STEM: Scanning Transmission Electron Microscopy

WtE: Waste-to-Energy

XRD: X-ray Diffraction

LIST OF FIGURES

ACKNOWLEDGEMENTS

I have had the enormous privilege of being surrounded by inspiring and supportive people who have guided me throughout my work leading to this thesis. I would like to take the opportunity to express my gratitude towards everyone who has been part of this journey.

First and foremost, I would like to express my sincere gratitude towards my supervisors Jesper Liske, Ph.D., and Torbjörn Jonsson, Ph.D. Thank you for allowing me to carry out my work that led to this thesis in the high-temperature corrosion group at Chalmers University of Technology. You are brilliant researchers, and your passion for your work and engagement with your students has been truly inspiring. Your input in my work and your expertise in the field has been invaluable. The unwavering support and encouragement I have received from you throughout this roller coaster of a journey have been beyond anything I could ever ask for. Thank you for your guidance.

Few Ph.D., students have the privilege of having not only their supervisors but also their examinator engaged in your research. I would like to thank my examiner Professor Jan-Erik Svensson, whose support and valuable feedback have greatly benefited my research and education. Thank you for always leaving your door open for any discussions.

I would like to acknowledge Maria Dolores Paz, Ph.D., and Christine Geers, Ph.D., for their support, especially during my first year at Chalmers. Starting my work amid a pandemic while building a new experimental set-up was challenging and lonely. However, your feedback and endless moral support helped me through this time. Thank you.

I am so grateful for all the fruitful discussions and collaborations I have had with my co-authors and industry partners. Thank you for sharing your knowledge with me!

Furthermore, I would like to thank Professor Lars-Gunnar Johansson. Your immense knowledge in high-temperature corrosion and inorganic chemistry is genuinely inspiring. Thank you for your valuable discussion and feedback on my work.

I would like to extend my gratitude towards my former and current office mates, Esraa Hamdy, Ph.D., and Aida Nikbakht, Ph.D-ish😉. Thank you both for all the laughs and indefinite support.

A big reason why I have enjoyed working at Chalmers is because of my former and current colleagues at the division of energy and materials. Thank you all for providing such a fantastic work environment! Thank you, Jan Froitzheim, Ph.D., for being such a great manager (I know you hate when I call you that, my apologies), particularly during these last months, which have been tough on a personal level.

Lastly, I would like to dedicate the final part to my family. A heartfelt expression of gratitude goes to my mother, father, sisters, and brother for your unwavering support, warmth, and patience. Special recognition goes to my partner Ludovica Frare. Thank you for your comfort, support, and encouragement. Words can't describe how lucky I am to have you in my life.

Dearest Dad. Your pride in my acceptance as a Ph.D. candidate at Chalmers will forever remain engraved in my heart. Although you are no longer with us, your invaluable lessons of kindness, courage, wisdom, and humility have shaped the person I am today and will guide me as I move forward to the next phase of my Ph.D., journey. Thank you for everything.

Hampus Lindmark, Gothenburg (2023)

Table of Contents

CHAPTER I
Motivation

1.1 The Connections between Climate Change, Waste and Corrosion

In March 2023, the Intergovernmental Panel on Climate Change (IPCC) finalized its sixth assessment report in which it summarized the current state of knowledge regarding the effects of anthropogenic emissions on climate change [1]. The conclusion from the report is clear: the rapid rise in global temperature since the industrial revolution is primarily attributed to the increased release of greenhouse gases (GHG) as a result of human activities [1-3]. The anthropogenic release of CO_2 is often cited as one of the main contributors to the greenhouse effect. Over the past few decades, emissions of CO_2 to the atmosphere have increased significantly, with a noticeable correlation between the levels of emissions and the global temperature increase (Figure 1.1) [4, 5]. Today, there is a consensus in the scientific community that a temperature increase of this magnitude will impose significant stresses on the earth's climate and ecosystems, resulting in a higher frequency of extreme weather events, such as droughts and heatwaves, which may result in some populated regions becoming uninhabitable in the near future [1, 2, 6].

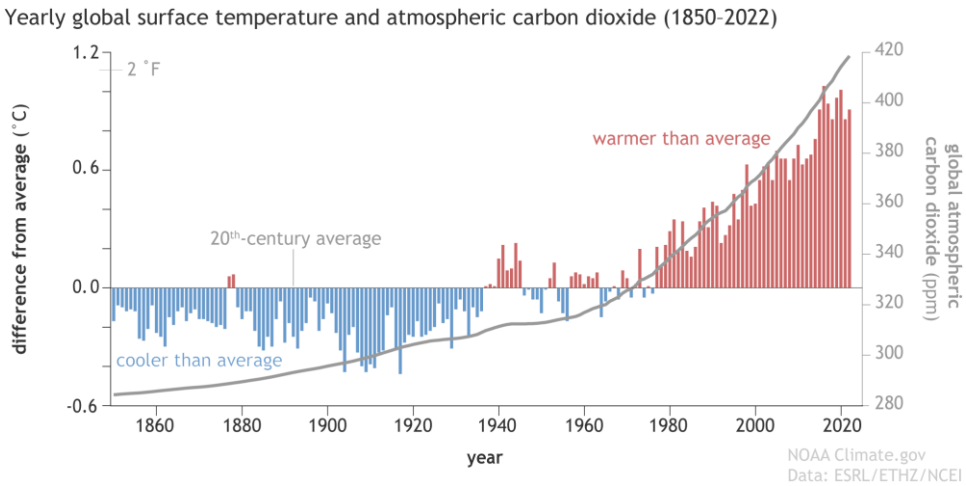

Figure 1.1: CO_2 levels in the atmosphere and surface temperatures globally over the last 160 years [7].

According to a previous report [8], more than 40% of the global emissions of CO_2 originate from heat and electricity production. The primary driver behind this substantial emission percentage is the sector's strong reliance on fossil fuels. Approximately two-thirds of the world's electricity is generated using fossil fuels, with coal serving as the predominant fuel source [8]. To address the ongoing global climate crisis, policymakers, in line with technological improvements, have proposed climate-resilient solutions for more sustainable energy production. For instance, as part of the European Green Deal (EGD), the European Union (EU) Member States have agreed upon an ambitious climate plan, with the aim of becoming the first climate-neutral continent by Year 2050 [9]. Today, it is accepted that electrification of industry and infrastructures will play an important role in reaching this goal [10-12]. Thus, the demand for electricity that is generated using sustainable technologies is expected to increase significantly in the near future.

In recent decades, biomass and waste-derived fuels have replaced the fossil fuels used in Combined Heat and Power (CHP) plants in Scandinavian countries to generate sustainable district heating and electricity. As an example, Figure 1.2 describes the fuel blends employed at the Händelö CHP plant in Sweden over the past 30 years. Notably, biomass and waste had almost completely replaced the use of fossil fuels by Year 2021. Waste derived from renewable sources, the origins if which can vary from straw to reused wood residue, are suggested to contribute close to net-zero CO_2 emissions, thereby promoting a low-carbon approach to heat and electricity production [13].

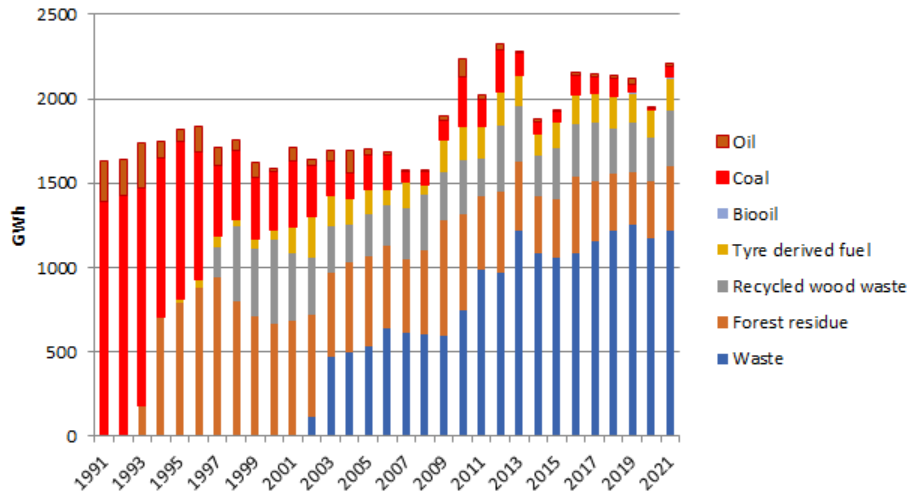

Figure 1.2: Description of the fuel mixes used in the last 30 years at Händelöverket, Sweden (courtesy of E.ON Energy Infrastructure AB).

One technical challenge that arises with the introduction of waste-derived fuel in CHP plants is the high corrosion rate of critical components of the boiler, such as the water wall and superheater tubes, which has been correlated with the complex corrosive flue gas that originates from the combustion of waste [14-16]. This results in significant operational expenditures (OpEx), including costs for materials and unplanned maintenance work. In fact, according to previous studies, roughly 70% of all the shutdowns of waste-fired boilers are associated with high-temperature corrosion [17, 18]. As such, waste-fired boilers are operated at lower temperatures compared to fossil fuel-based boilers, which results in inferior steam properties and lower electrical efficiency [18]. Depending on the position of the heat exchangers in the waste-fired boiler, the corrosion mechanism and rate can differ significantly.

Analyses of the flue gas and deposits extracted from the water wall region of waste-fired boilers have revealed the presence of high amounts of H_2O, hydrochloric acid (HCl), alkali chlorides and heavy metal chlorides, such as $PbCl_2$ [19-21]. Studies have demonstrated that these components can significantly accelerate the corrosion rate of critical boiler equipment, including water walls [22-28] and superheater tubes [29-31]. Low-alloyed steels are often implemented in this part of the boiler due to their low cost, good mechanical strength, and low heat expansion coefficient [32]. However, studies have shown that this material suffers from severe corrosion in this environment [32, 33]. Reducing the corrosion rate of the water-wall tubes can be accomplished by overlay welding the low-alloyed steel surface with coatings that contain a high-alloyed steel, such as a Ni-base alloy or austenitic stainless. However, this may increase the material cost by tenfold.

Extensive research has been carried out over the years regarding water-wall corrosion and the effect of $PbCl_2$, including field studies and complex experimental matrices that involve the interaction of $PbCl_2$ with various deposited compounds [22, 28, 34-37]. Previous work has suggested that $PbCl_2$ accelerates the rate of corrosion of water-wall tubes, both on its own and when mixed with other salts through the formation of melts, regardless of steel type [20, 33, 34]. Although the degree of severity of the corrosion attacks is apparent, the reaction mechanisms are not yet fully understood. To grasp fully the role of $PbCl_2$ in this environment, it is of great importance to develop well-controlled laboratory studies to investigate the initiation and propagation mechanisms of $PbCl_2$-induced corrosion.

As an approach to improve the steam parameters, modern circulating fluidized bed (CFB) waste-fired boilers contain superheaters [referred to as *fluidized bed heat exchangers* (FBHEs)] within the recirculation loop, called the loop seal, where the fluidizing medium is recirculated back to the combustion chamber. This region has good heat transfer properties of the recirculated fluidizing medium, which can indirectly lead to an increase in electrical efficiency, as compared with superheaters mounted in the convective pass [38]. In addition, the flue gas components are largely separated from this region, which should, in theory, lead to a significantly reduced corrosive environment. However, previous studies have shown that the FBHE suffer from material degradation due to the corrosive and erosive environment [38-40]. Though studies of superheater material performance within the loop seal region are scarce, it is of great importance to acquire knowledge of the degradation mechanism, so as to implement the most-suitable material in terms of corrosion/erosion resistance and cost effectiveness.

1.2 Aim

This thesis aims to contribute to an improved understanding of the high-temperature corrosion mechanisms that occur in waste-fired boilers. The specific objectives are:

(1) Improve current understanding of the complex material degradation mechanisms of the FBHEs positioned in the loop seal regions of waste-fired boilers; and

(2) Increase understanding of the corrosion mechanisms regarding $PbCl_2$-induced corrosion of low-alloyed steels in an environment that relates to the water-wall region of a waste-fired boiler.

In **Paper I**, we investigate the degradation rates and mechanisms of different alloy types that are exposed in the loop seal region of an 80-MW_{th} CFB waste-fired boiler. The alloys were exposed for 6 and 12 months by clamping half-moon rings of the samples onto the tubes of the installed FBHE bundle. The following research questions were addressed: What type of alloy material is suitable for this application? Does corrosion or erosion exert the strongest influence on the degradation rate of the material, or is there a synergism between erosion and corrosion? For this study, cross-sections were prepared by means of mechanical polishing, and the microstructural analyses were performed using scanning electron microscopy (SEM) coupled with energy-dispersive x-ray (EDX) spectroscopy.

In **Paper II**, we address the knowledge gap related to the initiation and propagation mechanism of $PbCl_2$-induced corrosion of a low-alloyed steel (T22) at 400°C in a humid atmosphere. This was done by implementing a time-resolved experimental approach, where we exposed T22 to $PbCl_2$ for 1, 24 and 168 h in an isothermally controlled laboratory-scale environment. The following research

questions were addressed: How rapid is the $PbCl_2$-induced corrosion attack on the T22 alloy? How do the individual elements of Pb and Cl affect the corrosion rate? How do the initiation and propagation mechanisms differ from each other? Microstructural analyses were carried out on carefully prepared ion beam-milled cross-sections. The analysis was performed by means of SEM coupled EDX and x-ray diffraction (XRD).

CHAPTER II
From Waste to Heat and Electricity

With an increasing global population, the consumption of goods and products is expected to increase, which in turn will increase the amounts of waste generated by households and industry. In Year 2018, the World Bank released an extensive report titled: *What a waste 2.0: A global snapshot of Solid Waste Management to 2050,* which discussed current and future global waste production patterns. Based on data collected from 217 countries regarding municipal solid waste (MSW) generation, the authors of that report have projected that MSW will increase by 70% during the period of 2020–2050 [41]. Globally, MSW and industrial waste are often discarded in open landfills, as this represents a cost-effective method for waste management. However, from the sustainability point-of-view, landfills are a rather inconvenient way of disposing waste, as they fail to recover potential materials and energy. In addition, high levels of GHG and toxic gases, such as methane and dioxins, are being emitted to the atmosphere, which are harmful to both the environment and human health [42].

2.1 The EU's Waste-to-Energy Approach and Prospects

As an approach to adopting a more-sustainable approach to waste management, the European Commission (EC) has implemented at the beginning of 21st Century two important pieces of legislation that strive to mitigate the use of landfills [Waste Framework Directive (2008/98/EC) and Landfill Directive (Council Directive 1999/31/EC)] [43, 44]. Through the Waste Framework Directive, a so-called "waste hierarchy" was initiated, which established the priority of waste treatments (Figure 2.1). Thus, when prevention, re-usage and recycling measures are not viable options, incineration should be implemented as a way to improve energy recovery [45]. As a consequence, the percentage of MSW generated in the EU that ends up in landfills has been reduced from 52.6 wt.% in 1999 to 22.8 wt.% per capita in 2021, whereas incineration for energy recovery, i.e., utilizing MSW as a fuel in waste-to-energy (WtE) plants, is steadily increasing (see Figure 2.1) [46]. In fact, in some EU Member States, such as Sweden, the landfilling of combustible and organic waste streams has been banned since Year 2005, which has led to a large portion of the produced waste being used as fuel in CHP plants for energy recovery, providing over 780,000 households with electricity, which accounts for roughly 16% of all households in Sweden [47, 48].

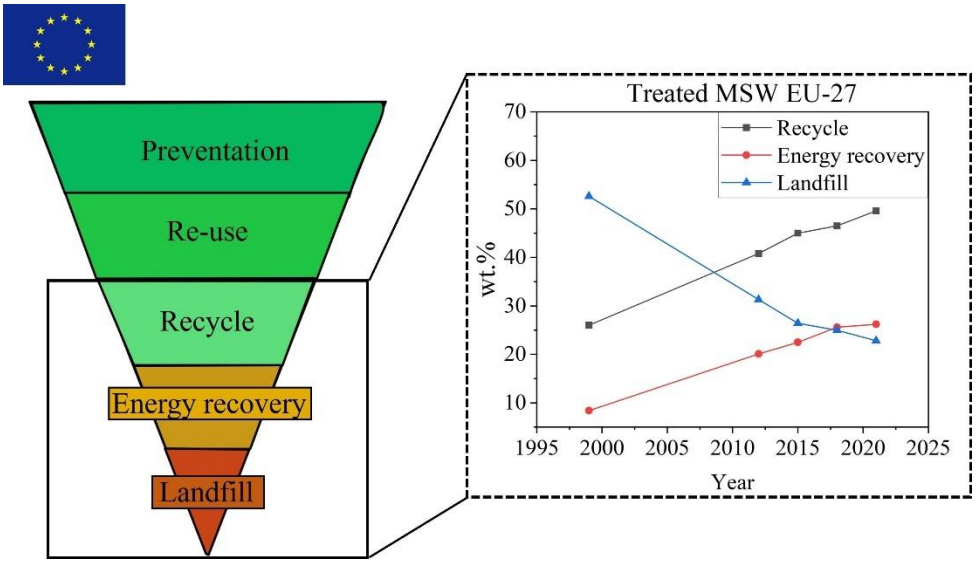

Figure 2.1: The EU waste hierarchy, along with data on treated MSW of the EU-27 Member States. Calculated from [46], expressed as wt.% of total MSW generated per capita in the EU-27.

In terms of future prospects, negative CO_2 emissions from waste-fired boilers could be achieved if they are integrated with the carbon capture and storage (CCS) technology. CCS involves a process whereby CO_2 is separated from the flue gas and transported to a storage site where it is injected into stable geological features, effectively sequestering it for hundreds of thousands of years. If the majority of the waste-fuel is derived from biogenic sources, the realization of negative CO_2 emissions could be within reach through use of the so-called Bioenergy with Carbon Capture and Storage (BECCS) technology (Figure 2.2). This is because biomass consumes CO_2 from the atmosphere during photosynthesis. By capturing the CO_2 emissions before exiting to the atmosphere, a negative CO_2 would be realized. Currently, BECCS is recognized as one of the more-promising large-scale carbon-negative technologies in terms of meeting the global, long-term CO_2 emissions targets. As an example of the potential of BECCS, a Swedish governmental study in Year 2020 suggested that the adoption of BEECS in biomass- and waste-fired boilers in Sweden could result in the uptake of 10 $MtCO_2$/year by Year 2045. This figure would correspond to around 25% of the current total CO_2 emissions in Sweden [49]. However, as mentioned in several previous studies, there remain serious technical and economic challenges that need to be solved before large-scale, WtE-based BEECS systems can be realized [50, 51].

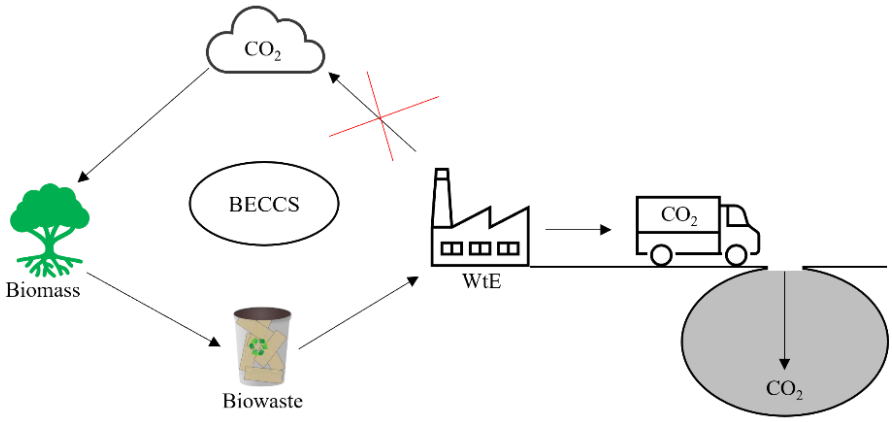

Figure 2.2: Illustration of the BECCS technology.

2.2 Waste-to-Energy (WtE)

The process of converting waste fuel to electricity and heat involves direct combustion in waste-fired boilers. Waste-fired boilers utilize the steam Rankine cycle to produce superheated steam that drives a turbine for electricity production. During the combustion of waste, a hot flue gas is formed in the combustion chamber, which is typically enclosed by the water-walls tube membrane. Commonly, the surface temperatures of the water-wall material facing the fireside of the boiler are within the range of 300°–400°C [52, 53] depending on the fuel and combustion technique used. Pressurized water is present inside these tubes, and the hot flue gas formed during combustion is utilized to heat the water to saturated steam. The steam is transported to the top end of the water-wall region, where saturated steam is separated from the water in a so-called *steam drum*. Thereafter, the saturated steam is transported to the superheaters, where the steam is further heated until superheated steam is formed. The superheated steam is then utilized to power a steam turbine, which converts mechanical energy into electrical power. While generating electricity, the power plant can simultaneously meet the heating demand of regional residential buildings by utilizing the excess heat exiting the turbine for district heating, thereby optimizing the use of the energy source [54, 55]. This combination is known as CHP production. This approach can achieve up to 85% energy efficiency with respect to the energy content of the waste fuel [53]. Today, CHP is frequently integrated into WtE power plants in the EU [56].

A major technical challenge that arises with waste-fired boilers is the formation of a highly corrosive flue gas that originates from the combustion of waste. Several authors have reported high concentrations of HCl, alkali chlorides and heavy metal chlorides, such as KCl and $PbCl_2$, in the flue gases of waste-fired boilers. These compounds may condense upon interaction with heat-exchange surfaces and form highly corrosive deposits that seriously reduce the lifetime of the material [20, 52, 57-63]. Depending on the prevailing environment (e.g., temperature and fuel composition), the corrosion rate and mechanism can vary for different parts of the boiler. Consequently, to decrease the corrosion rate, the steam temperature of waste-fired boilers is operated at a relatively low temperature. This has a detrimental effect on the electrical efficiency of the power plant, as the temperature and pressure of the steam entering the turbine dictate the turbine efficiency. When it comes to waste-fired boilers, the superheated steam temperature is generally constrained to the range of 350°–475°C. In contrast, state-of-the-art coal-fired boilers have been reported to reach steam temperatures >600°C. Consequently, the electrical efficiencies of waste-fired boilers have been reported as 18%–26%, whereas the average efficiency of fossil fuel boilers is in the range of 35%–45% [18, 55, 64].

Today, grate-fired, fluidized bed, and CFB boilers are the three primary combustion reactors employed in biomass and waste combustion for heat and power generation [65]. **Paper I** of this thesis focuses on field exposures conducted in a CFB boiler and, therefore, a concise overview of this technique will be provided in the section below.

2.3 Circulating Fluidized Bed Boiler

A schematic of a CFB boiler is shown in Figure 2.3. In a CFB boiler, the combustion process occurs in contact with a circulating bed material, which commonly comprises sand and the ash formed during combustion. The fuel is introduced into the combustion chamber, where primary air is injected from the bottom of the chamber to guarantee steady combustion and to ensure that the bed

material remains in a fluidized state. The heat transfer and efficient combustion rate are enabled by the homogeneous mixing of the fuel, air, and bed material. The hot flue gas is used for heating the boiler water present in the water-wall tubes, which is eventually transported to the superheaters, while the flue gas exits the furnace and is transported to the cyclone, where the bed material and large fuel particles are separated from the flue gas. The bed material is recirculated to the furnace chamber via a loop seal, which has its own inlet of air for rapid transportation [66].

The CFB technology is recognized for its high environmental performance and fuel flexibility for large-scale combustion of a variety of different solid-derived fuels, such as MSW, sludge, industrial waste, and recycled wood. In addition, the technique is suitable for the combustion of fuels that have a high moisture content, which reduces the cost of pretreating the fuel. Due to the high heat transfer coefficient of the bed material, efficient combustion is achieved, which means low emission levels of CO and NO_x. Key issues reported in the literature regarding CFB combustion include the need for fuel preparation to reduce the average size of the fuel particles. This preparative step is crucial for ensuring that the fuel remains fluidized during the combustion process [66]. In addition, a high content of alkali can induce agglomeration of the fluidized bed material, which in a worst case scenario can result in complete defluidization of the bed material [66] [67, 68].

Modern CFB boilers implement final heating of the steam in the loop seal region (see highlighted area in Figure 2.1). By installing the superheaters (FBHEs) in this region, direct contact between the superheater tube and the fluidized bed material is accomplished, resulting in superior heat transfer per unit area of the tube surface, as compared to the corresponding location of the superheaters in the convective pass [38, 69]. Having superheater tubes submerged in a bed of solids may, on the other hand, increase the risk for localized erosion, as described in more detail in Chapter V.

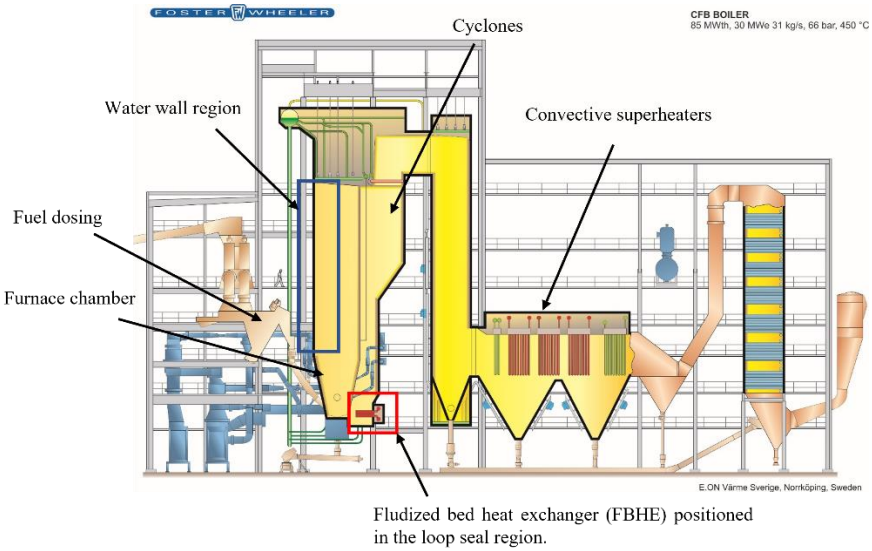

Figure 2.3: Schematic image of a circulating fluidized bed (CFB) boiler (courtesy of E.ON AB).

2.4 Waste-Derived Fuel

Approximately 50% of the electricity generated by WtE facilities in the EU comes from biodegradable sources. The other half stems from materials such as plastics, textiles, and

electronics, all of which originate from fossil fuels. A range of waste sources, encompassing agriculture, industry, and MSW, produces significant quantities of solid waste containing a substantial proportion of biodegradable organic material that is utilizable as combustion material [56].

2.4.1 Agricultural Residue

Agricultural residues account for around 27% of the total biomass used for heat and electricity production in the EU. Straw residue from grain production has been shown to be a viable fuel option for heat and power generation due to its cost-effectiveness, low moisture content and ease of transport in large bales [70]. However, utilizing biomass derived from vegetable crops poses technical challenges. Studies have indicated that the combustion of these crops results in a high alkali content, which can cause significant corrosion of the boiler equipment. Furthermore, the existence of alkali compounds increases the risk of significant particle agglomeration of the bed material within CFB boilers. This agglomeration arises from the creation of alkali silicates, which can ultimately result in the loss of fluidization of the bed material [66].

2.4.2 Recovered Waste Wood (RWW)

Recovered waste wood (RWW) comprises various wood types, primarily originating from construction and demolition activities, as well as commercial and industrial sources such as packaging and furniture. Compared to wood chips that originate from stem wood, this fuel type is relatively cheap and widely available, making it an attractive fuel for heat and electricity production. For instance, in Figure 2.4, a price comparison is depicted between wood chips and RWW in Sweden, showcasing that RWW is approximately twice as economically advantageous as wood chips.

However, RWW is notably complex with respect to its material composition, as it includes both material and chemical contaminants linked to its previous usage. As an example, RWW that has undergone surface treatment contains elevated concentrations of lead (Pb) compounds that originate from the pigments used in the surface treatments, including coatings, lacquers, drying agents and plastics. In addition, Pb- and Cl-containing RWW may arise from plastic components (polyvinyl chloride; PVC) derived from applications such as flooring and sheeting. These two chemical elements have been shown to increase dramatically the corrosion rates of waste-fired water walls. Kinnunen [71] has summarized the elemental compositions of 100 different RWW fuels used in waste-fired boilers in Europe and compared them with the composition of bark-less stem wood fuel. From that study, it was evident that RWW contains roughly a 480-fold higher level of Pb than stem wood, which was attributed to the surface compounds described above. A similar study was carried out by Krook et al [72] but instead the content of Pb in RWW was compared to the stem woods of pine and spruce. The results from that study showed that RWW used as fuel in the three largest heating plants in Sweden contain 480–1,638 times more Pb than stem wood that originates from pine and spruce trees.

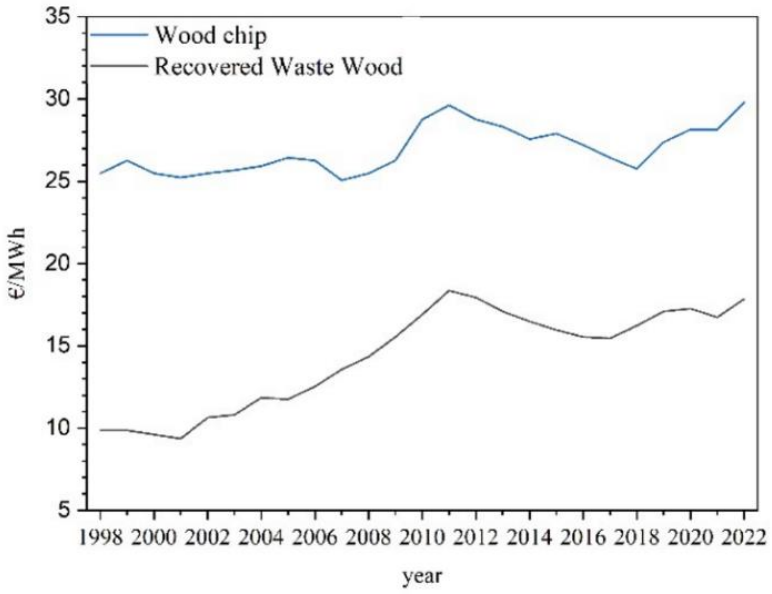

Figure 2.4: Prices of different wood residues in Sweden, expressed in EUR/MWh, collected from the Swedish Energy Agency [73].

2.4.3 Municipal Solid Waste

MSW traditionally originates from households, office buildings and state institutions (schools, nursery homes, government buildings etc.). According to Vainikka [74], who compiled several studies of MSW, for energy recovery, the major weight fractions of MSW globally comprise wood waste, textiles, paper and plastics. The origin of the Pb-containing compounds in MSW is commonly plastics in which Pb-containing compounds are used as stabilizers, while alkali chlorine compounds may derive from both renewable sources and PVC [74].

To summarize, WtE represents an attractive solution for mitigating waste disposal in landfills, while simultaneously contributing to the production of reliable, plannable, and sustainable electricity and heat by replacing the use of fossil fuel-based energy systems. In addition, compared to renewable energy systems such as wind and solar power, WtE offers a more-plannable and reliable energy system, which positions it as a valuable complementary technical solution [75].

Nevertheless, despite its promising benefits, there are notable technical hurdles that must be overcome for WtE to compete convincingly with fossil fuel combustion in terms of electrical efficiency. A critical issue is the accelerated corrosion rate of the heat-exchange components of the waste-fired boilers, such as the water-wall tubes and superheaters. This is attributed to the corrosive nature of the flue gas generated during waste combustion, which ultimately diminishes the electrical efficiency. Before venturing into the complex corrosion mechanism observed in waste-fired boilers, a brief introduction to the fundamentals of corrosion and metal oxidation at high temperatures is addressed in the following chapter.

Chapter III
Principles of High-Temperature Oxidation

Exposing a non-noble metal to high temperatures in an oxidizing environment inevitably results in the metal becoming oxidized. However, various factors can influence the characteristics of the oxide, including the alloy chemistry, temperature, partial pressure of oxygen, and the corrosive nature of the surrounding environment. By defining the thermodynamics and kinetics of metal oxide formation, it becomes possible to predict which oxide is formed and its protective properties in specific environments and at specific temperatures. This is vital for choosing the material and devising corrosion mitigation strategies for high-temperature applications such as WtE technologies.

3.1 Thermodynamics

The driving force for the oxidation of metals originates from the principle of the second law of thermodynamics [76]. Consider the following oxidation reaction between a metal (Me) and oxygen (O) where *x* and *y* are integers:

$$\mathrm{xMe(s)} + \frac{\mathrm{y}}{2}\mathrm{O_2(s)} \rightleftharpoons \mathrm{Me_xO_y(s)} \tag{3.1}$$

Assuming that the temperature (T) and pressure (P) are constant, it is possible to predict if the reaction is occurring spontaneously or not by calculating the change in Gibbs free energy (ΔG) of the reaction:

$$\Delta \mathrm{G} = \Delta \mathrm{H} - \mathrm{T}\Delta S \tag{3.2}$$

where H is the enthalpy, T is the temperature, and S is the entropy of the system. A negative value of the Gibbs free energy, ΔG<0, indicates that a spontaneous reaction is expected, i.e., the metal will undergo oxidation. Conversely, a positive ΔG value describes a thermodynamically impossible reaction, which means in this case that the metal will remain metallic, whereas if ΔG=0 the chemical reaction has reached equilibrium [77].

The Gibbs free energy per mole of oxygen can be expressed as follows:

$$\Delta \mathrm{G} = \Delta \mathrm{G}^\circ + \mathrm{RTln}\,\frac{\mathrm{aMe_xO_y}}{(\mathrm{a_{me}^x}) * \mathrm{a_O^{\frac{y}{2}}}} \tag{3.3}$$

where ΔG° is the standard Gibbs free energy, R is the universal gas constant, T is the temperature, and a represents the chemical activity of the reactant and products [78]. As the chemical activity of a pure solid substrate equals unity and the activity of any gas compound can be expressed as an ideal gas, Equation (3.3) in equilibrium (ΔG=0) can be rearranged as follows:

$$\Delta \mathrm{G}^\circ = \mathrm{RTln}\left(\mathrm{p_{O2}^{y/2}}\right) \tag{3.4}$$

where pO2 is referred to as the dissociation pressure of oxygen. As such, if a metal is subjected to a system in which $pO_{2system} > pO_{2diss}$, at a constant temperature, the metal will undergo oxidation [78].

The ΔG values for a large set of metals and the relative stabilities of the oxides as a function temperature are conveniently displayed in a so-called Ellingham-Richardson diagram (Figure 3.1). In this diagram, the intercept on the *y*-axis corresponds to the enthalpy change of the reaction (ΔH), while the slope is proportional to the entropy change (ΔS). Therefore, stable oxides, which are characterized by a highly negative ΔG value, are depicted by the lower lines in the diagram. The Ellingham-Richardson diagram also serves as a valuable tool for determining the minimum oxygen partial pressure of a system that is needed for the oxide to remain thermodynamically stable at equilibrium [78]. As an example, consider the exposure of pure Fe at 400°C in an oxidizing environment (see Figure 3.1). Initially, at a high partial pressure of oxygen, hematite (Fe_2O_3) will grow on the metal surface, given that $pO_{2system} > pO_{2dissFe2O3}$. As the oxide scale grows, an oxygen gradient forms over the oxide and in a region where $pO_{2system} < pO_{2dissFe2O3}$ a phase transformation from hematite to magnetite (Fe_3O_4) will occur.

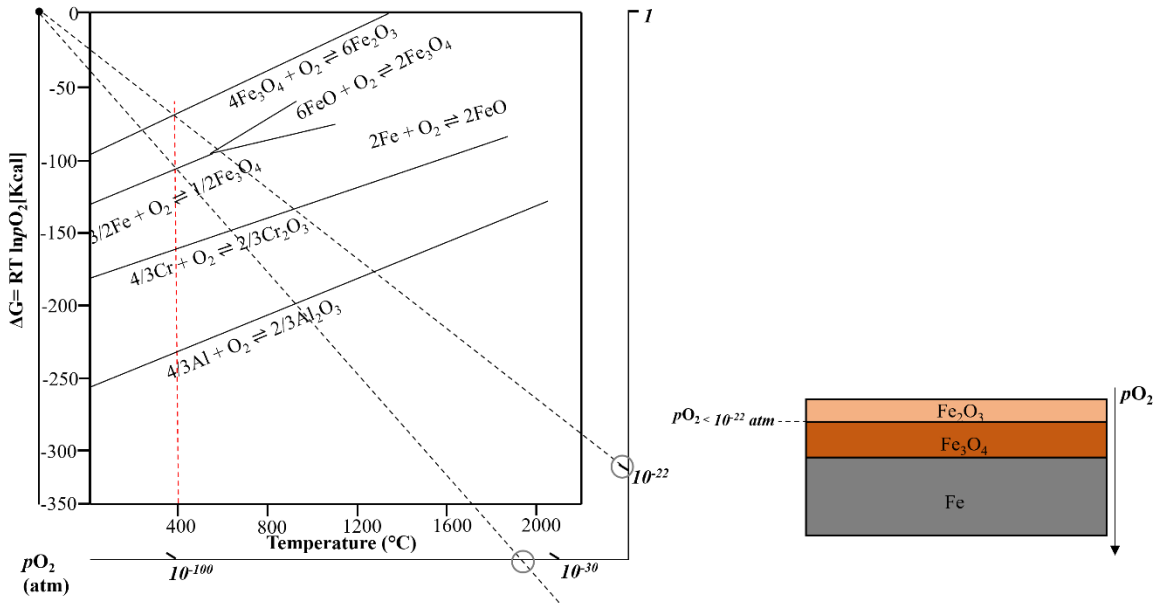

Figure 3.1: Left panel: Ellingham-Richardson diagram, adapted from [76]. Right panel: the multilayer oxide scale formed in pure Fe at 400°C. The position of the oxide scale is determined by the pO_2.

Thermodynamics can help us to understand if the formation of an oxide occurs spontaneously or not in a given environment. This is valuable information for designing alloys and predicting the alloy compositions needed for the formation of protective and selective oxides. However, discrepancies between prediction and observation are commonly observed when assessing oxidation from a purely thermodynamic perspective. The kinetics also needs to be taken into consideration to achieve a more-reliable assessment, as the diffusion rate of an alloying element and corrosive species through the oxide scale may alter the composition and stability of the formed oxide.

3.2 Kinetics

3.2.1 Oxide Growth

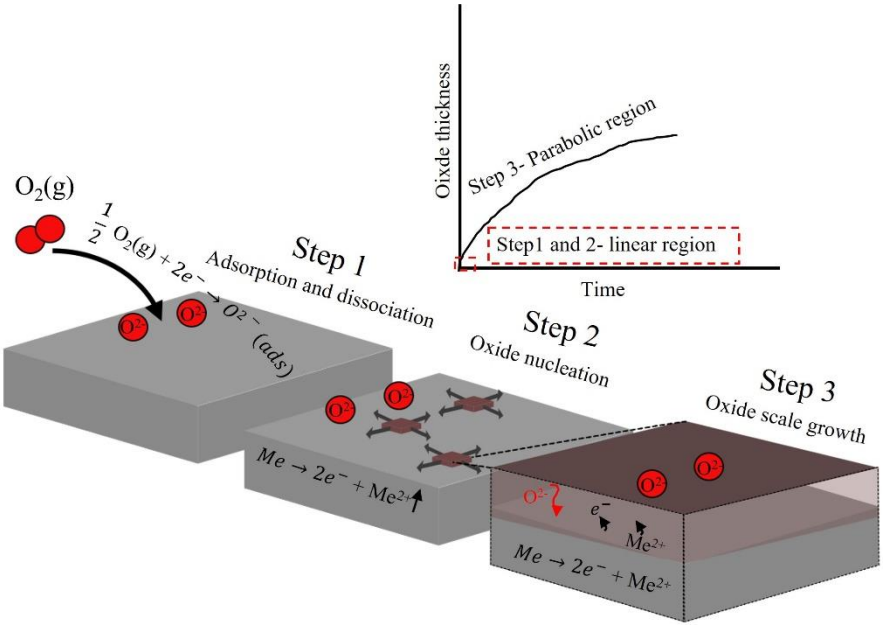

Figure 3.2: Oxide growth mechanism.

The formation and propagation of an oxide scale on a metal surface are commonly described in terms of a three-step process (Figure 3.2). In the initial step, oxygen from the surrounding environment is adsorbed on the metal surface, dissociate, and reduced to O^{2-} ions by electrons from the metal. In step 2, a reaction takes place when oxygen and metal ions come in contact, allowing the formation of individual oxide nuclei that will proceed to grow perpendicular to the metal surface until the entire surface is covered. Initially, the oxide thickness is assumed to be extremely thin, and the rate-limiting step of oxidation is considered to be represented by the reactions at the oxide scale/gas interface, i.e., the adsorption and dissociation of oxygen at the metal surface [76]. In this stage, the oxide growth is proportional to time and the kinetics of the reaction is said to conform to the linear rate law:

$$X = k_1 t \tag{3.5}$$

where X equals the oxide thickness, k is the rate constant, and t is time. In reality, steps 1 and 2 usually occur before any high-temperature corrosion test, as this thin oxide layer is readily formed even at room temperature. However, a linear oxide growth rate may also occur at high temperatures if the oxide diffusion barrier is not sufficient or breaks as will be discussed in Section 3.3. In step 3, the oxide layer fully covers the metal surface, effectively isolating the gas from direct contact with the metal. In this case, the solid-state diffusion of ions through the oxide scale becomes the rate-limiting step for oxide growth, and the growth rate is governed by a parabolic behavior that can be expressed as follows:

$$X^2 = K_p t + C \tag{3.6}$$

where X is the oxide thickness, Kp is the parabolic rate constant, t is time and C is an integer [76]. Since oxide growth rate in this stage is proportional to the square root of time ($X \propto t^{0.5}$), the growth rate of the oxide slows as time progresses. The parabolic growth rate model was first established

by Tammann [79] and further developed by Carl Wagner in 1930 [80]. The presented model is rather idealized, and several assumptions have been made, such as:

- Interface equilibrium between the gas/oxide and oxide/metal interface, as well as through the oxide.
- The oxide layer is adherend and compact.
- Oxide growth rate is driven by lattice diffusion of ionic species.
- Oxygen solubility in the metal is negligible.

The diffusion rate and path of charged species through an oxide scale at high temperatures are strongly influenced by the amounts and types of defects present in the oxide. Diffusion of charge species through the oxide can occur via either *lattice diffusion*, i.e., transportation of charged species via point defects in the lattice structure, or *short circuit diffusion*, whereby diffusion occurs along surface defects such as grain boundaries. The relative contributions of the two different types of diffusion processes are highly dependent upon the temperature [76].

Metal oxides are described as being stochiometric or non-stochiometric. In stochiometric oxides, the concentration of point defects is relatively low, and the defects do not influence the chemical composition of the oxide. The low concentration of defects, together with the poor electron conductivity, allows a rather slow diffusion of charged species through the oxide. This leads to the formation of slow-growing oxides with good protective properties, as exemplified by oxides such as α-Al_2O_3.

3.2.2 Lattice Diffusion in Stochiometric Oxides

The most-common point defects for stoichiometric oxides are Schottky and Frenkel pairs (Figure 3.3). In a Schottky defect, a pair of cationic and anionic vacancies in the crystal lattice is formed due to the movement of an atom from its original lattice position to the surface of the crystal. In this case, ionic conductivity arises due to the movement of vacancies through the crystal structure. A Frenkel defect arises as an atom moves from its original position to an interstitial site, leaving behind an atom vacancy. Ionic conductivity in this scenario relies on the so-called *interstitial diffusion mechanisms*, wherein interstitial ions hop to an adjacent equivalent site. Lattice diffusion may also arise when an atom positioned in an interstitial move to the lattice site, forcing the atom in the lattice site to move to the next interstitial site. This mechanism is called *interstitialcy diffusion* [76].

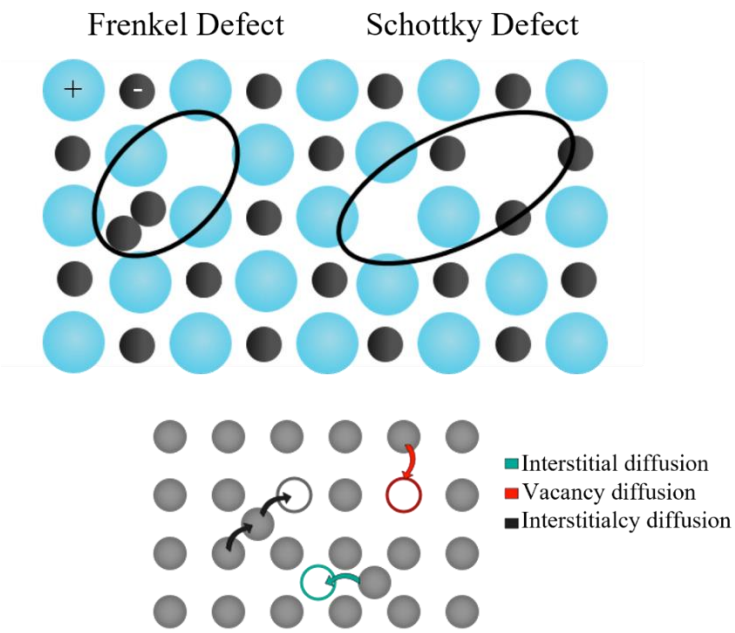

Figure 3.3: Illustration of Frenkel and Schottky defects for stochiometric oxides and diffusion mechanisms of the ions in the crystal lattice.

3.2.3 Lattice Diffusion in Non-Stoichiometric Oxides

Non-stochiometric oxides differ in composition from the stoichiometric oxides owing to a high concentration of defects that disrupt the expected atomic ratios. These defects may lead to either an excess or deficiency of metal/oxygen ions in the crystal lattice in the form of vacancies or occupation of ions in the interstitial sites, which facilitates a high diffusion rate of charged species through the oxide scale. As an example, $Fe_{1-x}O$ is a highly non-stoichiometric oxide with metal deficiency in the lattice structure, while NiO commonly encounters oxygen deficiency [78]. The transport of ions through the oxide occurs in a similar fashion, as described in Figure 3.3, namely by vacancy, interstitial or interstitialcy diffusion. Non-stoichiometric oxides can act as either p-type or n-type semiconductors, and their presence has a strong impact on the oxide growth direction (see Figures 3.4 and 3.5) [76].

- n-type oxides with an excess of cations in the crystal lattice allow predominately the diffusion of cations to occur, thereby promoting the formation of an outward-growing oxide (see Figure 10a). Alternatively, n-type oxides can be caused by anion vacancies. The anionic mobility is dominated by diffusion of the oxygen vacancy, promoting the formation of an inward-growing oxide (see Figure 3.4b) [76].

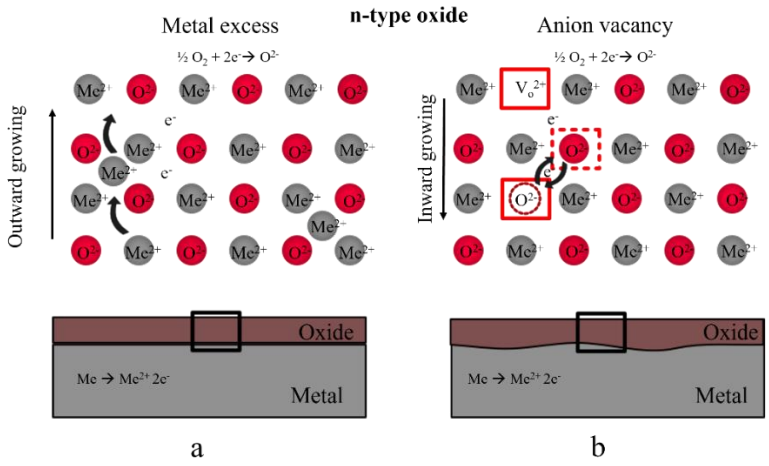

Figure 3.4: Simplified model of the diffusion mechanism of charged species in n-type oxides, showing a) metal excess and b) anion vacancy.

- For p-type oxides, an excess of anions in the interstitial sites may arise, leading to increased conduction of anions and promoting an outward-growing oxide. Finally, p-type oxides can emerge through metal vacancy in the lattice structure, allowing rapid diffusion of cations towards the oxide/gas interface and resulting in an outward-growing oxide (see Figure 3.5) [76].

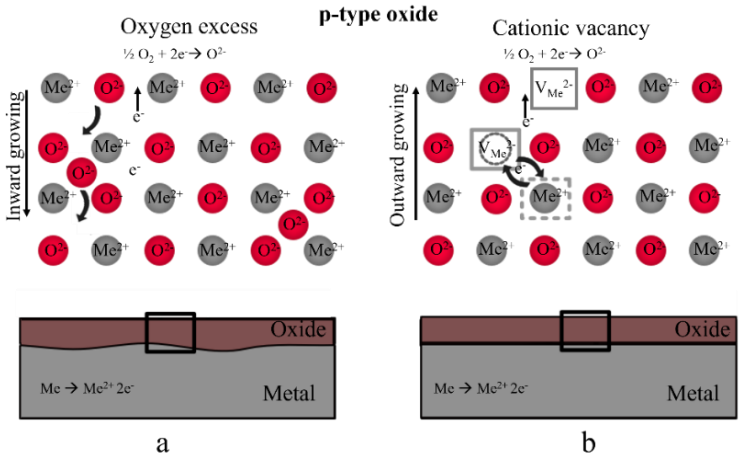

Figure 3.5: Simplified model of the diffusion mechanisms of charged species in p-type oxides, showing a) oxygen excess and b) cationic vacancy.

3.2.4 Short Circuit Diffusion via Grain Boundaries

A grain boundary represents the interface zone between two misoriented crystal structures, separating crystal regions that have distinct orientations. Considering that most metals and oxides are polycrystalline, the concentration of grain boundaries is rather significant and plays an important role in the diffusion rates of atoms and ions through the oxide scale. Concerning the influence of the grain boundaries, Kofstad [76] has proposed that the activation energy for ion diffusion via grain boundaries in alloys is 0.5–0.7-times lower than that required for lattice diffusion at temperatures 0.8-times the melting point of the alloy. Considering that the alloy types used in this work all have a melting point far above 1,000°C, these defects can be here regarded as rapid transport pathways through the oxide, as the exposures have been carried out at temperatures in the range of 400°–520°C [76].

3.3 Breakaway Corrosion

Alloys designed for use in high-temperature applications rely on the formation of a dense, firmly adhering, and slow growing protective oxide on the surface of the alloy, exemplified by oxides such as Cr_2O_3 and Al_2O_3. However, in waste-fired boilers, the environment is extremely dynamic and corrosive, resulting in rapid breakdown of the protective oxide scales. This is a result of interactions with the surrounding environment, resulting in depletion of Cr and Al from the oxide. If the alloy substrate cannot sustain the oxide with the alloy elements at the necessary rate, degradation of the primary protective oxide layer occurs. This results in the formation of a fast-growing, multilayer oxide with poorer protective properties, and consequent acceleration of the corrosion rate, which will lead to premature failure of the material. This phenomenon is called *breakaway corrosion*, and the sudden change in corrosion kinetics can be expressed as an increase in the parabolic rate constant, *Kp*, or as the transition to a linear growth rate of the oxide thickness (see Figure 3.6) [78].

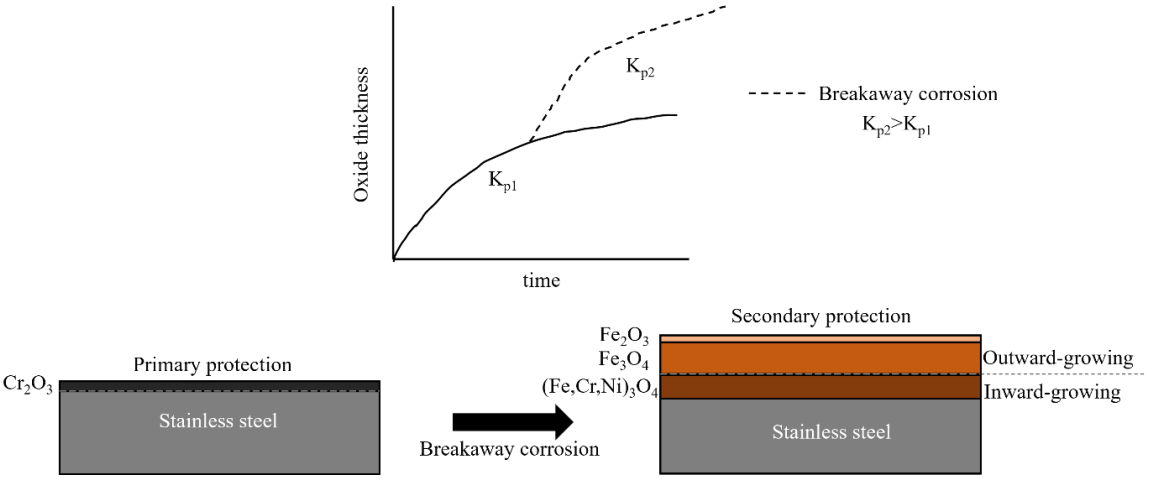

Figure 3.6: Breakaway corrosion on stainless steel.

A previous study [81] has demonstrated that stainless steel that is capable of forming a protective Cr-rich oxide in a mild environment undergoes breakaway corrosion already after 24 h of exposure in a commercial waste-fired boiler. This breakaway corrosion leads to the formation of a multilayer, outward-growing Fe-rich oxide and an inward-growing Fe,Cr,Ni spinel with debilitated protective properties.

Low-alloyed steel does not contain sufficient Cr to form Cr_2O_3, and the chemical composition of the oxide layers remains rather similar following breakaway corrosion, e.g., a multilayer, Fe-rich oxide structure. Nevertheless, several studies have shown evidence of a sudden kinetic transition upon exposure of a low-alloyed steel to aggressive salts. In this case, breakaway corrosion has been linked to different corrosion mechanisms that are capable of dissolving the oxide, or substantially diminishing the adhesion and density of the oxide scale, thereby facilitating rapid diffusion of charged species to the metal surface [82, 83]. As such, describing the protective properties of alloys based on their primary protective oxide is usually somewhat ”inappropriate” in the case of superheater and water wall application in waste-fired boilers. Therefore, recent studies regarding the development of materials for this application have investigated how different alloy elements enhance the protective properties of the alloy beyond breakaway corrosion [35, 84-87].

Chapter IV
Material Selection

Water-wall and superheater tubes serve as heat-exchange surfaces in waste-fired boilers. Their efficient and cost-effective performances over prolonged periods rely on specific attributes, including adequate resistance to high-temperature corrosion. To ensure this, a set of alloy types can be implemented. Depending on the chemical composition of the alloy, the temperature, and the surrounding environment, the protective properties of the oxide formed will vary. In this thesis, several different alloy classes relevant for waste-fired boiler applications has been studied. Descriptions of these alloy classes and the oxides that they can form are presented below. The mentioned oxides are limited to oxides relevant for this work.

4.1 Ferritic Low-alloyed Steel

Ferritic low-alloyed steel is an Fe-stabilized alloy with a body-centered cubic (BCC) crystal structure. It is commonly employed as a material for water-wall tubes due to its low cost and favorable mechanical properties, such as creep strength up to approximately 500°C. The addition of minor alloying elements is designed to enhance the corrosion resistance and mechanical strength of the steel substrate. Thus, Mo and C are frequently utilized as alloying elements to improve the mechanical properties of the material, while Cr is incorporated to improve the material's resistance to corrosion. Nevertheless, the amount of Cr added is not sufficient to form a Cr-rich oxide; instead, a multilayer, Fe-rich oxide is formed [76, 88, 89].

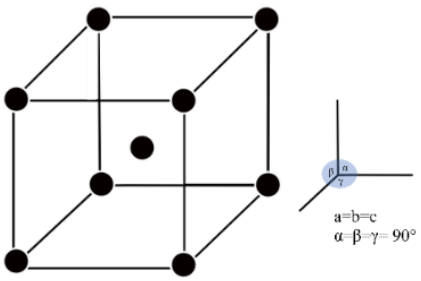

Figure 4.1: Body-centered cubic (BBC) crystal structure.

4.1.1 Oxide Formation on Ferritic Low-alloyed Steel

- *Wüstite ($Fe_{1-x}O$)*

Wüstite possesses a halite crystal structure in which the oxygen anions are closely packed and the divalent Fe ions occupy the octahedral interstitial sites. It is considered a poorly protective oxide due to its low stoichiometry and, thus, high concentration of defects. Moreover, Wüstite is only thermodynamically stable at temperatures above 570°C. In addition, the addition of a small amount of Cr to the alloy may shift the stability of Wüstite to even higher temperatures and, as such, it is not anticipated to form in this work [88].

- *Magnetite (Fe_3O_4)*

Magnetite crystallizes as an inverse spinel and is commonly assigned the following formula: $Fe^{3+}_{tetr}(Fe^{2+}Fe^{3+})_{oct}O_4^{2-}$. The oxygen anions are positioned at the lattice sites, while the cation

occupies both the tetrahedral and octahedral holes. As such, the crystal is face-centered cubic, whereby 1/8 of the tetrahedral sites is occupied by the trivalent cation (Fe^{3+}) and the octahedral holes are shared by Fe^{3+} and Fe^{2+}. Magnetite shows metal deficiency at high partial pressures of oxygen, leading to metal vacancy formation with p-type semiconductor behavior. Conversely, under low partial pressures of oxygen, a metal-excess structure may arise that allows transformation to an n-type semiconductor [76] [88]. However, compared to Wüstite, the defect concentration is significantly lower, resulting in superior protective properties.

- *Mixed spinel $(Fe,Cr)_3O_4$*

The trivalent iron ion in magnetite may be partially replaced by another alloy element, such as Cr^{3+}, which leads to the formation of a mixed inverse spinel. As such, Cr^{3+} competes with Fe^{3+} to fill the trivalent interstitial sites and may occupy a maximum of 67% of the total interstitial sites occupied [76]. This oxide is typically inward-growing.

- *Hematite (Fe_2O_3)*

Hematite possesses a corundum crystal structure with densely arranged Fe^{3+} ions occupying two-thirds of the octahedral sites of a hexagonal, close-packed unit cell. Given its limited content of point defects, hematite is regarded as the most protective of the Fe-rich oxides discussed in this work.

4.2 Austenitic Stainless Steel

When compared to low-alloyed steel, the Cr content of stainless steel is considerably higher (roughly 10–25 wt.%), which facilitates the formation of a slow-growing Cr-rich oxide with strongly protective properties at high temperatures and in a mildly corrosive environment. The presence of approximately 8%–12% Ni in stainless steel stabilizes its austenitic structure (FCC crystal structure), contributing to its ductile properties. In addition, previous studies have shown that the incorporation of Ni plays an important role in mitigating the corrosion rates of stainless steels in alkali chlorine environments at high temperatures following breakaway corrosion [85]. Furthermore, favorable weldability is anticipated for this type of alloy [89-91].

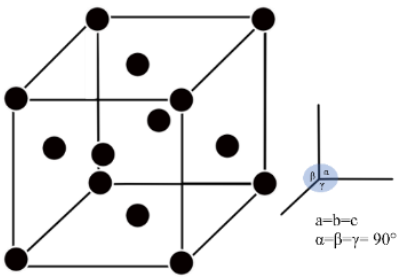

Figure 4.2: Face-centered cubic (FCC) crystal structure.

4.2.1 Oxide Formation on Austenitic Stainless Steel

- *Eskolaite (Cr_2O_3)*

Stainless steels contain sufficient Cr to form Eskolaite (Cr_2O_3) at high temperatures and in a non-corrosive environment. Eskolaite adopts a corundum structure with a hexagonal closely packed structure with 2/3 of the octahedral interstitial sites being occupied by the trivalent cation.

Compared to Fe-rich oxides, Cr_2O_3 offers significantly better corrosion protection, mainly due to its low ion mobility and dense oxide structure. However, many studies have reported that this oxide can break already after a short exposure in waste-fired boilers for superheater applications [81].

- *Corundum solid solution $(Fe,Cr)_2O_3$*

In stainless steel, most of the alloy elements comprise Fe. Due to their isostructural properties and associated solubilities, Fe_2O_3 and Cr_2O_3 can form solid solution that is stable at high temperature and that retains the corundum crystal structure. Depending on the concentration of soluble Fe^{3+} ions in the mixed corundum structure, the oxide can behave as either an n-type or a p-type semiconductor [92].

- *Mixed spinel $(Fe,Cr,Ni)_3O_4$*

Fe, Cr and Ni may form a mixed normal spinel solid solution in which divalent Fe ions are substituted with Ni^{2+} and Cr replaces trivalent Fe ions in the octahedral site. This oxide is commonly inward-growing and is present after breakaway corrosion in an oxidizing environment. The characteristic of the oxide primarily relies on the concentrations of Fe, Cr and Ni in the spinel structure [92] .

Upon breakaway corrosion, the stainless-steel may also form outward-growing, Fe-rich oxides [93].

4.3 Ni-based Alloys

Ni-based alloys, which consist primarily of Ni, are commonly alloyed with 10–15 wt.% Cr, which facilitates the formation of Cr_2O_3. These alloys have an austenitic microstructure and have excellent weldability and corrosion protective properties, which makes them attractive candidates for coating and overlay weld applications at high temperatures. Enhancement of mechanical strength is achieved by precipitation hardening or solution hardening through the addition of different alloy elements, such as titanium, aluminum, molybdenum, cobalt and tungsten. Today, it is rather common to apply a Ni-based alloy overlay onto low-alloyed steel in water-wall applications, to ensure enhanced corrosion resistance of the water-wall tubes in waste-fired boilers [94]. However, due to the high Ni-content, these materials can exceed the price of low-alloyed steel by a factor of 10.

4.3.1 Oxide Formation in Ni-based Alloys

- *Nickel oxide $(Ni_{1-y}O)$*

Compared to Cr_2O_3, $Ni_{1-y}O$ is a rather poor protective oxide, as it has a high concentration of defects due to the presence of metal vacancies, which means that it acts as a p-type semiconductor. It displays a rock salt structure with metal ions occupying the octahedral sites of the crystal lattice.

As mentioned above, the primary protective oxide formed for Ni-based alloys consists of Cr_2O_3. Nonetheless, when breakaway corrosion occurs, other alloy elements, such as Ni and Fe, start to oxidize, leading to the formation of oxides such as NiO and $(Fe,Cr,Ni)_3O_4$ spinel.

4.4 Ferritic FeCrAl Alloys –Possible Candidates for Heat Exchangers in Waste-Fired Boilers?

Ferritic FeCrAl alloys have the BCC structure and are highly regarded for their exceptional corrosion resistance properties in the temperature range of 900°–1,300°C. This is primarily attributed to their ability to form α-Al_2O_3, which is a thermodynamically stable oxide with high stoichiometry, such that it enables slow diffusion of chemical species thorough the oxide. However, superheater tubes in waste-fired boilers commonly operate at temperatures in the range of 350°–475°C. In this temperature interval, α-Al_2O_3 is not thermodynamically stable, leading to the formation of transient, mixed Al_2O_3 [89, 95].

The concentrations of Al and Cr alloying elements are important with respect to their mechanical and corrosion resistance properties. By lowering the Cr content to roughly 10–-15 wt% and the Al content to a maximum of 4 wt.%, sufficient Cr is acquired to facilitate the formation of a Cr-rich oxide, while avoiding α-α′ phase separation, which is caused by a miscibility gap in the Fe-Cr system. The formation of the α′ phase involves the spontaneous phase separation of the ferritic phase to a Cr-rich and a Fe-rich phase, leading to the material acquiring unwanted brittleness. The novel FeCrAl alloys developed by Kanthal used in this study have been designed specifically to avoid α-α′ phase separation at temperatures as low as 300°C, while retaining good corrosive properties. Thus, this makes these alloys interesting candidates for superheater applications in waste-fired boilers.

As mentioned in the previous chapter, breakaway corrosion is commonly observed after a short operational time for water-wall and superheater materials in waste-fired boilers. For FeCrAl alloys at these temperatures, this means that rapid degradation of the primary protective Al-rich oxide occurs and, instead, a multilayer oxide is present that has inferior protective properties. This multilayer oxide commonly comprises an outward-growing, Fe-rich oxide and an inward-growing Fe,Cr,Al spinel. Previous studies have shown that improved corrosive properties following breakaway corrosion can be obtained for these alloys through the addition of alloy elements, such as Si, Al and Cr. In fact, studies conducted by Eklund and coworkers have shown that the addition of small amounts of Si to FeCrAl alloys ensures corrosion rates similar to those of Ni-based alloys, when exposed to a waste-fired grate boiler for 672 h, such that these alloys are interesting candidates for superheater applications [95]. However, FeCrAl alloys do not currently have the acquired pressure-loading properties for use as base materials for superheater applications, and should be regarded as possible coating or weld overlay materials. As such, FeCrAl alloys have great potential for biomass and waste-fired boiler applications, as they could significantly reduce the material cost by substituting Ni-based alloys as coating material for superheater applications.

Aluminum-containing alloys exposed to high temperatures in environments that contain nitrogen may undergo Al-nitridation. For instance, gaseous N_2 can adsorb to the oxide surfaces of superheaters, dissociate, and diffuse into the metal surface, where it dissolves and reacts with Al to form aluminum nitride (AlN). From the corrosion point-of-view, this may lead to premature oxide scale failure because the formation of AlN precipitates leads to depletion of Al component from the alloy, thereby hindering the replenishment of Al, which is needed for the primary oxide layer (Al_2O_3) to remain intact during corrosive events. N_2 is a relatively stable molecule, and in presence of a pure alumina scale, dissociation of N_2 is unlikely to occur. However, studies performed by

Geers et al (88) and Sand et al (89) have shown that the formation of surface defects on α-Al_2O_3 scales exposed to high temperatures and in an environment with low oxygen activity, may provide a diffusion pathway for nitrogen ions to the metal surface, leading to local AlN formation [96, 97]. Internal nitridation of FeCrAl alloys have also been observed when exposed to alkali chlorides at high temperatures and in an oxidizing environment [98].

Chapter V
Corrosion Mechanisms in Waste-Fired Boilers

The focus of this work is to examine the corrosion mechanisms caused by $PbCl_2$ in a water-wall environment and the degradation mechanism for superheaters located in the loop seal of waste-fired CFB boilers. Comprehending the mechanism of $PbCl_2$-induced corrosion in water-wall regions and the synergy between erosion and corrosion in loop seal superheaters is crucial for constructing reliable models that can predict the lifespans of materials used in these applications. Various corrosion mechanisms have been proposed to influence significantly the deterioration rates of water walls and superheaters in waste-fired boilers, and these will be discussed in detail in this chapter.

5.1 Chorine-Induced Corrosion

It is widely acknowledged that Cl-containing compounds contribute to the severe corrosion of water-wall tubes and superheaters in biomass- and waste-fired boilers. Although the results are clear, the mechanism underlying the corrosion attack remains a subject of debate.

The active oxidation mechanism, also known as the chlorine cycle, was first suggested by Mcnallan [99] and subsequently refined by Grabke [100] . This mechanism suggests that gas-phase transportation of Cl_2 molecules through an oxide scale plays an important role in the degradation rates of various types of alloys [100]. It is argued that gaseous $Cl_2(g)$ may form from the oxidation of HCl or from the reaction of alkali chlorides on the metal oxide surface:

$$2HCl(g) + \frac{1}{2}O_2(g) \rightleftharpoons H_2O(g) + Cl_2(g) \tag{5.1}$$

$$2NaCl(s) + Fe_2O_3(s) + \frac{1}{2}O_2(g) \rightleftharpoons Na_2Fe_2O_4(s) + Cl_2(g) \tag{5.2}$$

It is then further argued that the formed $Cl_2(g)$ diffuses through the oxide scale via micro-cracks and pores and reacts with the metal substrate at the oxide/metal interface, forming metal chlorides ($MeCl_x$) [100]:

$$\frac{x}{2}Cl_2(g) + Me(s) \rightleftharpoons MeCl_x(s) \tag{5.3}$$

Due to the considerably high vapor pressures of metal chlorides, continuous evaporation takes place, which allows rapid diffusion of gaseous metal chlorides outwards towards the oxide/gas interface. As an oxygen concentration gradient develops throughout the oxide scale, the metal chlorides will eventually reach a region of sufficiently high pO_2 to promote the oxidation of metal chlorides, resulting in the formation of a porous, poorly protective, Fe-rich oxide and the release of $Cl_2(g)$. It is argued that the released $Cl_2(g)$ can act as a corrosion catalyst, re-entering the oxide scale and repeating the reactive steps described above:

$$yMeCl_x(g) + \frac{z}{2}O_2(g) \rightleftharpoons Me_yO_z(s) + \frac{xy}{2}Cl_2(g) \tag{5.4}$$

However, certain aspects of the proposed mechanism are subjects for debate. For instance, to establish favorable conditions for metal chloride formation at the metal/oxide interphase, rapid diffusion of Cl_2(g) and metal chlorides(g) through the oxide is assumed, whereas oxygen molecules simultaneously retain significantly lower mobility. Furthermore, as mentioned before, it has been assumed that diffusion occurs via cracks and pores. However, this assumption raises important questions, given that the molecular length of O_2 is less than that that of either Cl_2 or $MeCl_x$. Consequently, micro-cracks and pores should also promote rapid diffusion of oxygen, thereby promoting an environment that makes metal chlorides thermodynamically unstable. In addition, prior to breakaway corrosion, the oxide scales are commonly adherent with a low concentration of cracks and voids, which makes it even more difficult to explain the suggested rapid diffusion route of the chlorinating agent. When further discussing the relationship to water-wall and superheater corrosion, it is important to note that the high content of water vapor, combined with the oxidizing environment commonly observed in the flue gases of waste-fired boilers, promotes the formation of HCl rather than Cl_2 and, thus, a low concentration of Cl_2 is expected [93].

In light of this, Folkeson et al [101] have proposed an electrochemical approach to elucidate the diffusion mechanism of chlorine during high-temperature corrosion. In the proposed reaction mechanism, Cl_2(g) is suggested to form through the oxidation of HCl (the Deacon process) in a gas composition that contains water at the ppm level, as shown in the following reaction:

$$2\,HCl(g) + \frac{1}{2}\,O_2(g) \rightleftharpoons Cl_2(g) + H_2O(g) \tag{5.5}$$

It is then argued that the Cl_2 molecule dissociates at the oxide scale surface and reduces, forming Cl ions. Subsequently, metal oxidation takes place at the oxide scale/metal interface, thereby supplying the Cl molecule with the necessary electron current to facilitate Reaction (5.6):

$$Cl_2(g) + 2e^- \rightarrow 2Cl^-(ads) \tag{5.6}$$

$$Me(s) \rightarrow Me^{n+} + ne^- \tag{5.7}$$

It is also proposed that Cl ions can be formed by the deprotonation of adsorbed HCl on the oxide surface, as shown in Reaction (5.8). Here, the cathodic current is generated through the reduction of oxygen rather than chlorine [101].

$$2HCl(ads) + \frac{1}{2}O_2(ads) + 2e^- \rightarrow 2Cl^-(ads) + H_2O(g) \tag{5.8}$$

Given the relatively low charge and large size of Cl ions, it is unlikely that the Cl ions will exchange positions with oxygen ions in the oxide crystal lattice. In addition, surface-located Cl ions are expected to have higher mobilities than oxide ions, due to the aforementioned properties. As such, rather than gas-phase diffusion of chlorine via cracks and pores, as suggested by the chlorine cycle mechanism, Folkeson et al [101] have argued that diffusion of Cl ions takes place via grain boundary diffusion towards the metal/oxide interface. Metal chlorides are expected to form throughout the oxide surface rather than exclusively at the metal-oxide interface. The location of the metal chlorides in the oxide scale is suggested to depend on the speed of the inward and outward diffusion of Cl ions and metal ions, respectively [101]. However, more recent work carried out by

Cantatore et al [102], employing a combination of experimental work and first-principle modeling of Cl ion diffusion within an oxide scale, has revealed that diffusion through the oxide scale by Cl ions that originate from KCl is energetically favored if it follows the path of oxygen vacancies in the bulk oxide. As a result, the referred work introduces an alternative diffusion pathway, namely via lattice diffusion, to that suggested by [102].

5.2 Chromate Formation

In the cases of alloy types that contain sufficient amounts of Cr, such as FeCr, FeCrNi and FeCrAl, the level of corrosion resistance is linked to the ability of the material to retain its protective Cr-rich oxide. As such, the corrosion mechanisms of Cr-forming alloys cannot be explained solely in terms of Cl-induced corrosion. Chromia depletion from the oxide scale has been associated with alkali chlorides, which are commonly observed at high concentrations in the deposits on heat-exchange surfaces in waste-fired boilers [58]. Experimental studies carried out by Grabke and coworkers on stainless steel exposed to NaCl at 600°C and 700°C in an oxidizing environment suggest that NaCl reacts with the protective chromia scale to form sodium chromate and Cl_2 [100]:

$$4NaCl(s) + Cr_2O_3(s) + \frac{5}{2}O_2(g) \rightleftharpoons 2Cl_2(g) + 2Na_2CrO_4(s) \tag{5.9}$$

The released $Cl_2(g)$ is suggested to participate in the propagating corrosion step via the active oxidation mechanism described in the previous section, forming a very loose and porous oxide that consists mainly of Fe_2O_3. The conclusion of the authors is that chromate formation only acts as a source of the Cl_2-formation needed for the chlorine cycle to activate, which is designated as the main corrosion mechanism [20]. But what about the effect of breaking the protective chromia scale itself? This matter has been addressed by several authors who have studied the roles of the cations K^+, Na^+ and Ca^+ in KCl-, NaCl- and $CaCl_2$- induced corrosion of FeCr, FeCrNi and FeCrAl. It has been reported that the corrosion attack is initiated by the formation of alkali chromates, leading to rapid depletion of Cr_2O_3, which gives rise to the formation a poorly protective, multilayer oxide. Pettersson et al [103] have elucidated the role of alkali ions in high-temperature corrosion of stainless steel by carrying out experiments on stainless steel that was exposed to a set of alkali compounds, including both Cl-containing (KCl) and chlorine-free (K_2CO_3) salts, in a humid environment at 500°C and 600°C. Based on their observations, it was suggested that the rapid corrosion rate was initiated by the breakdown of the protective Cr-rich oxide scale, which was triggered by the formation of potassium chromate:

$$\frac{1}{2}Cr_2O_3(s) + 2KCl(s) + H_2O(g) + \frac{3}{4}O_2(g) \rightleftharpoons K_2CrO_4(s) + 2HCl(g) \tag{5.10}$$

$$\frac{1}{2}Cr_2O_3(s) + K_2CO_3(s) + \frac{3}{4}O_2(g) \rightleftharpoons K_2CrO_4(s) + CO_2(g) \tag{5.11}$$

From the results of that study, it was shown that K_2CO_3 is as corrosive as KCl and displays a similar oxide morphology. As such, this study strongly implies that the initial corrosion attack is strongly related to chromate formation, as opposed to being only influenced by chlorine.

Chromia depletion has also been associated with $PbCl_2$. Experimental studies carried out by Spiegel et al on stainless steel exposed to $PbCl_2$ at 500°C and 600°C in an oxidizing environment suggest

that $PbCl_2$ in the molten phase reacts with the protective chromia scale to form lead chromate and Cl_2 [20]:

$$2PbCl_2(l) + Cr_2O_3(s) + \frac{5}{2}O_2(g) \rightleftharpoons 2Cl_2(g) + 2PbCrO_4(s) \quad (5.12)$$

It has been suggested that the released Cl_2 gas participates in the propagating corrosion step via the active oxidation mechanism described in the previous section, forming an outward-growing porous Fe_2O_3 oxide and an inward-growing $FeCr_2O_4$ spinel as corrosion products. Bankiewicz and colleagues carried out experiments on stainless steel exposed to $PbCl_2$ at temperatures below the melting temperature of $PbCl_2$ [33]. A similar outcome was observed, but rather than attributing rapid corrosion solely to active oxidation, it was proposed by the authors that the initial step in the corrosion process was the breakdown of the protective chromium scale by lead chromate formation, which would allow rapid diffusion of oxygen and Cl through the damaged oxide, forming metal chlorides via the active oxidation mechanism. In addition, the findings of Bankiewicz et al (23) highlight that the formation of $PbCl_2$ melt is not a prerequisite for chromia depletion to occur, as chromia depletion was observed at temperatures below the melting point of $PbCl_2$.

5.3 Chromium Evaporation

Chromium evaporation has been studied extensively at high temperatures for various alloys. It has been shown that when a Cr-rich oxide is exposed to an environment that contains water vapor and oxygen, a chemical reaction occurs in which chromic acid [$CrO_2(OH)_2$ (g)] is formed, leading to depletion of the Cr-rich oxide:

$$Cr_2O_3(s) + 2H_2O(g) + \frac{3}{2}O_2(g) \rightarrow 2CrO_2(OH)_2(g) \quad (5.13)$$

The rate of Reaction (5.13) is highly dependent upon the partial pressures of H_2O and O_2 and the gas flow over the system.

5.4 $PbCl_2$-Induced Corrosion on Low-Alloyed Steel

Concerns regarding the corrosive effects of Pb-containing compounds in waste-fired boilers were already discussed in the late 1960s [104]. Since then, several studies have observed increased concentrations of $PbCl_2$ in the deposits on the water-wall tubes of waste-fired boilers, and this phenomenon has been correlated to severe corrosion issues. Depending on the composition of the deposit and the type of material being exposed, different mechanisms for $PbCl_2$-induced corrosion have been suggested in the literature. Since the work presented in this thesis is primarily aimed at investigating the mechanisms of $PbCl_2$-induced corrosion of low-alloyed steels in water-wall environments, the literature review will focus on this type of material class and condition.

In the 1986 National Waste Processing Conference, Daniel and colleagues presented their observations of deposits that were collected from the furnace wall of a waste-fired boiler [105]. High concentrations of heavy metal compounds, such as $PbCl_2$, were detected in the deposits, and it was argued that they play an important role in the corrosive environment. Indeed, the authors suggested that alkali chlorides, which were originally argued to be the primary source of waste-fired corrosion, could not be the only reason for the highly corrosive environment [105]. Instead,

they proposed that heavy metal chlorides such as $PbCl_2$ interact with alkali chlorides and thereby decrease the melting point of the formed deposit, leading to the formation of molten salt compounds. The formation of molten salts may significantly accelerate the corrosion rate of the material, in what is today described as *molten phase corrosion*. Molten salts act as electrolytes that facilitate the rapid diffusion of ions through the deposit and towards the oxide surface, in contrast to the solid-state interaction, which leads to a more-aggressive corrosion attack. Moreover, studies have shown that melt-induced corrosion can promote the dissolution of the protective oxide scales, resulting in rapid corrosion [20].

One of the earlier laboratory-scale studies investigating the role of $PbCl_2$ in the corrosion of low-alloyed steel (10CrMo910) was carried out by Spiegel et al in 1999 [20]. In that study, the low-alloyed steel was exposed to $PbCl_2$ for up to 360 h at 500°C and 600°C in an environment containing 5 vol.% O_2 + He and water content less than 10^{-4} bar. A significant increase in the corrosion rate was observed compared to samples exposed without the presence of $PbCl_2$. From the microstructural analysis of the corrosion product, a poorly adherent, multilayer oxide was observed. In the suggested reaction mechanisms, $PbCl_2$ is expected to be in a completely molten state at both of the tested temperatures and dissolve the formed iron-rich oxide (Fe_2O_3) at the melt/scale phase boundary, resulting in the formation of metal chlorides ($FeCl_x$). The metal chlorides are then suggested to evaporate and oxidize, forming a multilayer iron-rich oxide while simultaneously releasing Cl_2(g), were the latter product is argued to act as an corrosion catalyst as described in the active oxidation mechanism [20].

Subsequently, more-complex experimental frameworks have been formulated. These are concerned with the interactions of $PbCl_2$ with other salts and compounds commonly found in the deposits on the water-wall tubes in waste-fired boilers. Numerous works regarding $PbCl_2$-induced corrosion on low-alloyed steel in waste-fired boiler environment have been conducted at Åbo Akademi. A lot of their research has involved simulating the RWW waste-fired boiler environment in the water-wall region, which involves extensive laboratory work, field exposures and thermodynamic calculations. In many of their reported results, accelerated corrosion attacks on low-alloyed steel was attributed to the formation of Pb-containing melts originating from $PbCl_2$ salt/compound mixtures and corrosion products [22, 28, 34].

However, studies have revealed that molten $PbCl_2$ or eutectic melt mixtures of $PbCl_2$-containing salts are not necessarily a prerequisite for accelerated corrosion to occur on low-alloyed steels. A previous laboratory-based study carried out by Bankiewicz et al [106] on the corrosivity of Pb-containing salt mixtures for low-alloyed steel (10CrMo910) revealed the extreme activity of pure $PbCl_2$. In the referred study, the low-alloyed steel was exposed to different $PbCl_2$ salt mixtures at 400°C, 500°C and 600°C for 168 h in air. At 400°C, severe corrosion rate was apparent for $PbCl_2$ with no indication of any melt fraction present. Furthermore, there were no significant differences in the corrosion rates of samples exposed to pure $PbCl_2$ or a mixture of $PbCl_2$-KCl, suggesting the high reactivity of $PbCl_2$. It was argued that at 400°C the degradation of the steel was primarily driven by the presence of $PbCl_2$, which was suggested to destroy the presumably primary protective Cr_2O_3 oxide by forming $PbCrO_4$ [106]. However, this conclusion is questionable, as the steel compound only contains 2.2 wt.% Cr, raising doubts about the likelihood of Cr_2O_3 formation under these conditions. Significant increases in the corrosion rates of both pure $PbCl_2$ and $PbCl_2$ salt mixtures were observed in the temperature range of 500°–600°C, which were attributed to melt formations.

In another laboratory study carried out by Bankiewicz et al [33], a highly aggressive corrosive attack occurred on a low-alloyed steel exposed to $PbCl_2$ at a temperature of 450°C. The exposures were conducted both above (550°C) and below (350°C and 450°C) the melting point of $PbCl_2$ (501°C). At 350°C, the corrosion rate in the presence of $PbCl_2$ was low, while at both 450°C and 550°C significantly high corrosion rates were observed within a similar range. At 550°C, the resulting corrosion morphology revealed a thick multilayered scale with the formation of cracks and voids. Chlorine was detected primarily in the metal/scale interface, whereas Pb was detected further out in the oxide scale, in association with the Fe oxide. Unfortunately, no SEM/EDX analysis was presented for the corroded sample exposed at 450°C in the presence of $PbCl_2$. That study also involved exposures with PbO and without any deposit. For the sample exposed to PbO at 550°C, a low corrosion rate was observed, although it was higher than that of the sample exposed without deposit. Lastly, the authors suggested that $PbFe_2O_4$ had formed on both the $PbCl_2$ and PbO deposited samples after 168 h of exposure, as indicated by SEM/EDX analysis. Unfortunately, no SEM/EDX analysis was shown for the corroded sample exposed at 450°C and no corrosion mechanisms were proposed in the study of the low-alloyed steel sample [33].

Most of the laboratory studies presented in the literature regarding $PbCl_2$-induced corrosion have been carried out in air. However, the flue gas formed during the combustion of waste is usually rather humid, which may affect the corrosion rates and mechanisms of the exposed surfaces. Larsson et al have studied $PbCl_2$-induced corrosion of a low-alloyed steel (10CrMo910) at a temperature of 400°C in 5%O_2 + 20%H_2O for 24h [83]. The authors observed an accelerated corrosion rate for the material in the presence of $PbCl_2$, as compared with the corresponding sample exposed without $PbCl_2$. Upon analyzing the microstructure of the exposed sample, it was revealed that a localized accelerated corrosion attack occurred in close proximity to the locations of the original $PbCl_2$ crystals. In addition, severe spallation was noted in this region. According to the authors, this behavior is attributable to the observed rapid formation of PbO during the exposure, which releases HCl(g) according to Reaction (5.14):

$$PbCl_2(s) + H_2O(g) \rightleftharpoons PbO(s) + 2HCl(g) \quad (5.14)$$

The authors have further argued that the released HCl(g) contributes to the formation of metal chlorides at the metal/oxide interface. The formation of metal chlorides is suggested to reduce the adhesion between the metal substrate and oxide, thereby facilitating the rapid diffusion to the metal surface of corrosive elements located close to the original $PbCl_2$ particles. In this work no further explanation or discussion regarding the roles of Pb and PbO on the propagating mechanism of $PbCl_2$-induced corrosion was out forward.

In the literature on $PbCl_2$-induced corrosion of low-alloyed steels in the waste-fired boiler environment, it has been reported that $PbCl_2$ accelerates the corrosion rate of the material through the formation of low-temperature eutectic or partial melts, in what is commonly described as *molten phase corrosion*. However, laboratory studies have also shown that an increased corrosion rate is possible for low-alloyed steels in the presence of pure $PbCl_2$ in the absence of melt formation. Today, most of the literature lists the release of Cl and the active oxidation mechanisms as the main reasons for the significant attack of $PbCl_2$ on low-alloyed steel. Although the high corrosion rate of $PbCl_2$ is apparent in both humid and dry environments, the underlying mechanism remains unclear, and very little attention has been paid to the role of Pb in the initiation and propagation steps of $PbCl_2$-induced corrosion of low-alloyed steels.

5.5 Corrosion and Erosion of Fluidized Bed Heat Exchangers

As mentioned in Section 2.3, in newly developed CFB boilers, FBHE have been positioned in the loop seal position of the boiler. This means that more steam data can be collected, as higher steam temperatures can theoretically be utilized. This is because the majority of the flue gas is separated from this region of the boiler, which creates a region that has a reduced corrosive environment. In addition, the superheater is immersed in the fluidized bed material, resulting in high heat transfer rates between the bed material and superheater tubes. Thus, it is possible to reduce the material cost significantly in this area, as the superheater tubes can be reduced in size while still providing valuable steam data [107]. According to the Rishel model presented in Figure 5.1, the corrosion behavior in an erosive environment at high temperatures can be described in terms of the following four categories.

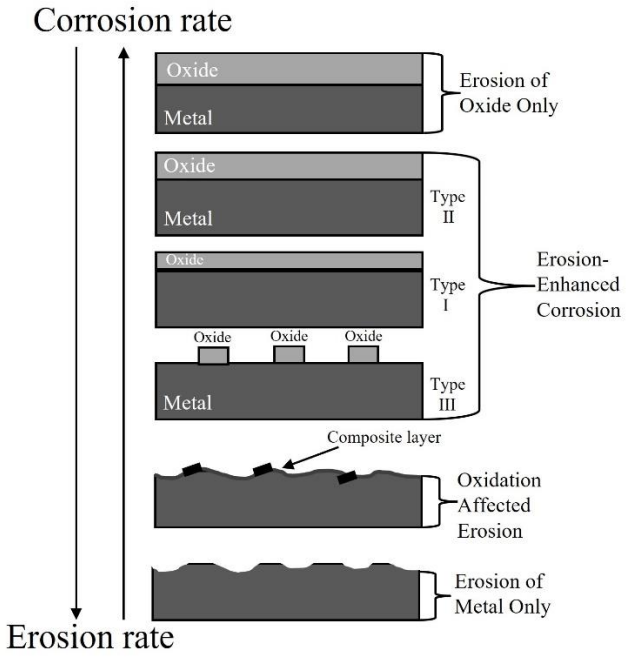

Figure 5.1: Erosion-Corrosion regimes, adapted from [108].

In *Erosion of oxide*, the effect of erosion is negligible and mainly confined to weak erosion of the oxide layer. Thus, the degradation rate is mainly corrosion-driven [108].

Erosion-enhanced corrosion is divided in two three subgroups (Types I, II and III). In Type I, the regime is characterized by oxide thinning due to erosion. As a result, the material wastage is larger than compared to pure oxidation. In Type II, the oxide is thicker than that seen in pure corrosion. This is attributed to the formation of cracks due to erosion in the oxide layer, which creates a short-circuit diffusion pathway for corrosive species. Lastly, in Type III, thermal and mechanical stresses provoke significant spallation of the oxide, exposing the material to the environment, which increases the corrosion rate [108].

In *Oxidation-affected erosion*, the oxide growth rate is significantly lower than the rate of erosion, resulting in direct contact between the metal surface and the corrosive environment. As such, a composite layer on top of the metal is formed, comprising oxidation fragments, deformed metal,

and erosion particles. Studies have shown that this composite layer can enhance the erosion rate of the material, leading to significant degradation of the material [108].

Compared to the studies on the degradation rates and mechanisms in superheaters positioned in the convective pass of waste-fired boilers, there are far fewer studies published regarding these activities in superheaters positioned in the loop seal region. Nevertheless, some studies have reported clear signs of corrosion attack on superheaters in this region, and these attacks are associated with aggressive corrosive species such as Cl, which suggests that the presumed mild environment might be harsher that initially believed [39] [40] [107]. One possible reason for this has been suggested by [39], whereby an increased corrosive environment is attributed to the transportation of corrosive flue gas to the loop seal region and metal surface via condensation on the fluidized bed material, leading to an more corrosive environment. Furthermore, the existing literature regarding the material wastage of FBHE positioned in the loop seal, is focused on commercial boilers firing pure biomass. Nafari et al [39, 109] have conducted two extensive studies on a wide range of coated and uncoated austenitic and ferritic steels, including stainless steels, FeCrAl alloys and Ni-based alloys, that were exposed in the loop seal of a 30-MW woodchip-fired CFB boiler. The exposure period was up to 2 years and the material temperature was in the range of 510°–550°C. The results showed that the oxide growth rate was non-linear on most of the sample, indicating that corrosion was the main degradation mechanism, while erosion was considered to have had a minor impact. In addition, a low rate of material degradation was observed, which was contributed to the seemingly mild corrosive environment. The deposits were mainly constituted of alkali components such as Ca, K, Mg and the corrosion product consisted of a multilayer oxide structure, indicating that breakaway corrosion had occurred. Traces of Cl were observed on the sample and the authors contributed the corrosion attack mainly to the active oxidation mechanism and presumable alkali chromate formations.

Chapter VI
Experimental

The experimental part is divided into two segments that outline the different experimental approaches used for **Papers I** and **II**.

6.1 Paper I – Material Selection for FBHE Application

6.1.1 Materials

In **Paper I**, a wide range of relevant alloys was exposed in the loop seal region of a commercial waste-fired CFB boiler for 6 and 12 months. The chemical compositions of the different alloys investigated in this study are presented in Table 6.1 (expressed in wt.%). The main goals of this work were to investigate the performances of novel FeCrAl alloys for FBHE applications and to benchmark their performances versus those of commercially available materials. The newly developed FeCrAl alloys tested in this study, Kanthal® EF100 and EF101, have lower Cr contents compared to other conventional FeCrAl alloys. While a lower Cr content reduces corrosion protection properties, this composition entails a significant improvement in mechanical properties at temperatures as low as 300°C by suppressing embrittlement of the alloy. In addition, EF101 is alloyed with additional silicon (Si), which have demonstrated to improve the protective properties beyond breakaway corrosion, as described in Chapter IV.

Table 6.1: Chemical compositions of the materials tested in Paper I.

		Chemical composition (wt.%)								
Name	Alloy type	Fe	Cr	Al	Ni	Mn	Si	Mo	Cu	Minor elements
316Ti	Austenitc stainless steel	Bal.	16.5	x	11	2	0.8	2.1	x	C, S, P, Ti
SX	Austenitc stainless steel	Bal.	17.5	x	19.5	0.5	5.0	0.4	2	C, S, P
Kanthal® EF100	FeCrAl	Bal.	10.1	4	x	<0.2	0.3	x	x	C, RE*
Kanthal® EF101	FeCrAl	Bal.	12.4	3.7	x	<0.1	1.3	x	x	C, RE*
Sanicro 69	Ni-based	10	30	x	60	<0.5	<0.5	x	x	C, S, P

* Reactive elements

x Excluded from the alloy

6.1.2 Exposure

For each alloy, two sets of half-moon sample rings were prepared and mounted on the top and bottom rows of the loop seal FBHE tube bundle. This was carried out during boiler shutdown using TIG-welding and Alloy 625 wire (see Figure 6.1). The samples were mounted at two positions on the superheater tubes:

- Windward position: facing downwards towards the loop seal air nozzles.
- Leeward position: facing upwards towards the return leg of the cyclone.

For this study, the samples positioned on the windward side were analyzed.

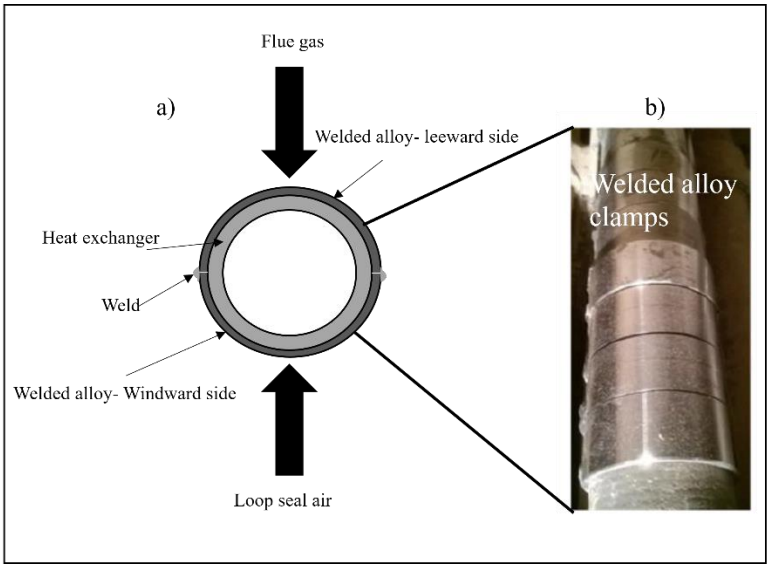

Figure 6.1: Schematic and photograph of: a) the welded areas of the loop seal FBHE; and b) samples clamped onto the FBHE bundle.

The field exposures were performed in an 85-MW_{th} waste-fired CFB boiler located in Sweden that was owned and operated by E.ON Energy Infrastructure AB. The fuel consisted of a mixture of industrial and household waste (see Figure 6.2). The circulating bed material consisted of roughly 70 wt.% fuel ash and 30 wt.% silica sand. The material surface temperatures facing the fireside were estimated using a boiler design software alongside the measured inlet and outlet steam temperatures. Based on the measured data, a material temperature of 500°–520°C was obtained.

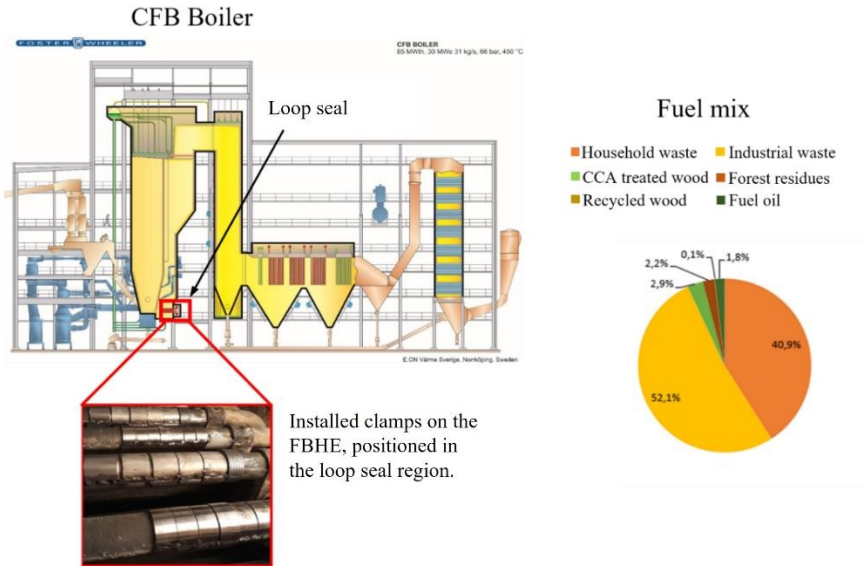

Figure 6.2: Schematic drawing of the CFB waste-fired boiler, positioning of the exposed samples and fuel mix.

The samples were removed using an angle grinder applied to the welded joint. The removed clamps were embedded in epoxy and cut using an automated saw to obtain a cross-sectional sample. The cross-sectional sample were ground down to 4000 grit, using silicon carbide (SiC) paper. To

enhance conductivity and the imaging contrast for the SEM analysis, a thin gold film of was deposited onto the samples through Au-sputtering.

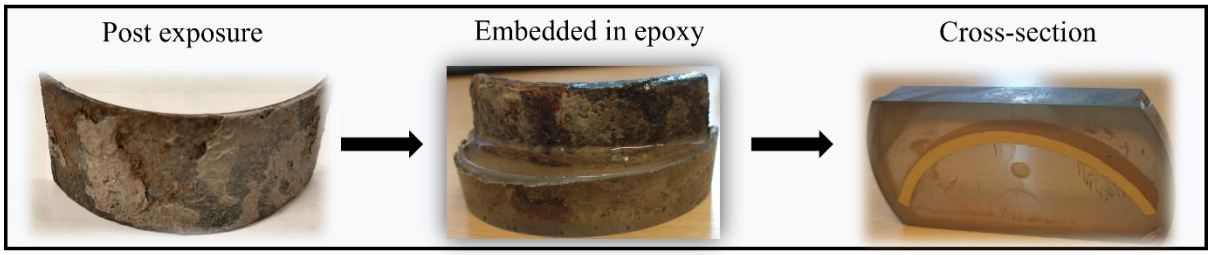

Figure 6.3: Preparation of cross-sections of the exposed samples.

6.2 Paper II – $PbCl_2$-induced Corrosion on Low-alloyed Steel

6.2.1 Material

In **Paper II**, a time-resolved study was carried out in a well-controlled laboratory environment. The aim was to investigate the corrosive effect of $PbCl_2$ on a low-alloyed steel (T22) and in particular to address the individual role of Pb and Cl. The chemical composition, expressed in wt.%, of the low-alloyed steel investigated in **Paper II** is shown in Table 6.2.

Table 6.2. Chemical composition of the investigated material, presented as wt.%.

Alloy	Fe	Cr	Si	Mo	Mn	C	P	S
T22	Bal.	1.9-2.6	≤0.50	0.87-1.13	0.3-0.6	0.05-0.15	≤0.025	≤0.025

6.2.2 Sample Preparation

Prior to exposure, the material was cut into coupons with nominal dimensions of 15 × 15 × 2 mm, and a hole was drilled at distances of approximately 7.5 mm and 2 mm from the edges. The surface edges were mechanically ground in water using silicon carbide (SIC) paper with a grit size of 1000. Subsequently, the samples were automatically ground in water using a Struers TegraPol-31 polishing instrument with a SIC paper grit size of 320 and polished with three diamond suspensions 9, 1 and 0.5µm until a mirror-like appearance was achieved. The samples were then degreased and cleaned by immersing them in acetone during ultrasonic agitation for 15 min using the Elmasonic P ultrasonic bath.

$PbCl_2$ was deposited on the polished sample surface by spraying a $PbCl_2$ deionized water solution onto the sample to achieve coverage of 0.185 mg/cm^2 in total (0.0925 mg/cm^2 on each side), while continuously heating the sample to ensure rapid evaporation of the solvent (Figure 6.4). To ensure that the correct amount of salt had been deposited on the sample surface, a Sartorius TM balance with microgram resolution was used to weigh the sample before and after salt deposition. As will be addressed in Section 8.2.2, $PbCl_2$ is rather reactive in this environment, and rapid formation of PbO was observed already after 24 h of exposure. To address the effect of PbO formation, additional samples were prepared that were covered with 0.185 mg/cm^2 PbO sample by spraying a PbO deionized water slurry onto the sample surface using same approach as for the $PbCl_2$-containing samples. All the samples were then stored in a desiccator that contained SICAPENT® as drying agent, before the furnace exposures.

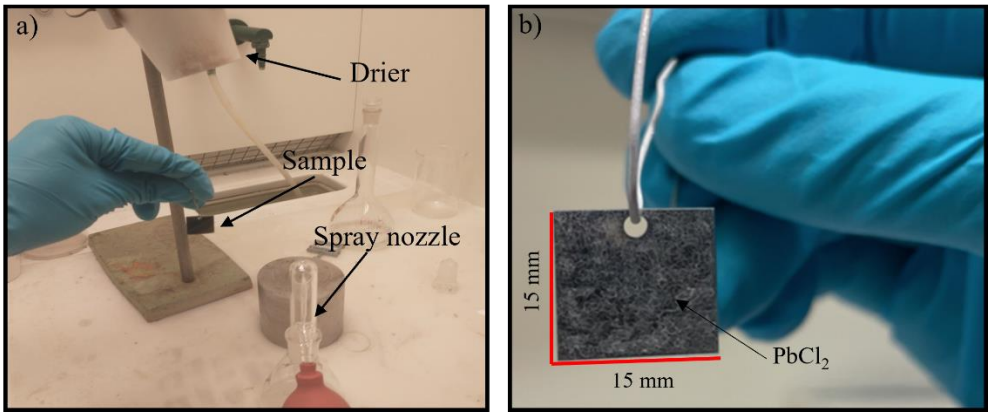

Figure 6.4: a) Photograph of the spray station. b) Polished sample surface covered with roughly 0.0925 mg/cm^2 $PbCl_2$.

6.2.3 Furnace Exposure

A schematic of the furnace setup used in **Paper II** is shown in Figure 6.5. The exposures were carried out isothermally at 400°±2°C using an 80-mm-diameter silica tube. The samples were exposed to a continuous gas flow that contained 5%O_2 + 20% H_2O + N_2 bal. at a flow rate of 3 cm/s for 1 h, 24 h and 168 h. Three samples were placed in alumina sample holders parallel to the gas flow for each exposure. The gas flow was measured with the Definer 2020 flowmeter, and the vapor content of the gas was obtained by connecting a water bath, set to 60°C, to the system, whereby the water vapor was added to the gas via a Nafion membrane. The water vapor content was measured at the exit of the membrane just before the entrance to the horizontal tube furnace using the Mitchell Instruments Optidew Vision™ chilled mirror humidity sensor. Following the exposure, the samples were stored in a desiccator containing SICAPENT® (P_4O_{10}) as drying agent.

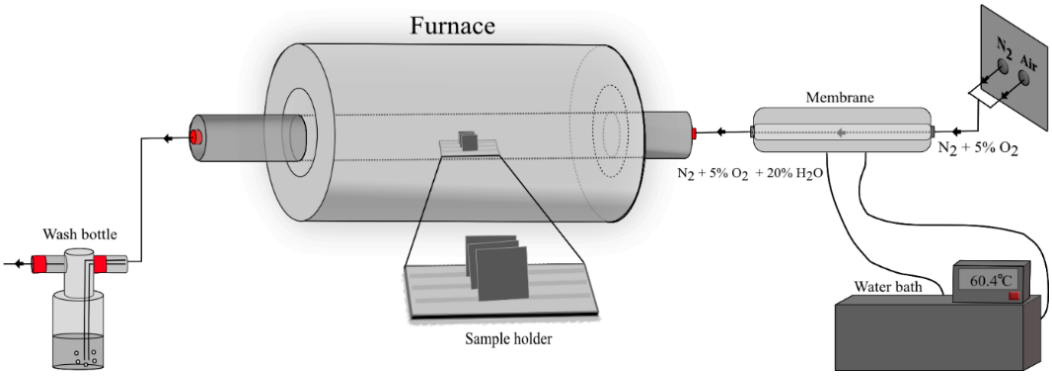

Figure 6.5: Schematic of the furnace setup used in paper II.

6.2.4 Sample Preparation for Cross-Sectional Analysis

Broad ion beam (BIB) milling was carried out in **Paper II** to produce high-quality cross-sections of the exposed samples. In this study, the Leica TIX 3X instrument equipped with three argon guns was used. The samples were subjected to BIB for 6 h at 8 kV and 3 mA. The working principle of BIB milling is shown in Figure 6.6. The sample of interest was mounted inside a vacuum chamber and subjected to an Ar^+ ion beam generated by a fixed Ar ion gun. In between the Ar-guns and the sample, a mask was applied to focus the generated beam onto a fixed surface area of the sample of interest. The kinetic energy of the Ar^+ allows the removal of thin layers of the material in a layer-by-layer fashion and removes potential artifacts derived from the mechanical polishing. Figure 6.6

compares two different regions of a sample that was prepared by mechanical polishing and BIB milling. It is apparent that the BIB milling-generated ion-etched surface allows far-superior resolution of the cross-section, allowing small features of the corrosion products to be observed. Prior to the milling process, a thin silica wafer was glued on top of the exposed samples and allowed to dry overnight. The sample was then cut in half and polished to a 0.5-µm surface finish with the Lecia EM TXP instrument, which was operated at low-speed setting and without any lubricant.

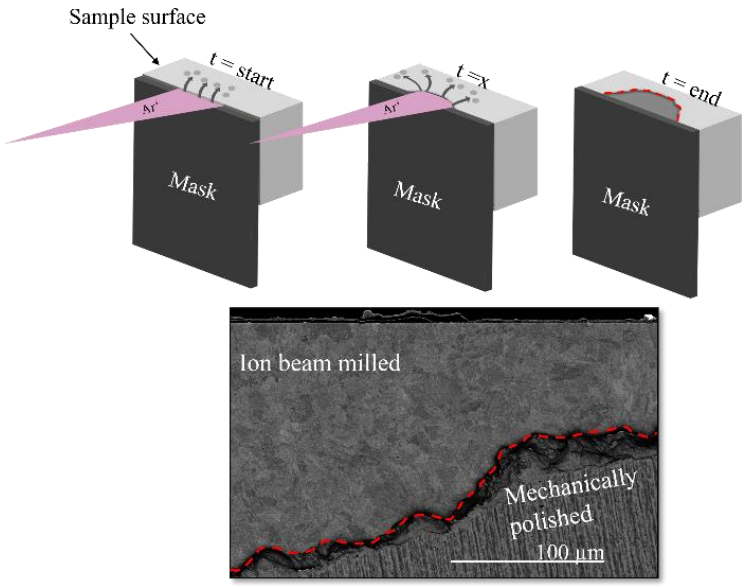

Figure 6.6: Schematic representing the working principle of BIB. The cross-section image shows the difference in resolution between samples prepared with BIB versus mechanical polishing.

Chapter VII
Characterization Methods

In order to understand and evaluate fully the complex corrosive events presented in this work, different analytical techniques and tools have been implemented. A brief explanation of the various instruments used in this study is provided below.

7.1 Scanning Electron Microscopy (Papers I & II)

Most of the findings presented in this work have been obtained through the use of scanning electron microscopy (SEM). SEM is an extensively employed instrument for the examination and analysis of the microstructural features of solid objects at sub-micron scales. In this work, all the plan-view and cross-sectional images of the samples of interest were acquired using SEM with an accelerating voltage of 10–20 keV, and the EDX analysis was carried out at 20 keV. The analyses were performed in the FEI QUANTA 200 FEG ESEM instrument coupled with an Oxford Instruments X-MAX 80 (EDX) detector.

The SEM instrument utilizes electrons to produce high-magnification images, in contrast to the light used in optical microscopes. The electrons in the SEM instrument are generated by an electron gun. The produced electrons are generally accelerated to a high energy level, in the range of 0.1–35.0 keV, and travel to the electron column where a system of electromagnetic condenser lenses and apertures is situated, the purpose of which is to align the electron beam into a narrow probe size while filtering away high-angle electrons that might decrease the quality of the image. The electron beam then passes through a set of scanning coils and an objective lens, which allows the formation of a highly concentrated probe beam that is rasterized over the studied specimen [110].

Chemical and surface information on the examined objects in SEM relies on the interactions between electrons emitted from the SEM instrument (primary electron beam) and the atoms of the specimen under study. The signals detected from the beam-specimen interaction include secondary electrons (SE), backscattered electrons (BSE), and characteristic x-rays (EDX), among others. In this study, the SE, BSE and EDX signals have been studied, as they offer valuable insights into the sample's topography, crystallography, and chemical composition. The depth of interaction of the specimen depends heavily on the type of signal generated, the studied material, the accelerating voltage, and the incident angle of the generated electron beam (see Figure 7.1) [110].

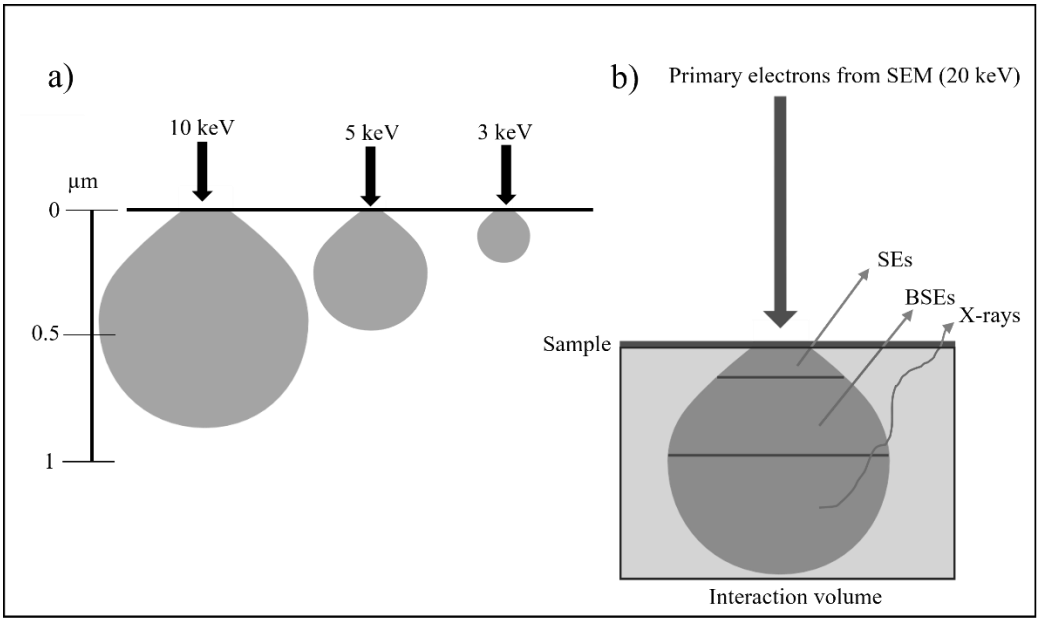

Figure 7.1: a) Depiction of the relationship between the interaction volume and accelerating voltage from the primary electron beam [111]. b) Relative interaction volumes of the emitted signals studied in this thesis.

7.1.1 Secondary Electrons (SE)

SE are low-intensity electrons (<50 eV) that are generated from inelastic interactions between the studied sample and the primary electron beam. Their relatively low energy limits the escape depth of the electrons. Consequently, the majority of the SE that escape to the surface of the material and reach the originate from areas close to the specimen surface, which means that they can carry useful information regarding the topography and complex surface features of the sample studied, with a spatial resolution of a few nanometers (see Figure 7.2) [110].

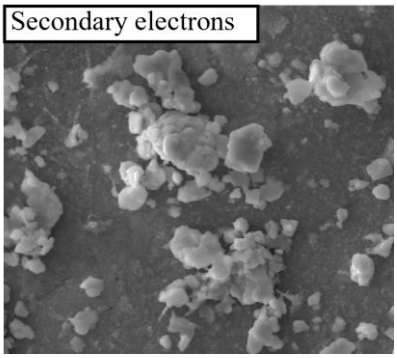

Figure 7.2: Secondary electron image. The contrast observed in the image is due to geometrical features where the edges of the surfaces emit more secondary electrons than the flat regions resulting in brighter regions.

7.1.2 Backscattered Electrons (BSE)

BSE are generated by elastic scattering between an electron and an atomic nucleus. This event changes the electrons trajectory, and the electron only loses minimal kinetic energy. This allows the electrons to obtain a much higher escape volume than is seen for the SE. However, this also leads to reduced spatial resolution of the image, as compared to SE. After numerous elastic interactions with the sample, the BSE may eventually reach the surface of the material and escape to the detector. The probability that elastic collisions will occur is proportional to the atomic number, *Z*, and the density of the material. Thus, heavy elements or dense regions of the sample will produce a high number of BSE that reach the detector, resulting in a bright appearance in BSE

images. Conversely, low-density areas or light elements will manifest as darker regions (see Figure 7.3) [110]. In this work, BSE have been utilized readily to determine the interface between oxides with different chemical compositions.

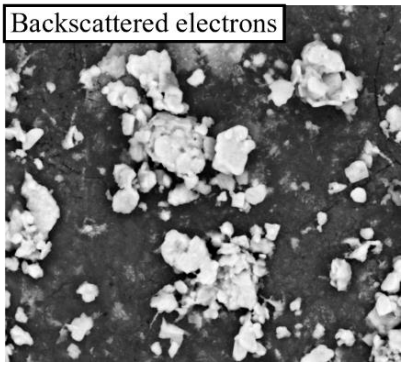

Figure 7.3: Backscattered electron image. The contrast observed in the image is due to the different chemical compositions of the different areas. The bright regions represent Pb-rich areas while the dark regions represent Fe-rich areas.

7.1.3 X-ray Photons

If sufficient energy is transferred between the primary electron beam and the sample atom, ejection of electrons from the inner electron shell of the atom may occur, leaving the atom in an excited state. As a direct consequence, the atom relaxes to its ground state by allowing electrons at higher energy levels to fill the vacant position. During this event, the excess energy is emitted as x-ray photons with a defined energy that is characteristic for each element. By coupling an EDX detector to the SEM instrument, it is possible to identify the chemical composition and quantify the chemical elements of individual points or map out the distribution of elements in the studied area. Compared to SE and BSE, the escape volume is significantly larger for x-rays, which limits the possibility to quantify precisely the chemical elements in small volumes of interest [110].

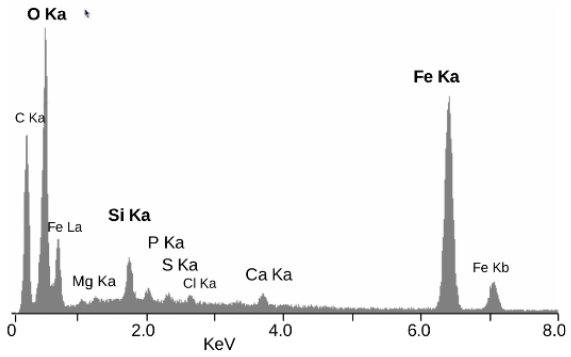

Figure 7.4: EDX spectrum.

7.2 X-Ray Diffraction (Paper II)

Crystallographic information on the corrosion product in **Paper II** was acquired with x-ray diffraction (XRD). In XRD, an x-ray source, which in this study comprised a copper anode x-ray tube, emits a monochromatic x-ray beam (CuK_{α}) that is filtered to a discrete wavelength. The emitted x-ray is applied to the sample of interest [112]. Upon interaction with the sample's atomic lattice structure, constructive interference may take place if the conditions satisfy Bragg's law:

$$n\lambda = 2d_{hkl}\sin\theta \quad (7.1)$$

Were *n* being an integer number, λ is the wavelength of the x-ray, d_{hkl} is the interplanar spacing of the lattice planes, and Θ is the angle at which radiation diffracts from the crystal plane. The interaction of the x-ray and substrate results in the formation of a diffractogram, which can be compared with an existing database to identify the crystalline phases [112].

Several different modes of XRD may be used. In this work, Bragg-Brentano x-ray diffraction was utilized. In this setup, the source and detector move in opposite directions symmetrically and at the same rate, as depicted in Figure 7.5. As the angle of the detector and source increases relative to the sample, the x-ray penetration depth increases, thereby allowing the identification of crystalline phases throughout a relatively thick oxide. In this work, the Siemens Bruker 8 Discovery diffractometer equipped with a Cu source and with a measuring range of 10< 2Θ <90° was employed to analyze the oxide scales.

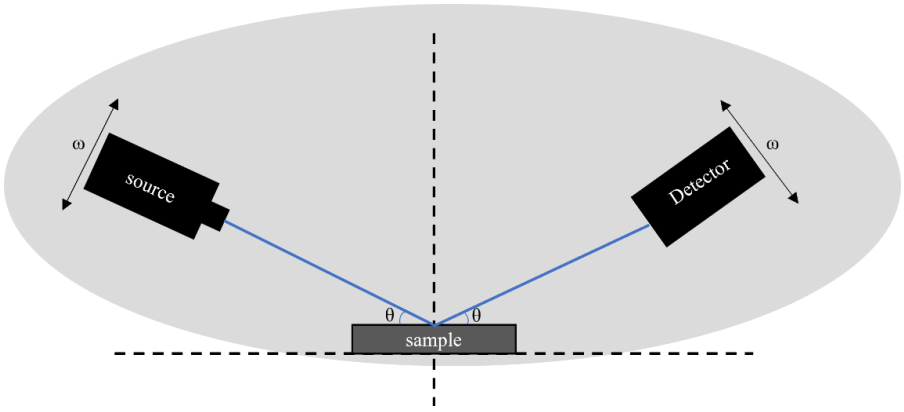

Figure 7.5: XRD with Bragg-Brentano x-ray diffraction.

7.3 Material Loss Analysis (Paper I)

In **Paper I**, material losses were quantified by measuring the sample thickness before and after exposure, by combining ultrasonic measurements with SEM. Prior to exposure, the thickness of the clamps was measured three times around the sample using an Olympus 27MG ultrasonic thickness gage (UTG) with 0.01-mm resolution. After exposure, a cross-sectional surface was prepared as described in Section 6.1.2. The material loss was measured by combining SEM with a vector graphic software (INKSCAPE). Initially, an SEM BSE image was acquired and subjected to INKSCAPE, and three vertical lines were drawn between the metal surface and oxide where the measured pixels of each line were converted to micrometers. Thereafter, the cross-section was tilted at a 45° angle and the sample thickness was measured once again at three positions (see Figure 7.6). This step was repeated for a total of three times, and a total of nine data-points was analyzed; the average material loss and standard deviation were recorded. In this work, intergranular corrosion attack and internal nitridation were not included in the material loss quantification.

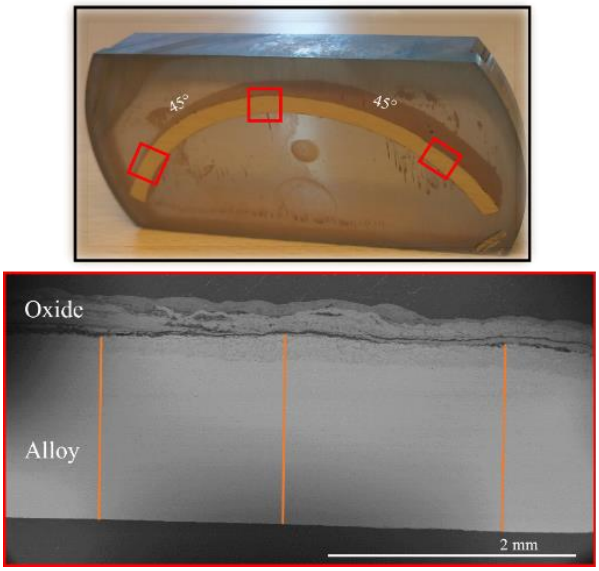

Figure 7.6: Material loss analysis conducted by combining SEM with the vector graphic software INKSCAPE.

7.4 Oxide Thickness Analysis (Paper II)

The oxide thickness measurements in **Paper II** were carried out by combining SEM with INKSCAPE. In total, four SEM BSE images were obtained within the BIB cross-sectional area and combined in a panoramic fashion. Subsequently, the images were subjected to analysis with the INKSCKAPE software, and the oxide thickness was measured by drawing vertical lines over the oxide where each pixel was converted to micrometers. In total, nine measuring points were used, and the average oxide thickness and standard deviation were recorded.

Chapter VIII
Results and Discussion

As highlighted throughout this work, replacing fossil fuels with waste as an energy source for more-sustainable heat and electricity production has become a high priority in national and global energy and waste management policies. However, one of the major drawbacks associated with this shift is the increased rate at which heat exchange materials corrode in waste-fired boilers. In this context, this thesis has focused on studying the critical corrosion phenomena in waste-fired boilers and providing new insights into these events.

The first part of this chapter provides an overview and discussion of the outcomes from the long-term-exposure material degradation test carried out on various alloy types that were evaluated for their suitability for FBHE applications in the loop seal regions of commercial, waste-fired CFB boilers. Specifically, the aim of this study was to improve the understanding of the interplay between erosion and corrosion and how this affects material degradation in this environment. The motivation for this study was the limited existing literature covering this specific topic, and to simplify the process of selecting materials for this particular application.

The second part of this chapter concerns the results from the laboratory study regarding the influence of $PbCl_2$ on high-temperature corrosion of low-alloyed steel that is exposed to a humid environment at 400°C. While the existing literature has addressed $PbCl_2$-induced corrosion in similar environments and materials, there remains a gap in the knowledge regarding the initial and propagating corrosion mechanisms. Given that the initial corrosion process may strongly impact the corrosion behavior in subsequent stages, acquiring detailed knowledge of the initial corrosion mechanisms is of great importance. Moreover, previous studies have mainly attributed propagating corrosion mechanisms to Cl-induced corrosion and the formation of metal chlorides, either through melt formation or the rapid release of Cl that results from $PbCl_2$ decomposition, with little discussion on the role of Pb in the corrosion process. Elucidating this phenomenon is crucial for the development of corrosion prevention strategies and for gaining insights into the rapid degradation rates observed in the water-wall tubes of waste-fired boilers. Consequently, the results presented in this study offer valuable insights into the corrosion mechanisms induced by $PbCl_2$ on low-alloyed steel, potentially enhancing our understanding of high-temperature corrosion phenomena within the water-wall regions of waste-fired boilers.

8.1 Paper I - Material selection for FBHE applications

8.1.1 Material Loss Analysis

Figure 8.1 shows the material losses for the samples after 6 and 12 months of exposure. As described in Section 7.3, nitridation and intergranular oxidation was not included in the material loss calculation. Due to exposure failure, the Sanicro 69 and EF101 materials exposed for 12 months could not be retrieved.

Severe material loss (0.68 µm) was observed for the austenitic stainless steel 316Ti after 6 months of exposure, whereas the remaining materials showed material losses of <0.20 µm after the same exposure time. The small differences observed between the high-performing materials (SX, EF100, EF101 and Sanicro 69) could be attributed to their different positions on the superheater bundle,

which may lead to minor changes in the exposure conditions. After 12 months of exposure, the material loss was roughly 6–7-fold higher for the 316Ti sample than for the novel EF100 FeCrAl alloy and the austenitic steel SX. These results indicate that conventional austenitic stainless steels may not be suitable for FBHE applications in the loop seal region.
The novel FeCrAl alloy EF100 and EF101 manifested minimal material losses (roughly 0.10 mm) within the 6-month exposure period. Moreover, EF100 exhibited significantly low material losses even after 12 months of exposure and demonstrated the lowest material loss (0.19 mm) of the materials tested.

Lastly, the austenitic stainless steel, SX displayed negligible material loss, outperforming the Ni-based alloy Sanicro 69 and alumina-forming FeCrAl alloys after 6 months of exposure. After 12 months of exposure, the SX sample exhibited a slightly higher material loss than EF100 (0.22 mm versus 0.19 mm).

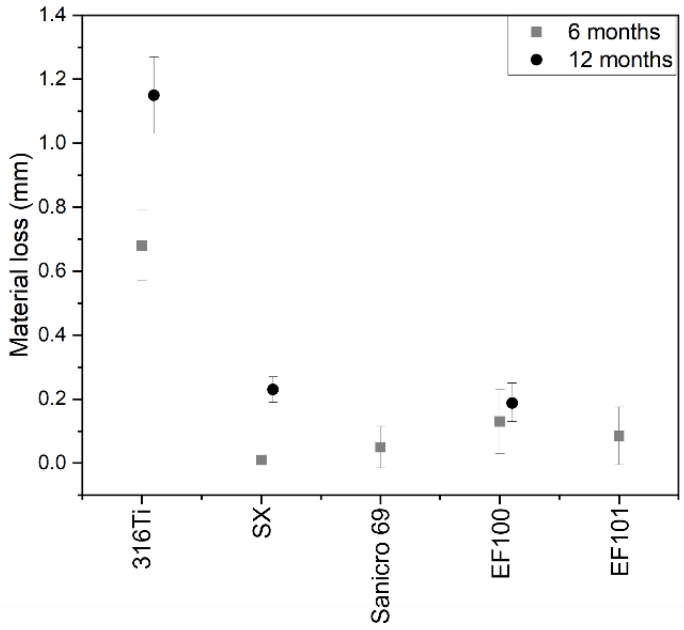

Figure 8.1: Material losses after 6 and 12 months of exposure.

8.1.2 Microstructural Analysis

A cross-sectional analysis was carried out to identify the corrosion products of the exposed alloys. These analyses were carried out to improve understanding of the interplay between erosion and corrosion attacks in this environment. A summary of the observed corrosion products and material losses is shown in Table 8.1.

Table 8.1: Summary of the microstructural analysis carried out in Paper 1.

Name	Alloy type	Exposure time (months)	avrg Material loss (µm)	avrg Internal oxidation (µm) *	avrg Internal AlN (µm) *	Deposit composition
316Ti	Austenitic stainless steel	6	0.68 ± 0.11	126 ± 25	x	x***
SX	Austenitic stainless steel	6	0.01 ± 0	72 ± 10	x	Ca, S, Cl, Na
Sanicro 69	Ni-based	6	0.05 ± 0.01	230 ± 42	x	Ca, S, P, Mg
EF100	FeCrAl	6	0.13 ± 0.1	x	96 ± 90	Mg, Ca, S, P, Si
EF101	FeCrAl	6	0.09 ± 0.1	x	424 ± 220	Ca
316Ti	Austenitic stainless steel	12	1.15 ± 0.12	225 ± 19	x	x***
SX	Austenitic stainless steel	12	0.23 ± 0.04	192 ± 35	x	Ca, S, Cl, Na
Sanicro 69	Ni-based	12	N.a**	N.a**	x	N.a**
EF100	FeCrAl	12	0.19 ± 0.06	x	430 ± 70	Ca, S, Mg
EF101	FeCrAl	12	N.a**	x	N.a**	N.a**

* Not included in material loss measurement
** Experimental failure
*** Not obserseved during SEM analysis

- 316Ti

After 6 and 12 months of exposure, an outer oxide layer, primarily composed of Cr with a lesser concentration of Fe, was detected on the surface of the 316Ti sample (see Figure 8.2). This is assumed to be remnants of an inward growing mixed spinel oxide containing both Fe and Cr and should not be confused with a Cr_2O_3 primary protective oxide. Seeing the significant corrosion attacks and high material loss for these samples, it is assumed that the sample has undergone breakaway corrosion. Furthermore, barely any deposit was found the samples. Clear signs of internal oxidation propagating in the grain boundaries appeared after 6 months, and these zones continued to propagate over time. From the EDX analysis of the samples after 12 months of exposure, it was clear that a Cr-rich oxide had formed in the steel grain boundaries (see Figure 8.2 d). Furthermore, after 12 months of exposure, a roughly 150-µm-thick, Cr-depleted region had formed below the alloy/oxide layer. The Cr-depletion zone was also observed after 6 months but it was less-significant in magnitude.

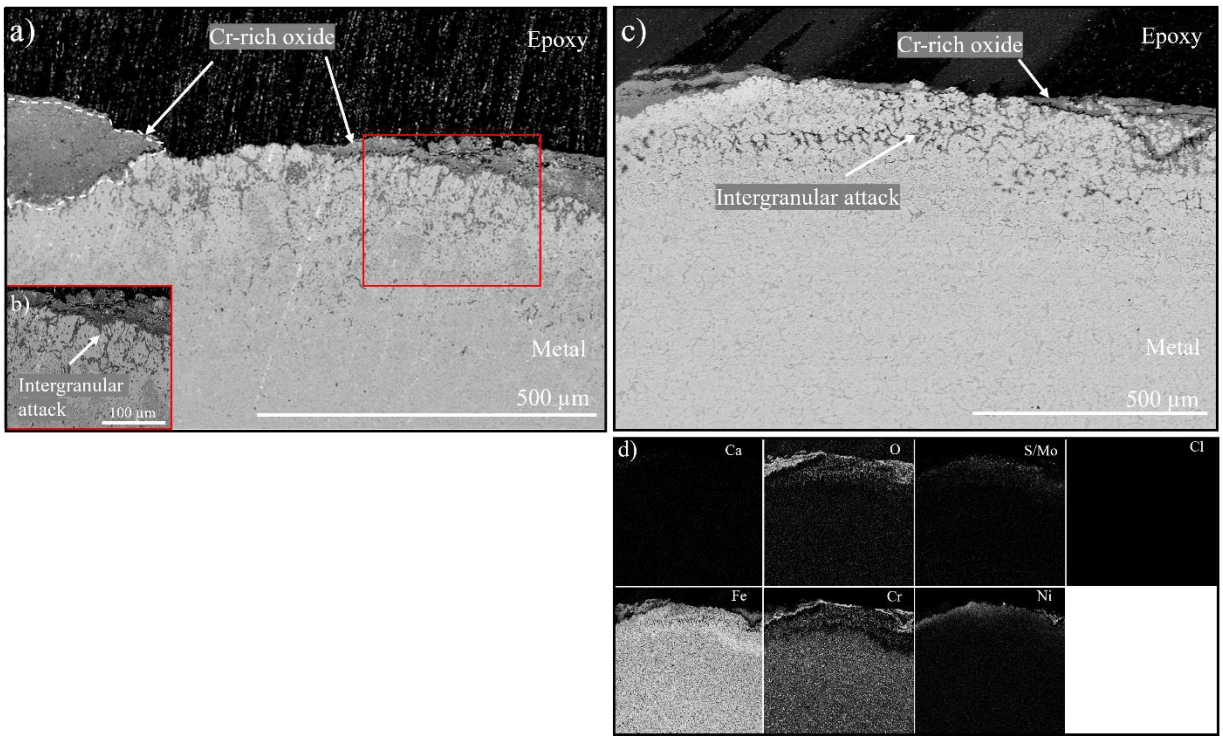

Figure 8.2: SEM BSE cross-sectional images of 316Ti: (a) after 6 months of exposure; (b) showing intergranular corrosion attack after 6 months of exposure; and (d) EDX mapping of (c).

The grain boundary attacks and the Cr-depletion zones observed on the 316Ti samples have been reported previously for austenitic stainless steel exposed to corrosive environments at high temperatures [113, 114]. The Cr-depletion zones are suggested to be a consequence of severe corrosion attack on the material, causing Cr from the bulk material to diffuse to the corrosion front to replenish the content of Cr in the oxide, while simultaneously leaving behind a zone that contains less Cr due to the slow diffusion of Cr in the bulk material. Although the Cr-depleted zone is not accounted for in the material loss, it significantly alters the material composition close to the corrosion front, and it may affect its mechanical properties.

The significant corrosion features observed throughout the cross-section indicate that corrosion has played an important role in the degradation rate of this material. Considering the substantial depth of the Cr-depleted zones together with the grain boundary attacks on the samples, it can be argued

that the erosive components of the degradation mechanisms were not the rate-determining steps in the observed material loss. If the degradation mechanism would be erosion-driven, the intergranular corrosion features observed would most likely have been eroded from the sample, as discussed in the Rishel model (see Section 5.5). Given the high material losses, it is presumed that the material had undergone breakaway corrosion and that the outward-growing Fe-rich oxide had spalled off during sample preparation rather than being eroded away during the exposure.

- SX

The cross-sectional and EDX analyses of alloy SX after 6 and 12 months of exposure revealed the formation of a continuous deposit that contained high levels of Ca and S, as well as traces of Na and Cl (Figure 8.3). The material had undergone breakaway corrosion after 6 months of exposure, revealing a multilayered oxide that contained an outward-growing, Fe-rich oxide. The internal oxidation at the metal/oxide interphase consisted mainly of a Cr- and Si-rich oxide that was propagating via the grain boundaries. At approximately 60 µm below the metal/oxide interphase, there was notable depletion of Cr within the grain boundaries, while simultaneously there was enrichment of the Si-rich oxide, after 12 months of exposure.

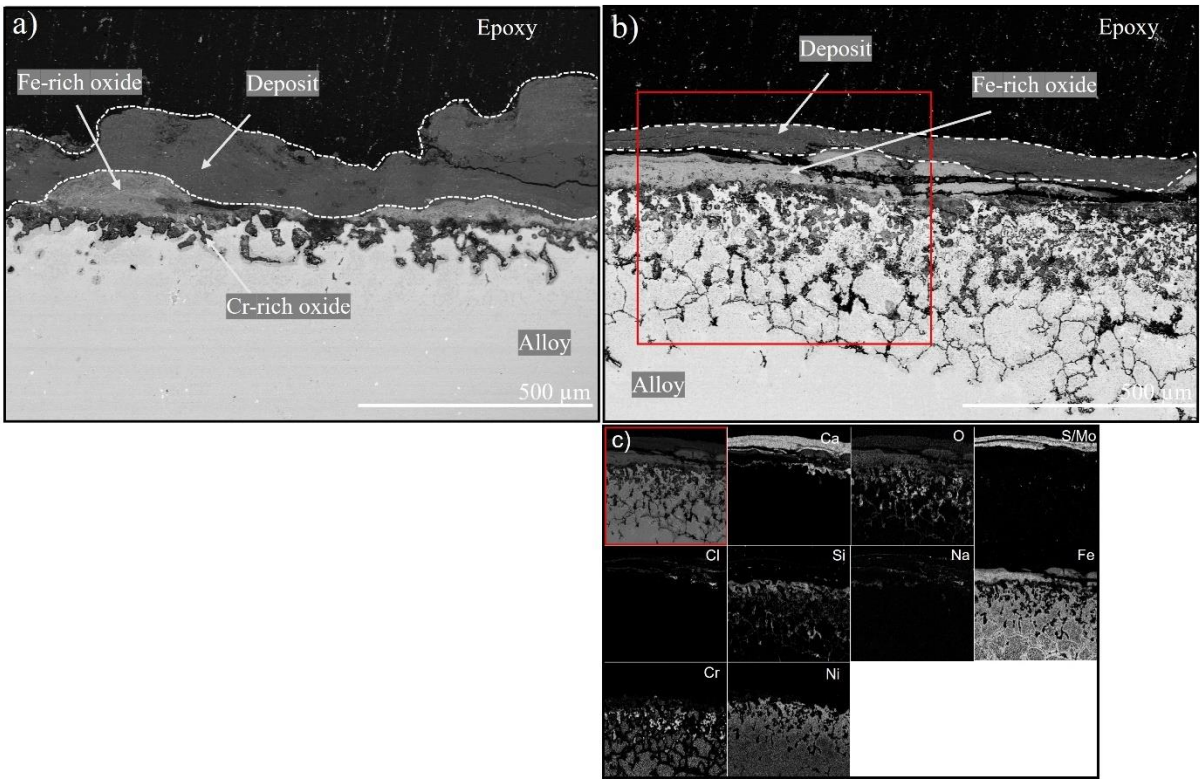

Figure 8.3: SEM BSE cross-sectional images of SX after: (a) 6 months of exposure; (b) 12 months of exposure, (c) EDX mapping of highlighted area in (b).

As with 316Ti the microstructural feature for this material indicates that a corrosion attack has taken place on this material considering the presence of Cr-depletion zone and grain boundary attacks. It could be argued that the visible Si originates from the fluidized bed material, which contains of quartz (SiO_2), or from the polishing paper during sample preparation. However, the incorporation of Si into the oxide layers was detected only for the SX material, confirming that the Si originates from the alloy. Supportive results from [115] and [116] demonstrate the mitigation of the corrosion rate upon the addition of Si to austenitic stainless steel. In a previous study (107), an

austenitic stainless steel (353MA, containing 2.42 wt% Si) was exposed to 700°C and 900°C in a humid environment. A continuous SiO_2 layer that propagated into the steel grain boundaries was observed after 168 h at the metal/oxide interphase, and it was suggested that the silica acts as a diffusion barrier, thereby improving the corrosion-protective properties of the material. Similar oxide features were observed in the present study, and it is tempting to conclude that the formation of a silica is the main reason for the observed reduced corrosion rate of SX, as compared to 316Ti.

However, compared to 316Ti, SX also contains a high concentration of Ni. Research has indicated that an elevated Ni content in austenitic alloys can enhance the protective properties of the resulting oxide scale, beyond breakaway corrosion [85]. Studies have shown that increase Ni content in austenitic alloys may promote the protective properties of the formed oxide scale, beyond breakaway corrosion. As such, since both the Si and Ni contents may play important roles in the kinetics of oxidation of austenitic stainless steels in this environment, it becomes challenging to define definitively the impact of each individual element on the corrosion properties with the current experimental setup. Nevertheless, when comparing the material losses of the conventional austenitic steel 316 Ti and SX it becomes apparent that SX manifests superior corrosion resistance in this environment.

- Sanicro 69

Figure 8.4 shows the cross-sectional SEM image of the Sanicro 69 sample after 6 months of exposure. A deposit layer with thickness of about 50 µm was observed that contained mainly S, Ca, and O, with traces of P and Mg. Underneath the deposited layer, a Ni-rich oxide had formed, and at the metal/oxide interface, an oxide with a significant amount of Cr was detected. In addition, a Cr-rich oxide was observed further into the metal, at a depth of approximately 80 µm below the corrosion product layer, most likely representing a 3D effect in this 2D cross-sectional imaging. EDX mapping revealed that Cr depletion occurred in the metal, while Ni remained the principal alloy element close to the corrosion front. As shown in Figure 8.1, the measured material loss for Sanicro 69 was negligible after 6 months of exposure. Nevertheless, considering the microstructural analysis, the internal corrosion attack could be observed up to a depth of 0.3 mm into the metal and should be considered.

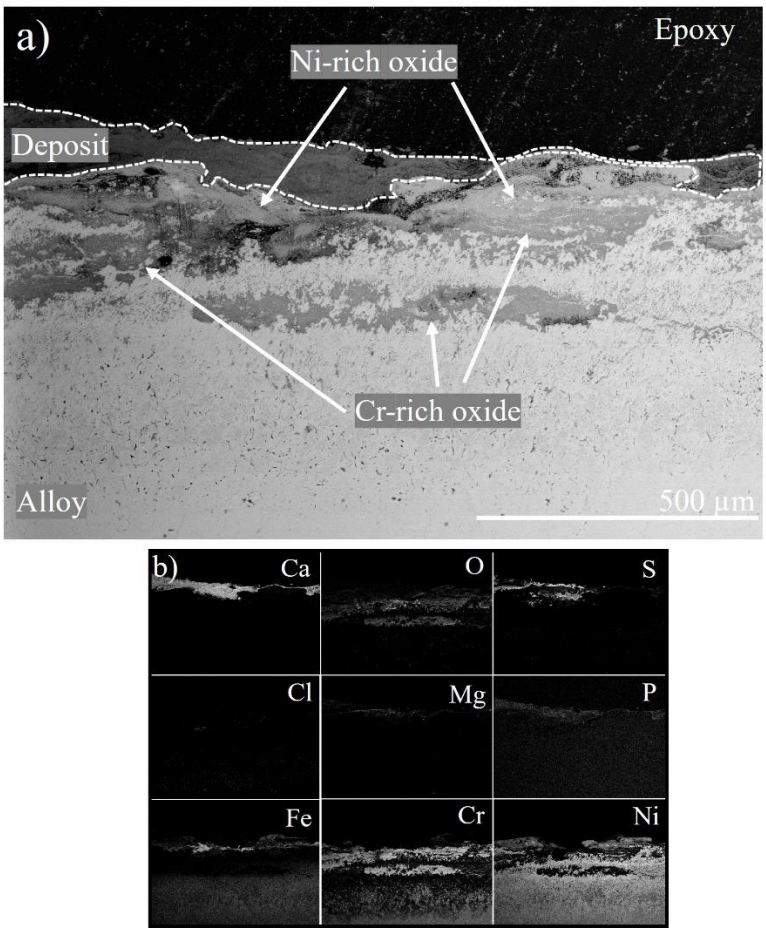

Figure 8.4: SEM BSE cross-sectional images of Sanicro 69 after: (a) 6 months of exposure; (b) EDX mapping of (a).

Sanicro 69 contains significant amounts of Ni. As mentioned earlier, various studies have demonstrated a positive relationship between increased Ni content and enhanced corrosion resistance at high temperatures when in contact with alkali chlorides [85]. A previous study of the degradation rate of Ni-based alloys in the loop seal region of a biomass boiler revealed minimal material degradation after 12 months of exposure. In that study, forest residue was fired, which is usually less corrosive than waste used as fuel. As such, if one were to extrapolate the results from the present study, the outcome would suggest that Sanicro 69 exhibits good protective properties in the prevailing environment even after 1 year of exposure.

- EF100 & EF101

The cross-sectional analysis of EF100 after 6 months of exposure revealed that a multi-layer oxide had been formed that contained an outward-growing, Fe-rich oxide and a Cr/Al-rich oxide, close to the metal/oxide interphase (Figure 8.5). Crack and void formations were observed on the oxide scale throughout the cross-section. From the EDX analysis, it is clear that a deposit containing Ca, S Mg, and P was formed on top of the oxide. Moreover, the SEM EDX analysis revealed severe internal nitridation. The internal nitridation zones consisted of alumina nitride (AlN) precipitates that were embedded in a Fe-rich alloy matrix. The nitridation zone was identified throughout the cross-section in a patch-wise pattern, with zone thicknesses in the range of 10–250 µm.

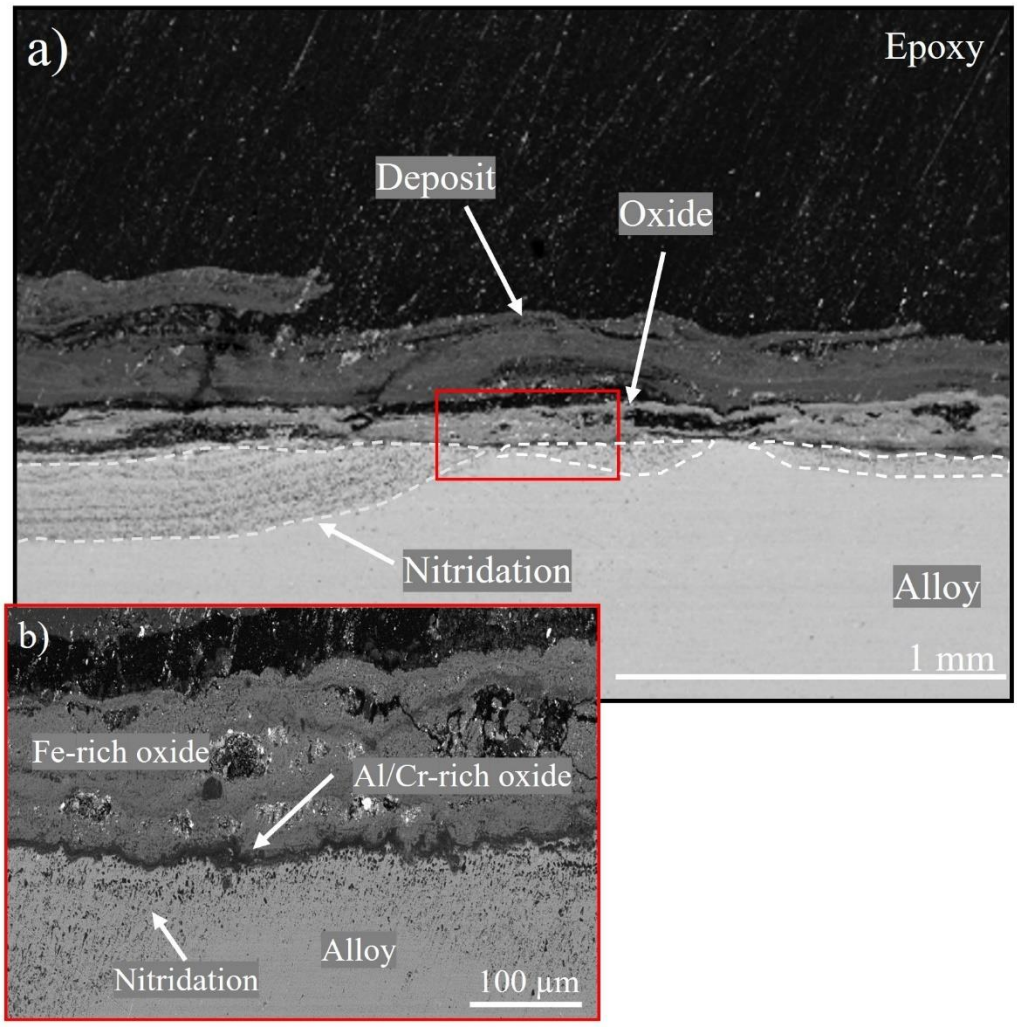

Figure 8.5: SEM BSE cross-sectional images of EF100 after: (a) 6 months of exposure; (b) Higher-magnification image of the area highlighted in (a).

Similar features were observed for EF100 exposed for 12 months (Figure 8.6). However, increased thickness of the Fe-rich oxide was observed together with increased severity of Al-nitridation, and these were distributed in a homogenous fashion throughout the cross-section and below the metal/oxide interface (*cf.* Figures 8.5 and 8.6). Beneath the nitridation zone, a roughly 100-µm-thick, Cr-depleted zone was noted.

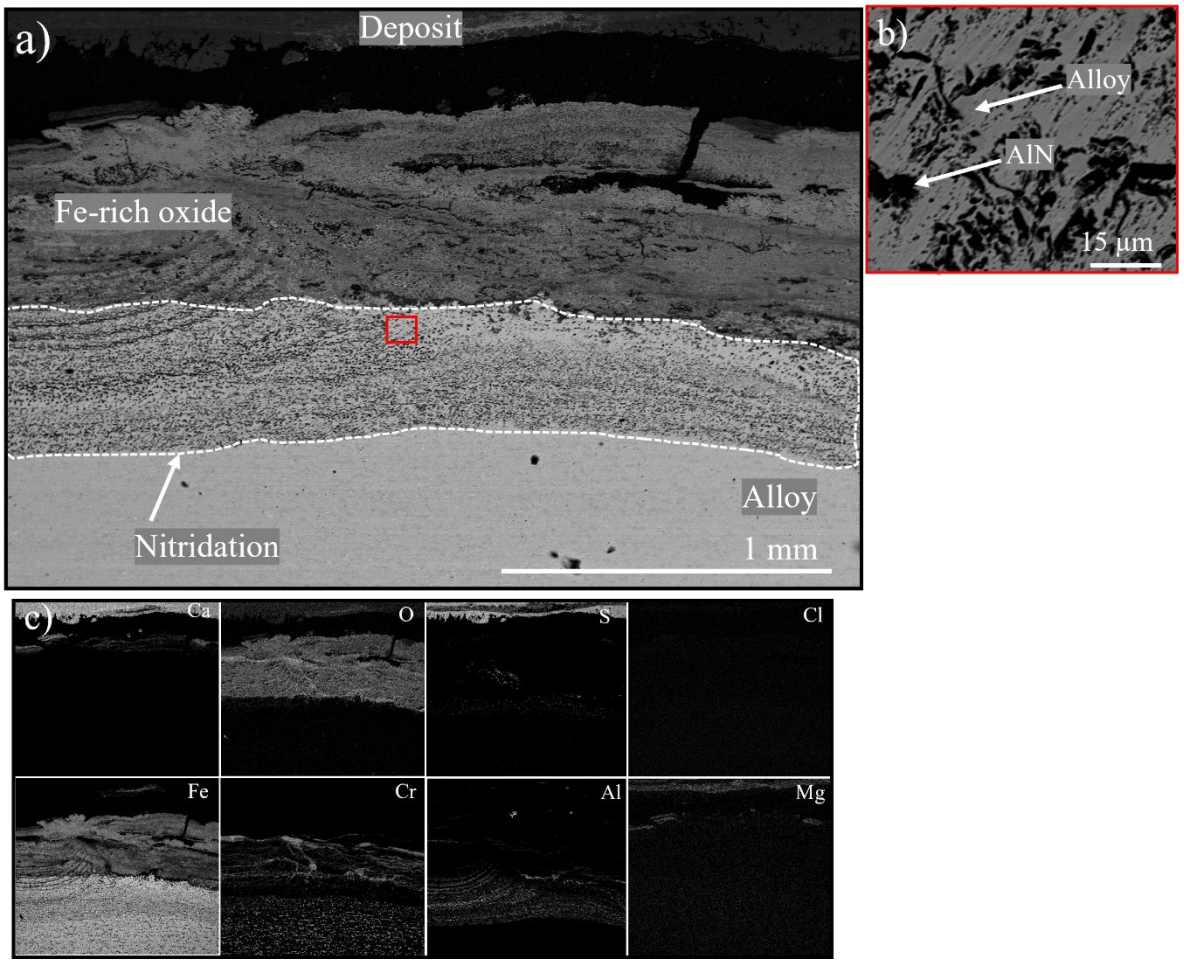

Figure 8.6: SEM BSE cross-sectional images of EF100 after: (a) 12 months of exposure; (b) Higher-magnification image of the area highlighted in (a); (c) EDX mapping of (a).

The cross-sectional images of EF101 that was exposed for 6 months are shown in Figure 8.7. After 6 months of exposure, EF101 displayed characteristics similar to EF100 exposed for the same amount of time. The sample exhibited breakaway corrosion, with a layer of Fe-rich oxide located beneath a deposit layer that was rich in Ca. In close proximity to the metal/oxide interface, weak traces of Al-rich oxide were identified, although they did not appear to be uniformly distributed across the surface. A notably large AlN region was observed below the oxide, which in some regions exceeded 700 µm in thickness (see Figure 8.7).

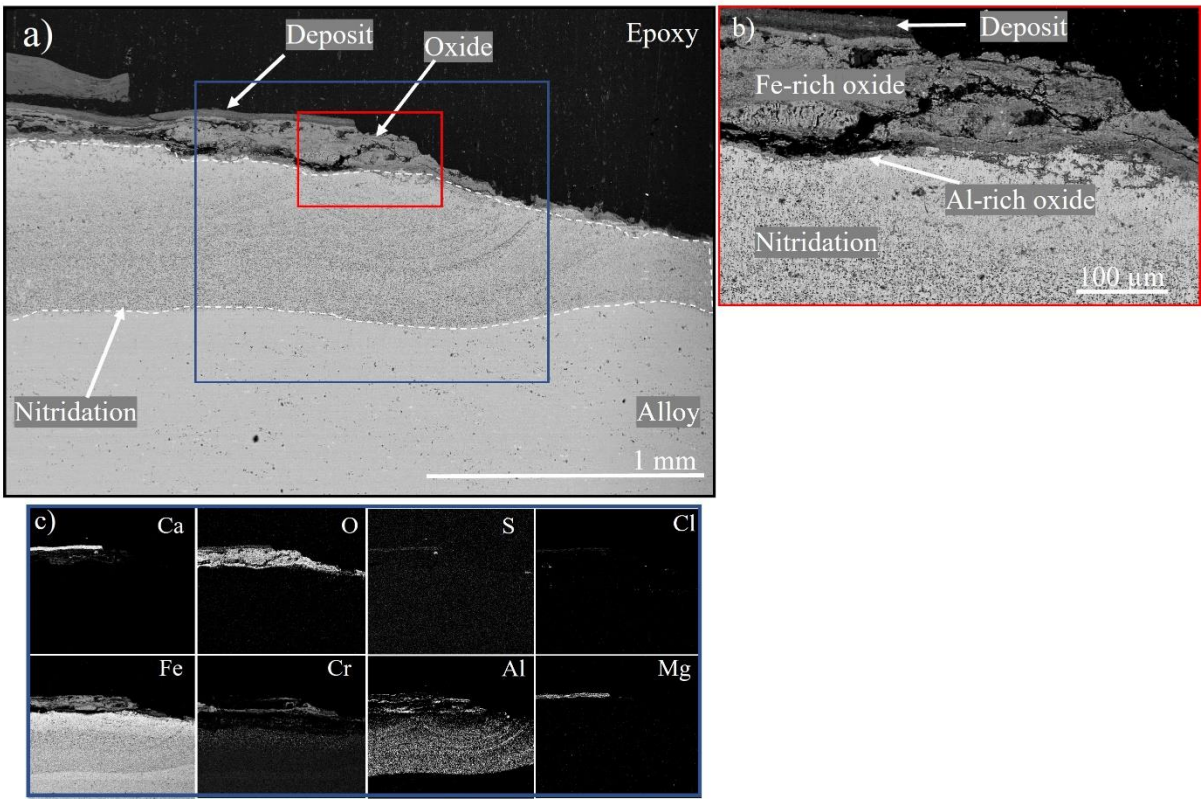

Figure 8.7: SEM BSE cross-sectional images of EF101 after: (a) 6 months of exposure; (b) Higher-magnification image of the small area highlighted in (a); (c) EDX mapping of the large area highlighted in (a).

From the analysis of the FeCrAl alloys, it was clear that breakaway corrosion had occurred after 6 months of exposure, which indicates that the material degradation rate is strongly affected by the corrosive environment. As highlighted in Chapter IV, Ni-based alloys are frequently employed as coatings or weld overlays on the heat-exchange tubes of waste-fired boilers, to improve corrosion resistance. Nevertheless, due to their high Ni content, these materials are rather expensive. To enhance boiler efficiency, it is imperative to find alternative materials that have equivalent or superior material degradation resistance properties and that are available at a lower cost. The novel FeCrAl alloys EF100 and EF101 exhibited comparable material losses to the Ni-based alloy Sanicro 69 after 6 months of exposure, suggesting the potential of these alloys to substitute for Ni-based coatings and weld overlay materials in this specific application. However, in the microstructural analyses, severe internal nitridation was observed for both FeCrAl alloys. In the present study, it appears that the formation of AlN does not have a significant impact on the rate of material loss. This might seem counterintuitive at first, as the formation of AlN locks the aluminum in place rather than forming a protective Al-rich oxide. However, from the SEM BSE analyses, it is evident that both EF101 and EF100 underwent breakaway corrosion after 6 months of exposure, forming multilayer oxides that consisted of an Fe-rich oxide and a Cr/Al-rich oxide and with traces of Fe close to the metal/oxide interphase. After breakaway corrosion, the protective properties of FeCrAl alloys depend solely on the protective properties of the multilayer oxide scales and not on the formation of the primary protective Al-rich oxide. As such, one might argue that AlN should not impact significantly the protective properties of FeCrAl in the breakaway regime. However, a previous study [84] carried out after breakaway corrosion has suggested that the concentration of Al in the inward-growing, Cr/Al-rich spinel oxide formed after breakaway corrosion of FeCrAl alloys significantly reduces the need for Cr to prevent internal oxidation. In addition, the depletion

of Al from the alloy structure due to AlN formation may change the microstructure of the alloy, thereby altering the mechanical properties of the material. The effect of AlN is, therefore, an interesting issue and its effects on the corrosive properties after breakaway corrosion remain rather elusive. An investigation as to how nitridation impacts the secondary protective properties of FeCrAl alloys in a high-temperature corrosive environment is planned as part of future studies, as discussed in Chapter VIII.

Lastly, it has been reported in previous studies [95] that the addition of Si to FeCrAl alloys significantly increases the corrosion resistance of the material for superheater applications in biomass- and waste-fired boilers. In the present study the effect of Si was not visible.

8.2 Paper II - $PbCl_2$-Induced Corrosion on Low-alloyed Steel

To investigate the initiation and propagating corrosion mechanisms of $PbCl_2$-induced corrosion on a low-alloyed steel (T22), a time-resolved study was carried out using the experimental setup described in Section 6.2.

8.2.1 Oxide Growth Rate

Figure 8.8 illustrates the average oxide thicknesses of T22 after exposure times of 1, 24, and 168 hours in three different environments: 5% O_2 + 20% H_2O; $PbCl_2$ + 5% O_2 + 20% H_2O; and PbO + 5% O_2 + 20% H_2O. The inclusion of PbO was motivated by the findings presented in Section 8.2.2 and was designed to investigate in detail the role of Pb in the propagating corrosion mechanisms of $PbCl_2$-induced corrosion.

In all cases, the samples show parabolic kinetics, indicating that the oxide growth is diffusion-controlled. However, in the case of the $PbCl_2$ exposed samples, a significant standard deviation in oxide thickness was observed, making the parabolic growth rate less apparent. In the presence of $PbCl_2$, a noticeable oxide thickness (approximately 4 µm) was observed after just 1 hour of exposure. This thickness was roughly 40-times greater than those of samples exposed to PbO or samples without deposits after 1 hour of exposure. Over time, the oxide thickness continued to increase, reaching approximately 6 µm after 24 hours and 15 µm after 168 hours for the samples exposed to $PbCl_2$.

The samples exposed to PbO obtained a significantly reduced oxide thickness compared to the $PbCl_2$-exposed samples. After 24 hours of exposure, the oxide thickness was similar to those of the samples exposed without any deposit, measuring approximately 0.1 µm and 0.7 µm after 1 hour and 24 hours, respectively. However, after 168 hours, a significantly reduced oxide

thickness was recorded for the PbO-exposed sample, having roughly half the oxide thickness of the samples without any deposit (0.8 µm and 1.8 µm, respectively) (Figure 8.8).

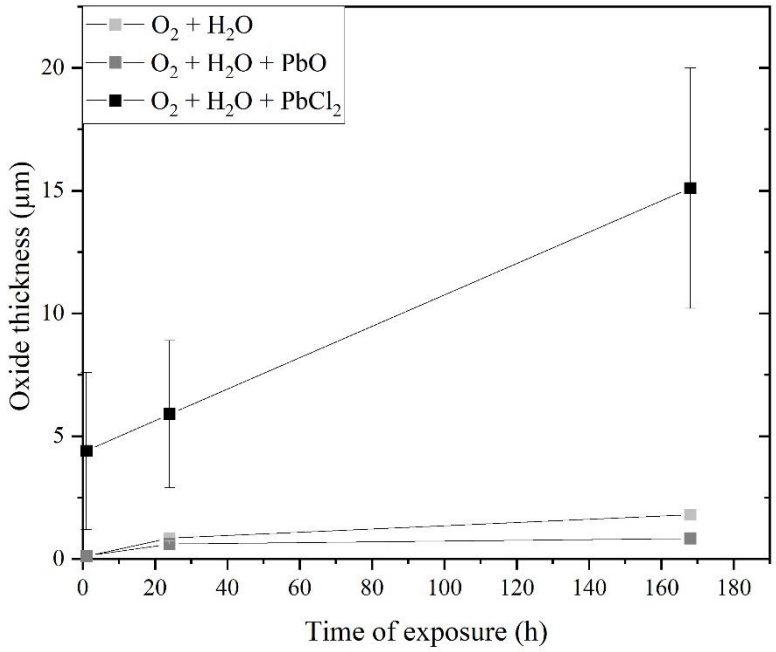

Figure 8.8. Oxide thicknesses of T22 in relation to time of exposure for the three environments tested.

8.2.2 Microstructural Analysis

8.2.2.1 5% O_2 + 20% H_2O + N_2 bal. (Ref).

SEM BSE cross-section analysis of samples exposed without any deposit after 24 and 168 hours of exposure is shown in Figure 8.9. In this environment, an adherent, dense and protective oxide scale had formed. This is consistent with the oxide thickness measurements presented in Figure 8.8 were a slow parabolic growth kinetic was demonstrated for these samples. The oxide scale was multilayered and consisted of an inward growing $(Fe,Cr)_3O_4$ spinel and an outward growing oxide scale with magnetite (Fe_3O_4) growing in the middle and hematite (Fe_2O_3) whiskers present at the top. The argument that the region of the outward and inward-growing oxide layers is between the Fe_3O_4 layer, and the spinel oxide layer is based on the relatively slow diffusion of Cr^{3+} in a spinel structure compared to Fe^{2+}/Fe^{3+} [117]. Therefore, the rapid outward diffusion of Fe ions promotes the creation of an outward-growing Fe-oxide layer, while Cr remains relatively stationary within the inward-growing spinel oxide.

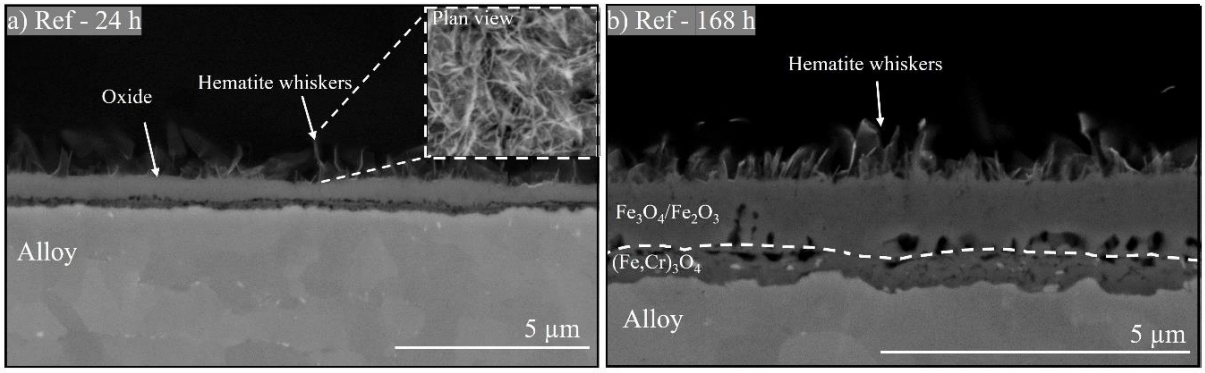

Figure 8.9: SEM BSE cross-section images of T22 exposed at 400°C in 5% O_2 + 20% H_2O + N_2 bal. after (a) 24 h; (b) 168 h.

8.2.2.2 $PbCl_2$ + 5%O_2 + 20% H_2O + N_2 bal.

The microstructural analysis of the samples exposed to $PbCl_2$ after 1, 24 and 168 hours of exposure is shown in Figure 8.10, 8.12 and 8.13. After 1 h of exposure severe corrosion in close vicinity to the original $PbCl_2$ particles was observed on the corroded surface (see Figure 8.10a). Large Fe-rich oxide nodules had partially grown on top of the $PbCl_2$ deposited particles, suggesting that rapid diffusion of Fe-ions takes place in these regions. A more homogenous oxide scale was observed in regions further away from highly concentrated $PbCl_2$ areas (referred to as base oxide), where hematite whiskers were growing on top of a Fe-rich oxide (see Figure 8.10b). Moreover, XRD analysis indicated that $PbCl_2$ was no longer present on the corroded surface and that that $Pb_3Cl_2O_2$(s) had formed (see highlighted area in Figure 8.11). The cross-sectional analysis (see Figure 8.10c) revealed the formation of a completely different microstructure compared to the sample exposed without $PbCl_2$. The oxide scale exhibited poor adhesion to the alloy substrate in areas with high concentrations of initially deposited $PbCl_2$ particles, where significant voids and cracks had developed. Furthermore, the EDX map analysis revealed Cl-containing compounds in two regions, namely in correction to Pb corresponding to mendipite and at the vicinity of the metal/oxide interface, presumably in the form of metal chloride (see Figure 8.10e).

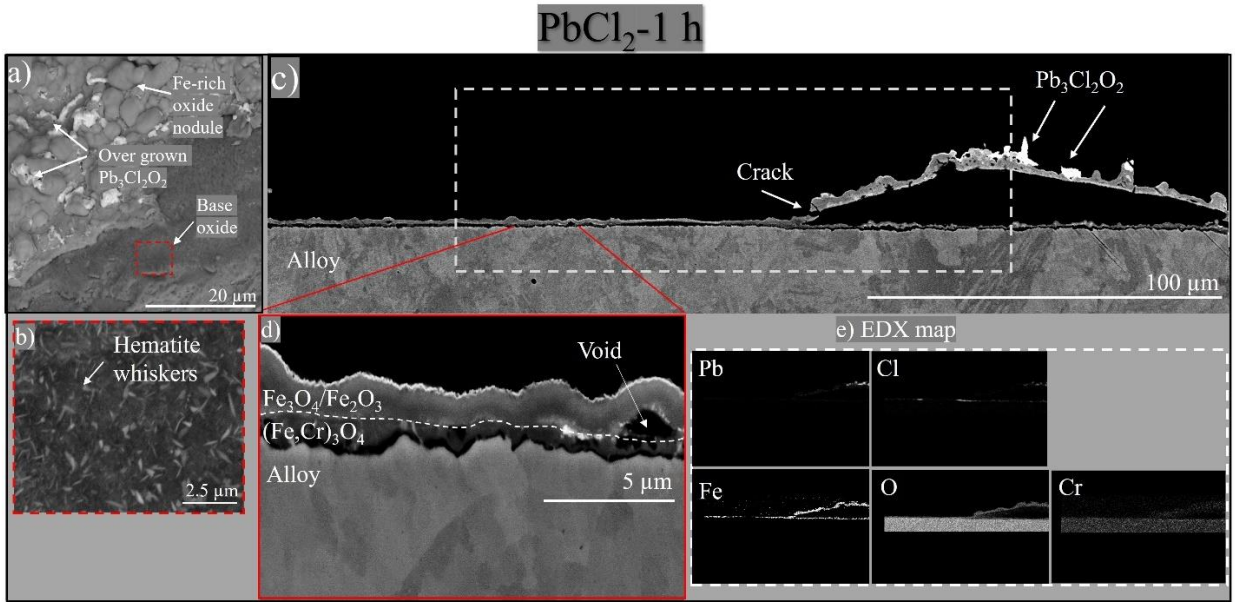

Figure 8.10: SEM BSE image of T22 exposed at 400°C in $PbCl_2$(s) + 5%O_2 + 20% H_2O + N_2 bal. for 1 hour. (a) Plan view image; (b) Highlighted area in (a); (c) Cross-section; (d) Higher magnification of selected area; (e) EDX map of highlighted area in (c).

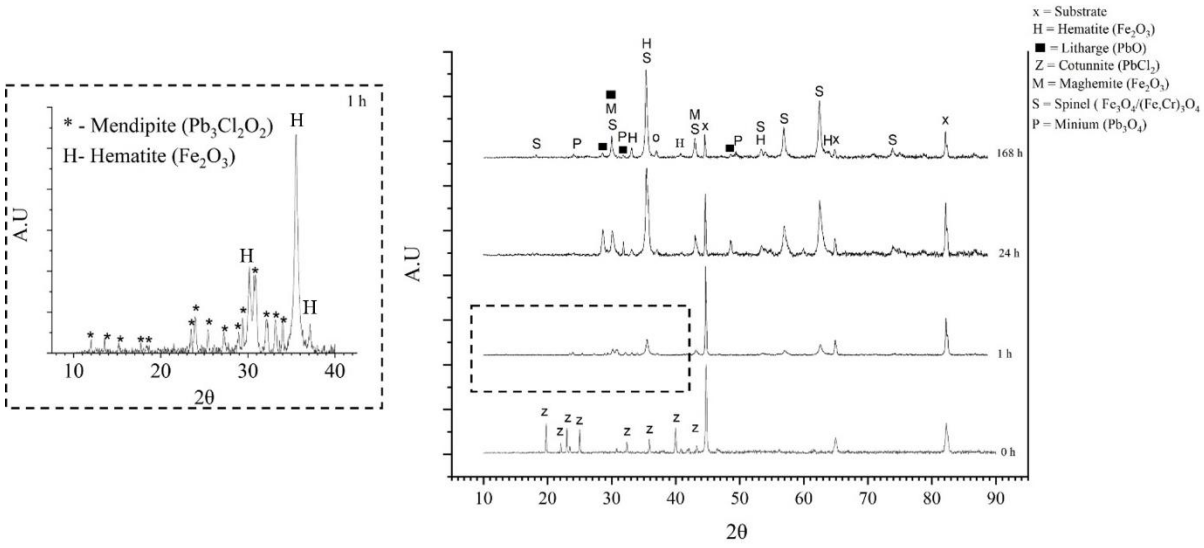

Figure 8.11: XRD spectra for samples exposed to $PbCl_2$(s) at 400°C for different exposure times. The highlighted section indicates the presence of mendipite formation after 1 hour of exposure.

Figure 8.12 shows the SEM microstructural analysis of the sample exposed to $PbCl_2$ for 24 hours. The corroded surface exhibited a heterogeneous oxide structure, similar to what was observed after 1 hour of exposure. However, there was an increased presence of Fe-rich oxide nodules growing over the initial $PbCl_2$ particles, as shown in Figure 8.12a. Furthermore, XRD analysis revealed the absence of $Pb_3Cl_2O_2$ on the surface, with intense peaks of PbO being identified on the corroded surface (see Figure 8.11). The SEM cross-section image revealed an increased formation of large voids and severe spallation of the oxide scale after 24 hours of exposure, as shown in Figure 8.12b. These features were generally observed in close proximity to the original $PbCl_2$ particles. Furthermore, a roughly 0.5 µm bright Pb-containing Fe-rich oxide (Fe-Pb-O) emerged on top of the outward-growing oxide layer (see Figure 8.12b). This oxide feature was generally observed in

close proximity to the originally deposited $PbCl_2$ particles. According to EDX analysis, it was shown that this region comprised approximately 7 atomic percent (at.%) of Pb, with the remainder of the atomic distribution identified as Fe. It's important to note that the presented at.% values represent cationic concentration, excluding oxygen. Lastly, The Cl map from the EDX analysis indicated the formation of metal chlorides at the metal/oxide interface (see Figure 8.12d).

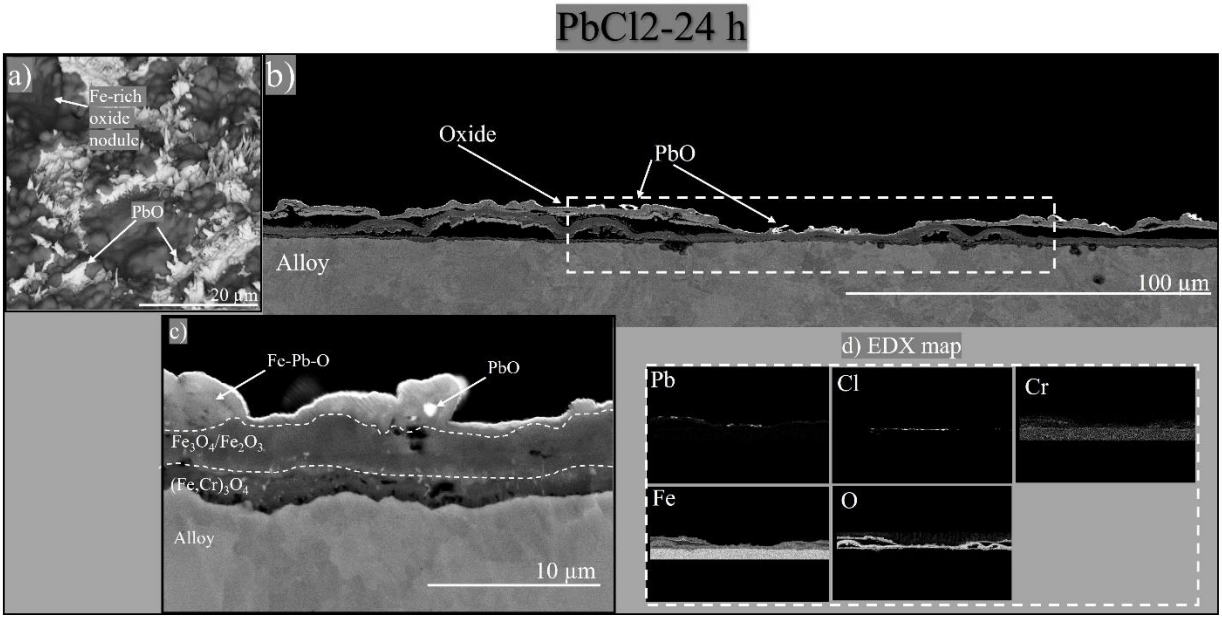

Figure 8.12: SEM BSE image of T22 exposed at 400°C in $PbCl_2$(s) + 5%O_2 + 20% H_2O + N_2 bal. for 24 hours. (a) Plan view image; (b) Cross-section; (c) Section with Fe-Pb-O formation; (d) EDX map of highlighted area in (b).

The corroded surface of the sample exposed to 168 hours showed both the formation of PbO and Pb_3O_4 according to XRD (see Figure 8.11). Cracks were observed on the corroded surface (see Figure 8.13a). From the cross-section analysis, the oxide morphology continued to show large void formations and accumulation of metal chlorides at the metal/oxide interface (see Figure 8.13b). Severe cracks on the oxide scale were observed, resulting in the formation of a porous oxide structure. From EDX map analysis it was shown that metal chlorides were still present close to the metal/oxide interface (see Figure 8.13d).

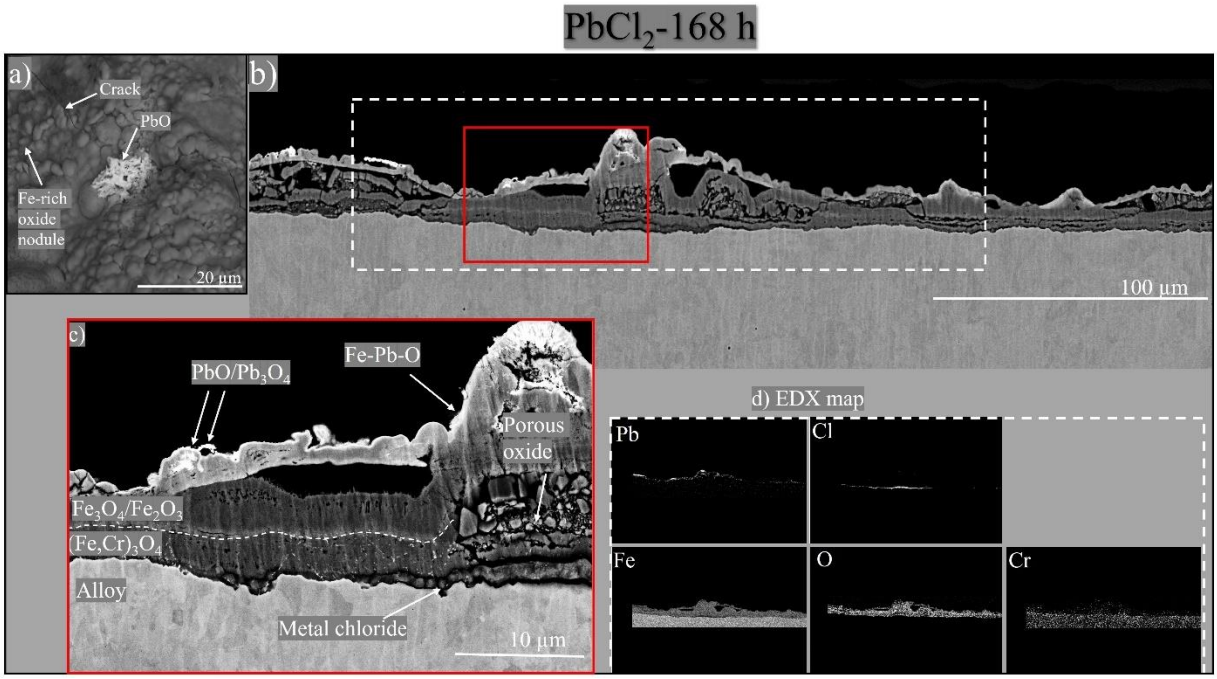

Figure 8.13: SEM BSE image of T22 exposed at 400°C in $PbCl_2$(s) + 5%O_2 + 20% H_2O + N_2 bal. for 168 hours. (a) Plan view image; (b) Cross-section; (c) Higher-magnification image of the small, highlighted area in (b); (d) EDX map of the large, highlighted area in (b).

8.2.2.1 PbO + 5% O_2 + 20% H_2O + N_2 bal.

Given that PbO was present on the corroded surface of the $PbCl_2$-exposed samples after 24 hours of exposure and remained present throughout the entire exposure period, a natural question arises: What is the impact of PbO formation on the progressing corrosion mechanisms? To isolate the influence of PbO, T22 samples deposited with PbO were prepared and exposed to the same experimental conditions as the $PbCl_2$-exposed samples described in Section 6.2.2.

Figure 8.14a-c shows the plan view images of the samples exposed to PbO. A significant difference in the oxide morphology between samples exposed to $PbCl_2$ and PbO was noted. Throughout the exposure time, there was no evidence of any accelerated corrosion rate associated to the deposited PbO particles or crack formation of the oxide scale. After 1 hour of exposure, barely any oxide layer was observed on the surface of the sample. After 24 and 168 hours of exposure, a Fe-rich oxide with traces of Pb (Fe-Pb-O) was present on the surface. The XRD spectra of the samples exposed to PbO indicated the presence of magnetoplumbite ($PbFe_{12}O_{19}$) after 168 hours of exposure (see Figure 8.15). In contrast to the samples exposed to $PbCl_2$ and those without any deposit, there were no indications of hematite whiskers on the surface of samples exposed to PbO. This finding was also confirmed with XRD analysis. After 168 hours of exposure, Both PbO and Pb_3O_4 were detected on the surface, and it is suggested that the formation of Pb_3O_4 resulted from the additional oxidation of the deposited PbO particles.

The SEM cross-sectional analysis revealed the formation of a firmly adherent and compact multilayer oxide structure (see Figure 8.14d-f). This structure consisted of an inward-growing layer of $(Fe,Cr)_3O_4$ spinel oxide and an outward-growing layer of magnetite (Fe_3O_4) oxide after 24 hours of exposure. On the surface, there was a continuous and uniform Fe-Pb-O oxide layer, presumably identified as magnetoplumbite. After 168 hours of exposure similar oxide features were observed as after 24 hours of exposure. EDX point analysis were carried out on the top oxide region in Figure

8.14f revealing an approximate composition of 8-9 (cat at.%) of Pb, with the remainder of the cat at.% being identified as Fe. These findings offer additional support for the presence of magnetoplumbite, as the atomic ratio of Pb/Fe for this oxide is approximately 8 at.%.

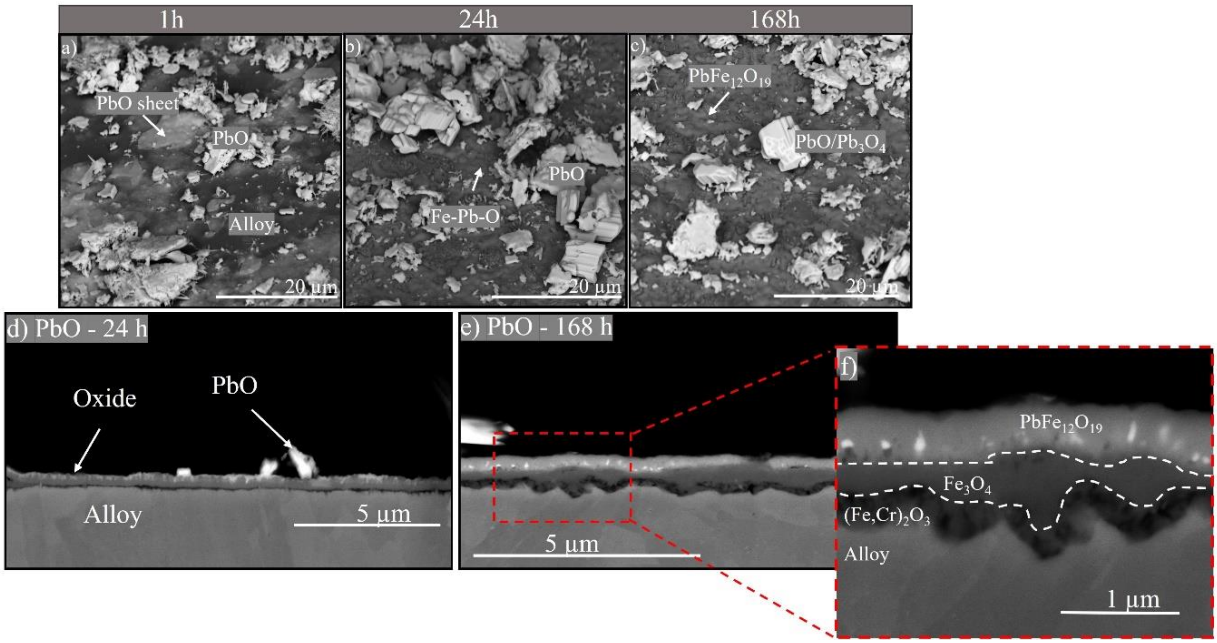

Figure 8.14. SEM BSE image of T22 exposed at 400°C in PbO_2(s) + 5%O_2 + 20% H_2O + N_2 bal. (a-c) Plan view image; (d) Cross-section after 24 hours of exposure; (e) Cross-section after 168 hours of exposure; (f) Higher magnification image of highlighted area in (e).

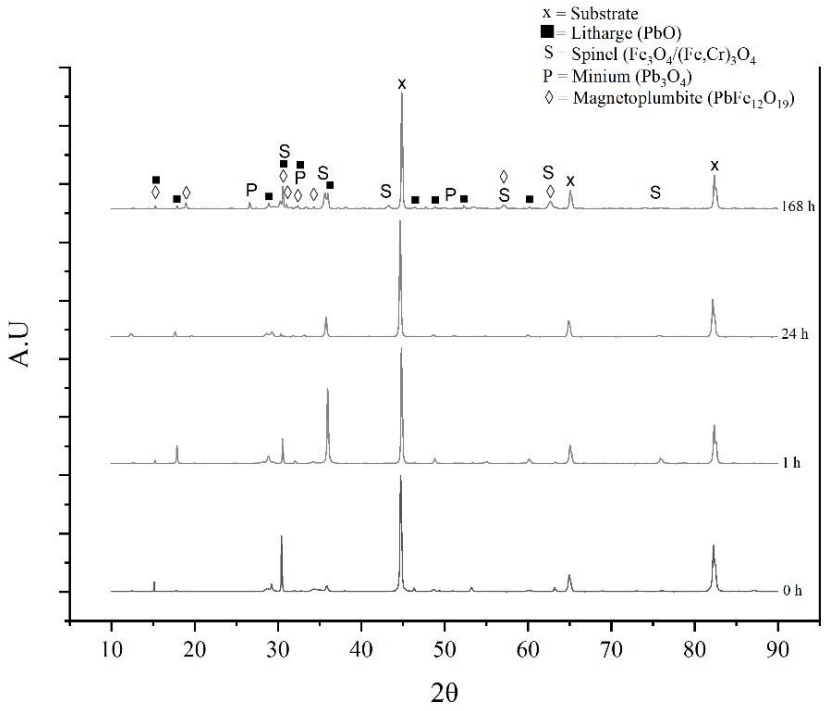

Figure 8.15: XRD spectra for samples exposed to PbO.

8.2.3 The Corrosion Mechanisms of $PbCl_2$ on Low-alloyed Steel

As presented in Chapter IV, various proposed corrosion mechanisms have associated the presence of $PbCl_2$ with the acceleration corrosion rate observed on various alloy types, including low-alloyed steel. This thesis will put forth arguments and engage in a discussion regarding potential corrosion mechanisms that have been previously proposed in the literature that is of relevance to this study based on the obtained results. The discussion will be divided in to two sections where the role of Cl and Pb on the corrosion attack on the low-alloyed steel is discussed separately.

8.2.3.1 The Role of Cl

From the results obtained, it is evident that $PbCl_2$ highly accelerates the corrosion rate of T22. The presence of mendipite $Pb_3Cl_2O_2$ on the corroded surface after 1 hour of exposure shows the extreme reactivity of $PbCl_2$ in this environment. Moreover, the accumulation of chlorine observed at the metal/oxide interface indicates that chlorine has diffused away from the initial $PbCl_2$ particles, likely resulting in the formation of metal chlorides. It may be noted that a prerequisite for Cl diffusion to occur through the oxide scale is the release of Cl from $PbCl_2$. From XRD analysis, it was shown that $PbCl_2$ had formed $Pb_3Cl_2O_2$ and PbO after 1 hour and 24 hours, respectively. Based on these observations, it is proposed that the chlorine is released from $PbCl_2$ in a two-step process, resulting in the formation of HCl(g) at the surface of the sample:

$$3PbCl_2(s) + 2H_2O(g) \rightarrow Pb_3Cl_2O_2(s) + 4HCl(g) \quad (8.1)$$

$$Pb_3Cl_2O_2(s) + H_2O(g) \rightarrow 3PbO(s) + 2HCl(g) \quad (8.2)$$

To the best of the author's knowledge, this is the first time mendipite is observed in these conditions. The Gibbs free energy could not be determined due to the limited availability of thermodynamic data related to these reactions. Therefore, it is important to regard these reactions solely in light of experimental observations.

The accumulation of metal chlorides at the metal/oxide interface has been documented in previous studies for T22 exposed at high temperature corrosion with KCl(s) and has been associated with a significant decrease in the adhesion of the oxide scale to the metal surface [118]. The results from the microstructural analysis in this thesis show that areas closed to the deposited $PbCl_2$ particles suffered from severe spallation, cracking and delamination of the oxide layer. The severe delamination is argued to occur due to the rapid and local release of HCl(g) described in Reaction (8.1) and (8.2). The HCl(g) is then suggested to form Cl ions on the corroded surface according to the electrochemical approach discussed in Section 5.1 and diffuse to the metal oxide, where metal chlorides are formed. By employing an ion-based transport mechanism, it can be argued that the diffusion of monovalent Cl- ions is anticipated to occur more rapidly than that of O^{2-} ions. As such this phenomenon elucidates the formation of stable metal chlorides at the metal/oxide interface.

As mentioned, the cross-section analysis revealed severe spallation, crack, and void formation occurring within just 1 hour of exposure for samples exposed to $PbCl_2$. It is argued that the surface cracks on the spalled oxide scale initiate rapid transport of $O_2(g)$ and $H_2O(g)$ to the metal/oxide interface promoting the formation of a secondary oxide layer. Due to the presence of metal chloride at the metal/oxide interface, it is further argued that the formed oxide layer has diminished adhesive properties and eventually also detaches from the metal surface. This detachment was observed on the sample after 24 hours of exposure, initiating a cyclic event wherein a new oxide scale is formed, and thus the process repeats. After 168 hours, it is argued that many of these voids have been filled due to the continuous formation of new oxide scale inside the voids. As such it is postulated that

regions with high concentration of initial $PbCl_2$ undergoes a crack-induced corrosion attack (see Figure 8.16).

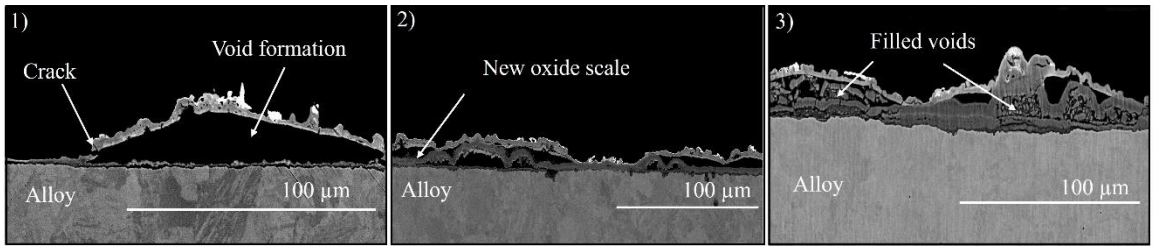

Figure 8.16. Proposed crack-induced corrosion mechanism on T22 exposed to $PbCl_2$. (1) The presence of metal chlorides at the metal/oxide interface facilitates delamination, void and crack formation on the oxide scale. (2) This process in turn facilitates rapid diffusion of $O_2(g)$ and $H_2O(g)$ to the metal/oxide interface, consequently promoting the growth of a new oxide scale at the metal/oxide interface. The newly formed oxide scale will eventually spall off as well, driven by the presence of metal chlorides at the metal/oxide interface. (3) It is proposed that this process continues over time, with the voids eventually becoming filled with oxide, which leads to severe cracking of the oxide scale.

However, it is important to note that the crack-induced corrosion mechanism discussed above is not proposed as the sole explanation for the increased oxidation kinetics for the sample exposed to $PbCl_2$. This since regions with good adherence to the metal substrate were also found and displayed significantly higher oxide thickness than the sample exposed without deposit (compare Figure 8.12c with Figure 8.9a). This could once again be attributed to the formation of metal chlorides, which have been associated with facilitating improved ion diffusion through oxide scales [119]. It is possible that the formation of metal chlorides distributed across the oxide scale may have taken place in the present study. However, it is noteworthy that no Cl was detected within the oxide scale during EDX mapping and point analysis, except at the metal/oxide interface. It is important to acknowledge that detecting trace amounts of Cl using SEM EDX is challenging, and implementing a higher-resolution technique such as STEM may be necessary to confirm this hypothesis.

8.2.3.1 The Role of Pb

Lastly, let us shift our focus to the role of Pb. While it is evident that Cl plays a significant role in accelerating the corrosion rate of $PbCl_2$ on low-alloyed steel in the current environment, it is argued that Pb assumes a more passive role. Following 24 hours of exposure, the corroded surface exhibited the presence of PbO, along with the existence of a Fe-Pb-O oxide at the top oxide layer in proximity to the initial $PbCl_2$ particles. In parallel exposures conducted on T22 exposed to PbO, the corrosion rate was minimal, and the microstructure exhibited the formation of a dense, slowly growing oxide. On top of this oxide scale magnetoplumbite was argued to be present. Although magnetoplumbite was not identified in the XRD analysis of $PbCl_2$-exposed samples, the atomic percentage (at.%) of Pb in the regions of Pb-Fe-O was similar to that of magnetoplumbite. However, due to the severe formation of cracks spalling of the oxide layer caused by the presence of metal chlorides, it is assumed that the protective properties of the Pb-Fe-O oxide layer is lost in the sample exposed to $PbCl_2$.

Chapter IX
Summary and Future Work

9.1 Paper I- Material selection for FBHE Application

The key findings from the field exposure study assessing the performance of relevant alloy types for FBHE application in the loop seal region of a CFB waste-fired boiler is summarized below:

- ✓ The microstructure and material loss analysis revealed that all the tested alloy types had undergone breakaway corrosion after 6 months of exposure. It was shown that corrosion played a significant role in the material degradation mechanisms while damage from erosion was considered low. These results emphases the importance of considering corrosion mitigation approaches when choosing suitable materials for FBHE application in the loop seal region of CFB waste-fired boilers.

- ✓ Conventional austenitic stainless steel 316Ti obtain high material losses, highlighting that this material may not be suitable for the specific application. On the other hand, the austenitic stainless steel SX that contained elevated concentrations of Ni and Si showed superior resistance towards material degradation. This indicates the importance of both alloy elements for this application.

- ✓ The novel FeCrAl alloys EF100 and EF101, demonstrated promising material degradation resistance after 6 and 12 months of exposure. Their material loss fell within a similar range as that of a Ni-based alloy, positioning them as potential candidates for this application. Nevertheless, the formation of internal Al-nitrides (AIN) could pose concerns over an extended exposure duration both from a corrosion and mechanical point of view.

Future work: For the novel FeCrAl alloys to become a strong contender for commercial alloys for FBHE applications, it is imperative to deepen our comprehension of how the formation of AlN impacts the corrosion rate beyond breakaway corrosion. As such, well-controlled laboratory studies on this subject are planned for future work on these alloy types.

9.2 Paper II- $PbCl_2$-Induced Corrosion on Low-alloyed Steel

The key findings from the laboratory study regarding $PbCl_2$-induced corrosion on low-alloyed steel is summarized below:

- ✓ The presence of $PbCl_2$ highly accelerated the corrosion rate on a low-alloyed steel (T22) at 400°C in an atmosphere of 5% O_2 + 20% H_2O and N_2 bal. The accelerated corrosion rate was apparent already after 1 h of exposure, and the accelerated corrosion attack is proposed to be a result of the rapid release of Cl from the reaction of $PbCl_2$ with the surrounding environment and formation of metal chlorides. The metal chlorides are argued to facilitate poor adhesion of the oxide scale and improved diffusion through the oxide scale. Both of these factors are believed to play a role in the severe corrosion attack.

- ✓ The accelerated corrosion attack induced by $PbCl_2$ on low-alloyed steels is primarily attributed to the role of Cl, whereas Pb is deemed to have a minor influence.

Future work: Detailed microstructural investigation with STEM and APT is planned for future work on the low-alloyed steel samples exposed to $PbCl_2$. This will aim to confirm the proposed corrosion mechanisms outlined in Paper II regarding $PbCl_2$-induced corrosion on low-alloyed steel.

Furthermore, future research will involve the addition of HCl(g) along with the introduction of high-alloyed steels such as Ni-based and FeCrAl alloys to the experimental matrix. The primary objective of this study will be to assess the feasibility of utilizing FeCrAl alloys as potential coating materials for water wall tubes in waste-fired boilers, which as of today remains relatively unexplored.

Chapter X
Bibliography

1. Lee H, Calvin K, Dasgupta D, Krinner G, Mukherji A, Thorne P, et al. AR6 Synthesis Report: Climate Change 2023. Summary for Policymakers. 2023.

2. Jamieson MA, Trowbridge AM, Raffa KF, Lindroth RL. Consequences of climate warming and altered precipitation patterns for plant-insect and multitrophic interactions. Plant physiology. 2012;160(4):1719-27.
3. Lindsey R. If carbon dioxide hits a new high every year, why isn't every year hotter than the last? Climate.gov2023 [Available from: https://www.climate.gov/news-features/climate-qa/if-carbon-dioxide-hits-new-high-every-year-why-isn%E2%80%99t-every-year-hotter-last.
4. Yoro KO, Daramola MO. CO2 emission sources, greenhouse gases, and the global warming effect. Advances in carbon capture: Elsevier; 2020. p. 3-28.
5. Li T, Baležentis T, Makutėnienė D, Streimikiene D, Kriščiukaitienė I. Energy-related CO2 emission in European Union agriculture: Driving forces and possibilities for reduction. Applied Energy. 2016;180:682-94.
6. Pörtner H-O, Roberts DC, Adams H, Adler C, Aldunce P, Ali E, et al. Climate change 2022: Impacts, adaptation and vulnerability: IPCC Geneva, Switzerland:; 2022.
7. [GlobalChange]. Available from:https://www.globalchange.gov/browse/multimedia/global-temperature-and-carbon-dioxide.
8. Ang BW, Su B. Carbon emission intensity in electricity production: A global analysis. Energy Policy. 2016;94:56-63.
9. A european green deal [Available from: A european green deal [Internet]. [cited 2023 May 13]. Available from: https://commission.europa.eu/strategy-and-policy/priorities-2019-2024/european-green-deal_en
10. Scarlat N, Prussi M, Padella M. Quantification of the carbon intensity of electricity produced and used in Europe. Applied Energy. 2022;305:117901.
11. Wolf S, Teitge J, Mielke J, Schütze F, Jaeger C. The European Green Deal—more than climate neutrality. Intereconomics. 2021;56:99-107.
12. Elavarasan RM, Pugazhendhi R, Irfan M, Mihet-Popa L, Khan IA, Campana PE. State-of-the-art sustainable approaches for deeper decarbonization in Europe–An endowment to climate neutral vision. Renewable and Sustainable Energy Reviews. 2022;159:112204.
13. Stoeglehner G, Narodoslawsky M. How sustainable are biofuels? Answers and further questions arising from an ecological footprint perspective. Bioresource technology. 2009;100(16):3825-30.
14. Davidsson KO, Åmand L-E, Leckner B, Kovacevik B, Svane M, Hagström M, et al. Potassium, chlorine, and sulfur in ash, particles, deposits, and corrosion during wood combustion in a circulating fluidized-bed boiler. Energy & fuels. 2007;21(1):71-81.
15. Nielsen HP, Frandsen F, Dam-Johansen K, Baxter L. The implications of chlorine-associated corrosion on the operation of biomass-fired boilers. Progress in energy and combustion science. 2000;26(3):283-98.
16. Michelsen HP, Frandsen F, Dam-Johansen K, Larsen OH. Deposition and high temperature corrosion in a 10 MW straw fired boiler. Fuel processing technology. 1998;54(1-3):95-108.
17. Albina DO, Themelis N. Theory and experience on corrosion of waterwall and superheater tubes of waste-to-energy facilities. Department of Earth and Environmental Engineering. 2005.
18. Francis Chinweuba E. Efficiency Improvements in Waste-to-Energy Combustion Processes: Method Development and Evaluation: Högskolan i Borås; 2019.
19. Brunner T, Fluch J, Obernberger I, Warnecke R. Investigations of aerosol formation pathways during MSW combustion based on high-temperature impactor measurements. Fuel processing technology. 2013;105:154-60.
20. Spiegel M. Salt melt induced corrosion of metallic materials in waste incineration plants. Materials and corrosion. 1999;50(7):373-93.
21. Bøjer M, Jensen PA, Frandsen F, Dam-Johansen K, Madsen OH, Lundtorp K. Alkali/Chloride release during refuse incineration on a grate: Full-scale experimental findings. Fuel Processing Technology. 2008;89(5):528-39.
22. Kinnunen H, Hedman M, Engblom M, Lindberg D, Uusitalo M, Enestam S, et al. The influence of flue gas temperature on lead chloride induced high temperature corrosion. Fuel. 2017;196:241-51.
23. Alipour Y, Henderson P. Corrosion of furnace wall materials in waste-wood fired power plant. Corrosion Engineering, Science and Technology. 2015;50(5):355-63.

24. Bankiewicz D, Vainikka P, Lindberg D, Frantsi A, Silvennoinen J, Yrjas P, et al. High temperature corrosion of boiler waterwalls induced by chlorides and bromides–Part 2: Lab-scale corrosion tests and thermodynamic equilibrium modeling of ash and gaseous species. Fuel. 2012;94:240-50.
25. Enestam S, Backman R, Mäkelä K, Hupa M. Evaluation of the condensation behavior of lead and zinc in BFB combustion of recovered waste wood. Fuel processing technology. 2013;105:161-9.
26. Enestam SH, Fabritius MK, Hulkkonen SK, Ro¨ ppa¨ nen JT, editors. Control of Ash-Related Operational Problems in BFB Combustion of Biofuels and Waste. International Conference on Fluidized Bed Combustion; 2003.
27. Antunes RA, de Oliveira MCL. Corrosion in biomass combustion: A materials selection analysis and its interaction with corrosion mechanisms and mitigation strategies. Corrosion Science. 2013;76:6-26.
28. Niemi J, Kinnunen H, Lindberg D, Enestam S. Interactions of PbCl2 with alkali salts in ash deposits and effects on boiler corrosion. Energy & Fuels. 2018;32(8):8519-29.
29. Lehmusto J, Skrifvars B-J, Yrjas P, Hupa M. High temperature oxidation of metallic chromium exposed to eight different metal chlorides. Corrosion Science. 2011;53(10):3315-23.
30. Sánchez Pastén M, Spiegel M. High temperature corrosion of metallic materials in simulated waste incineration environments at 300–600° C. Materials and corrosion. 2006;57(2):192-5.
31. Sadeghimeresht E, Reddy L, Hussain T, Markocsan N, Joshi S. Chlorine-induced high temperature corrosion of HVAF-sprayed Ni-based alumina and chromia forming coatings. Corrosion Science. 2018;132:170-84.
32. Larsson E. The Corrosive Effect of Chlorine Containing Species on Waterwalls and Superheater Materials in Waste and Biomass-Fired Power Plants: Chalmers Tekniska Hogskola (Sweden); 2017.
33. Bankiewicz D, Enestam S, Yrjas P, Hupa M. Experimental studies of Zn and Pb induced high temperature corrosion of two commercial boiler steels. Fuel Processing Technology. 2013;105:89-97.
34. Kinnunen H, Lindberg D, Lauren T, Uusitalo M, Bankiewicz D, Enestam S, et al. High-temperature corrosion due to lead chloride mixtures simulating fireside deposits in boilers firing recycled wood. Fuel Processing Technology. 2017;167:306-13.
35. Talus A, Norling R, Wickström L, Hjörnhede A. Effect of lead content in used wood fuel on furnace wall corrosion of 16Mo3, 304L and alloy 625. Oxidation of metals. 2017;87(5-6):813-24.
36. Talus A, Kinnunen H, Norling R, Enestam S. Corrosion of carbon steel underneath a lead/potassium chloride salt mixture. Materials and Corrosion. 2019;70(8):1450-60.
37. Alipour Y, Henderson P, Szakalos P. The effect of a nickel alloy coating on the corrosion of furnace wall tubes in a waste wood fired power plant. Materials and corrosion. 2014;65(2):217-25.
38. Johansson A, Johnsson F, Andersson B-Å. The performance of a loop seal in a CFB boiler. 2006.
39. Nafari A, Nylund A. Field study on superheater tubes in the loop seal of a wood fired CFB plant. Materials and Corrosion. 2004;55(12):909-20.
40. Ekström A. Conditions of increased life time of superheaters in loop seals: Uppsala University; 2018 [Master thesis]. Available from: https://www.diva-portal.org/smash/record.jsf?pid=diva2%3A1186253&dswid=4676.
41. aza S, Yao L, Bhada-Tata P, Van Woerden F. What a waste 2.0: a global snapshot of solid waste management to 2050: World Bank Publications; 2018.
42. Siddiqua A, Hahladakis JN, Al-Attiya WAK. An overview of the environmental pollution and health effects associated with waste landfilling and open dumping. Environmental Science and Pollution Research. 2022;29(39):58514-36.
43. Grosso M, Motta A, Rigamonti L. Efficiency of energy recovery from waste incineration, in the light of the new Waste Framework Directive. Waste Management. 2010;30(7):1238-43.
44. Directive L. Council Directive 1999/31/EC of 26 April 1999 on the landfill of waste. Official Journal of the European Communities. 1999;182(1):26.04.
45. Commision TE. Waste Framework Directive: The European Union; [Available from: https://environment.ec.europa.eu/topics/waste-and-recycling/waste-framework-directive_en#contact.
46. Eurostat. Municipal waste by waste management operations: The European Union; [Available from: https://ec.europa.eu/eurostat/databrowser/view/ENV_WASMUN__custom_7095573/default/table?lang=en.

47. Bolton K, Rousta K. Solid waste management toward zero landfill: a Swedish model. Sustainable resource recovery and zero waste approaches: Elsevier; 2019. p. 53-63.
48. energidepartementet M-o. Förslag till Europaparlamentets och rådets direktiv om ändring av

direktiv 2003/87/EG om ett system för handel med utsläppsrätter för växthusgaser

inom unionen samt om ändring av beslut (EU) 2015/1814 och förordning (EU)

2015/757: AVFALL SVERIGE; 2021 [Available from: https://www.regeringen.se/contentassets/e0855204cc064c6fa9d37d842a5cf4e9/avfall-sverige.pdf.
49. Regeringskansliet. Vägen till en klimatpositiv framtid SOU2020:4 29 January 20202020 [Available from: https://www.regeringen.se/rattsliga-dokument/statens-offentliga-utredningar/2020/01/sou-20204/.
50. Pour N, Webley PA, Cook PJ. Potential for using municipal solid waste as a resource for bioenergy with carbon capture and storage (BECCS). International Journal of Greenhouse Gas Control. 2018;68:1-15.
51. Beiron J, Normann F, Johnsson F. A techno-economic assessment of CO2 capture in biomass and waste-fired combined heat and power plants–A Swedish case study. International Journal of Greenhouse Gas Control. 2022;118:103684.
52. Vainikka P, Bankiewicz D, Frantsi A, Silvennoinen J, Hannula J, Yrjas P, et al. High temperature corrosion of boiler waterwalls induced by chlorides and bromides. Part 1: Occurrence of the corrosive ash forming elements in a fluidised bed boiler co-firing solid recovered fuel. Fuel. 2011;90(5):2055-63.
53. Pavlas M, Touš M, Klimek P, Bébar L. Waste incineration with production of clean and reliable energy. Clean Technologies and Environmental Policy. 2011;13:595-605.
54. Thorin E, Sandberg J, Yan J. Combined heat and power. 2015.
55. Lombardi L, Carnevale E, Corti A. A review of technologies and performances of thermal treatment systems for energy recovery from waste. Waste management. 2015;37:26-44.
56. Kalogirou EN. Waste-to-Energy technologies and global applications: CRC Press; 2017.
57. Enestam S, Bankiewicz D, Tuiremo J, Mäkelä K, Hupa M. Are NaCl and KCl equally corrosive on superheater materials of steam boilers? Fuel. 2013;104:294-306.
58. Viklund P, Hjörnhede A, Henderson P, Stålenheim A, Pettersson R. Corrosion of superheater materials in a waste-to-energy plant. Fuel Processing Technology. 2013;105:106-12.
59. Broström M, Kassman H, Helgesson A, Berg M, Andersson C, Backman R, et al. Sulfation of corrosive alkali chlorides by ammonium sulfate in a biomass fired CFB boiler. Fuel processing technology. 2007;88(11-12):1171-7.
60. Viklund P, Pettersson R, Hjörnhede A, Henderson P, Sjövall P. Effect of sulphur containing additive on initial corrosion of superheater tubes in waste fired boiler. Corrosion engineering, science and technology. 2009;44(3):234-40.
61. Karlsson S, Åmand L-E, Liske J. Reducing high-temperature corrosion on high-alloyed stainless steel superheaters by co-combustion of municipal sewage sludge in a fluidised bed boiler. Fuel. 2015;139:482-93.
62. Nielsen HP, Frandsen FJ, Dam-Johansen K. Lab-scale investigations of high-temperature corrosion phenomena in straw-fired boilers. Energy & Fuels. 1999;13(6):1114-21.
63. Saqib N, Bäckström M. Trace element partitioning in ashes from boilers firing pure wood or mixtures of solid waste with respect to fuel composition, chlorine content and temperature. Waste management. 2014;34(12):2505-19.
64. Winebrake JJ. Biomass Technology Roadmap. 2004.
65. Yin C, Li S. Advancing grate-firing for greater environmental impacts and efficiency for decentralized biomass/wastes combustion. Energy Procedia. 2017;120:373-9.
66. Van Caneghem J, Brems A, Lievens P, Block C, Billen P, Vermeulen I, et al. Fluidized bed waste incinerators: Design, operational and environmental issues. Progress in Energy and Combustion Science. 2012;38(4):551-82.
67. Mettanant V, Basu P, Butler J. Agglomeration of biomass fired fluidized bed gasifier and combustor. The Canadian Journal of Chemical Engineering. 2009;87(5):656-84.
68. Henderson P, Högberg J, Mattsson M. Reduction of fireside corrosion of superheater materials in a biomass-fired circulating fluidised bed boiler. 2002.

69. Sharp W. Superheater corrosion in biomass boilers: Today's Science and Technology. Oak Ridge National Laboratory. 2010:3.
70. Janiszewska D, Ossowska L. The role of agricultural biomass as a renewable energy source in European Union countries. Energies. 2022;15(18):6756.
71. Kinnunen H, Hedman M, Lindberg D, Enestam S, Yrjas P. Corrosion in recycled wood combustion—reasons, consequences, and solutions. Energy & Fuels. 2019;33(7):5859-66.
72. Krook J, Mårtensson A, Eklund M. Sources of heavy metal contamination in Swedish wood waste used for combustion. Waste Management. 2006;26(2):158-66.
73. Agency SE. Trädbränsle-, torv, och avfallspriser 2023-06-08 [Available from: https://www.energimyndigheten.se/statistik/den-officiella-statistiken/statistikprodukter/tradbransle--och-torvpriser/.
74. Vainikka P. Occurrence of bromine in fluidised bed combustion of solid recovered fuel. 2011.
75. Plants CoEW-t-E. Waste-to-Energy in Europe 2020 [Available from: https://www.cewep.eu/waste-to-energy-plants-in-europe-in-2020/.
76. KOFSTAD P. High temperature corrosion((Book)). London and New York, Elsevier Applied Science, 1988, 568. 1988.
77. Birks N, Meier GH, Pettit FS. Introduction to the high temperature oxidation of metals: Cambridge university press; 2006.
78. Young DJ. High temperature oxidation and corrosion of metals: Elsevier; 2008.
79. Tammann G. Über Anlauffarben von metallen. Zeitschrift für anorganische und allgemeine Chemie. 1920;111(1):78-89.
80. Wagner C. Beitrag zur theorie des anlaufvorgangs. Zeitschrift für physikalische Chemie. 1933;21(1):25-41.
81. Olivas Ogaz MA. High Temperature Corrosion of Low-alloyed and Stainless Steels: Mechanistic Study of Chlorine-Induced Corrosion. Ph D Thesis. 2019.
82. Persdotter A, Sattari M, Larsson E, Ogaz MO, Liske J, Jonsson T. Oxidation of Fe-2.25 Cr-1Mo in presence of KCl (s) at 400 C–Crack formation and its influence on oxidation kinetics. Corrosion Science. 2020;163:108234.
83. Larsson E, Gruber H, Hellström K, Jonsson T, Liske J, Svensson J-E. A Comparative Study of the Initial Corrosion of KCl and PbCl 2 on a Low-alloyed Steel. Oxidation of metals. 2017;87:779-87.
84. Eklund J, Persdotter A, Hanif I, Bigdeli S, Jonsson T. Secondary corrosion protection of FeCr (Al) model alloys at 600° C–The influence of Cr and Al after breakaway corrosion. Corrosion Science. 2021;189:109584.
85. Persdotter A, Eklund J, Liske J, Jonsson T. Beyond breakaway corrosion–Influence of chromium, nickel and aluminum on corrosion of iron-based alloys at 600° C. Corrosion Science. 2020;177:108961.
86. Zhou R, Wang F, Xu K, Yuan Y, Chen L, Lou M, et al. Effect of molybdenum addition on oxidation behavior and secondary protection mechanism of FeCrAl coatings. Materials Characterization. 2023;204:113221.
87. Eklund J, Persdotter A, Ssenteza V, Jonsson T. The long-term corrosion behavior of FeCrAl (Si) alloys after breakaway oxidation at 600° C. Corrosion Science. 2023;217:111155.
88. Cornell RM, Schwertmann U. The iron oxides: structure, properties, reactions, occurrences, and uses: Wiley-vch Weinheim; 2003.
89. Pohja R, Hänninen H. Properties of FeCrAl Alloys and Austenitic Stainless Steel for Boiler Environments. 2010.
90. Kumar N, Pandey C, Kumar P. Dissimilar welding of Inconel alloys with austenitic stainless-steel: A review. Journal of Pressure Vessel Technology. 2023;145(1):011506.
91. Michler T. Austenitic stainless steels. Reference Module in Materials Science and Materials Engineering. 2016;1(6).
92. Jonsson T, Karlsson S, Hooshyar H, Sattari M, Liske J, Svensson J-E, et al. Oxidation after breakdown of the chromium-rich scale on stainless steels at high temperature: internal oxidation. Oxidation of Metals. 2016;85:509-36.
93. Pettersson J. Alkali Induced High Temperature Corrosion of Stainless Steel-Experiences from Laboratory and Field: Chalmers University of Technology; 2008.
94. Kim I, Choi B, Jung J, Do J, Jo C. Effect of microstructural characteristics on the low cycle fatigue behaviors of cast Ni-base superalloys. Materials Characterization. 2015;106:375-81.

95. Eklund J, Paz MD, Jönsson B, Liske J, Svensson JE, Jonsson T. Field exposure of FeCrAl model alloys in a waste-fired boiler at 600° C: The influence of Cr and Si on the corrosion behaviour. Materials and Corrosion. 2019;70(8):1476-85.
96. Geers C, Babic V, Mortazavi N, Halvarsson M, Jönsson B, Johansson L-G, et al. Properties of alumina/chromia scales in N 2-containing low oxygen activity environment investigated by experiment and theory. Oxidation of Metals. 2017;87:321-32.
97. Sand T, Liske J, Helander T, Svensson J-E, Johansson L-G. A Comparison of the Oxidation and Nitridation Properties of Selected Chromia-and Alumina-Forming Alloys at 800° C. Oxidation of Metals. 2022;98(1-2):163-78.
98. Eklund J, Hanif I, Bigdeli S, Jonsson T. High temperature corrosion behavior of FeCrAlSi model alloys in the presence of water vapor and KCl at 600 C–The influence of Cr content. Corrosion Science. 2022;198:110114.
99. McNallan M, Liang W, Kim S, Kang C. Acceleration of the high temperature oxidation of metals by chlorine. High Temperature Corrosion, NACE. 1983;316.
100. Grabke H, Reese E, Spiegel M. The effects of chlorides, hydrogen chloride, and sulfur dioxide in the oxidation of steels below deposits. Corrosion science. 1995;37(7):1023-43.
101. Folkeson N, Johansson L-G, Svensson J-E. Initial stages of the HCl-induced high-temperature corrosion of alloy 310. journal of the electrochemical society. 2007;154(9):C515.
102. Cantatore V, Olivas Ogaz MA, Liske J, Jonsson Tr, Svensson J-E, Johansson L-G, et al. Oxidation driven permeation of Iron oxide scales by chloride from experiment guided first-principles modeling. The Journal of Physical Chemistry C. 2019;123(42):25957-66.
103. Pettersson J, Folkeson N, Johansson L-G, Svensson J-E. The effects of KCl, K 2 SO 4 and K 2 CO 3 on the high temperature corrosion of a 304-type austenitic stainless steel. Oxidation of metals. 2011;76(1):93-109.
104. Bryers RW. Fireside slagging, fouling, and high-temperature corrosion of heat-transfer surface due to impurities in steam-raising fuels. Progress in energy and combustion science. 1996;22(1):29-120.
105. Daniel P, Barna J, Blue J, editors. Furnace-wall corrosion in refuse-fired boilers. Proc 1986 Natl Waste Proc Conf, Denver, Colorado; 1986.
106. Bankiewicz D, Yrjas P, Lindberg D, Hupa M. Determination of the corrosivity of Pb-containing salt mixtures. Corrosion Science. 2013;66:225-32.
107. Henderson P, Hjörnhede A. Combating corrosion in biomass and waste-fired plant. 2010.
108. Rishel D, Pettit F, Birks N. Some principal mechanisms in the simultaneous erosion and corrosion attack of metals at high temperatures. Materials Science and Engineering: A. 1991;143(1-2):197-211.
109. Nafari A, Nylund A. Erosion corrosion of steel tubes in the loop seal of a biofuel fired CFB plant. 2002.
110. Reimer L. Scanning electron microscopy: physics of image formation and microanalysis. Measurement Science and Technology. 2000;11(12):1826-.
111. Baatsen P, Gabarre S, Vints K, Wouters R, Vandael D, Goodchild R, et al. Preservation of fluorescence signal and imaging optimization for integrated light and electron microscopy. Frontiers in Cell and Developmental Biology. 2021;9:737621.
112. Guinier A. X-ray diffraction in crystals, imperfect crystals, and amorphous bodies: Courier Corporation; 1994.
113. Uusitalo M, Vuoristo P, Mäntylä T. High temperature corrosion of coatings and boiler steels below chlorine-containing salt deposits. Corrosion science. 2004;46(6):1311-31.
114. Bajt Leban M, Vončina M, Kosec T, Tisu R, Barborič M, Medved J. Comparison of cycling high temperature corrosion at 650 C in the presence of NaCl of various austenitic stainless steels. High Temperature Corrosion of Materials. 2023;99(1-2):63-77.
115. Jonsson T, Canovic S, Liu F, Asteman H, Svensson J-E, Johansson L-G, et al. Microstructural investigation of the effect of water vapour on the oxidation of alloy 353 MA in oxygen at 700 and 900 C. Materials at High Temperatures. 2005;22(3-4):231-43.
116. Amy S, Vangeli P. Water vapour effect on the high temperature resistant grades. EUROCORR 2001. 2001.
117. Van Orman JA, Crispin KL. Diffusion in oxides. Reviews in Mineralogy and Geochemistry. 2010;72(1):757-825.

118. Jonsson T, Folkeson N, Svensson J-E, Johansson L-G, Halvarsson M. An ESEM in situ investigation of initial stages of the KCl induced high temperature corrosion of a Fe–2.25 Cr–1Mo steel at 400 C. Corrosion Science. 2011;53(6):2233-46.
119. Folkeson N, Jonsson T, Halvarsson M, Johansson LG, Svensson JE. The influence of small amounts of KCl (s) on the high temperature corrosion of a Fe-2.25 Cr-1Mo steel at 400 and 500° C. Materials and Corrosion. 2011;62(7):606-15.